学位論文

A Search for a Contribution from Axion-Like Particles to the X-Ray Diffuse Background Utilizing the Earth's Magnetic Field

(地球磁場を用いたアクシオン様粒子起因の
X線背景放射の探索)

平成 28 年 7 月 博士（理学）申請

東京大学大学院理学系研究科
物理学専攻

山本 亮

Abstract

Axion Like Particles (ALPs) are theoretical particles of a quantum field which work to conserve CP symmetry in a strong interaction. They can be converted into photons by an electromagnetic field, via an inverse Primakoff effect. If the ALPs are abundant in the universe as a cold dark matter in the standard cosmology, isotropic distribution is expected, and photons from ALPs contribute to diffuse background radiation in the corresponding waveband. In this thesis, we propose a novel method to uncover ALP origin photons by space observatory using the Earth's magnetic field to host the inverse Primakoff process. In the X-ray band, we selected a CCD camera system, XIS, which is an onboard *Suzaku* satellite because of low intrinsic background capability. We selected four observing directions from the archival data and evaluated the diffuse background spectra as a function of the integrated magnetic field $(BL)^2$ of an order of 10^4 $\mathrm{T^2m^2}$ in the field of view. Assuming a continuum emission with ($dN/dE \propto E^{+0.5}$) made by the ALPs produced at the cosmological distance as proposed by Kawasaki & Yanagida (1997) and Asaka et al. (1998), the upper limit at 99 % *CL* for a continuum emission from the ALPs converted by the Earth magnetosphere is 2.8×10^{-9} erg $\mathrm{s^{-1}}$ $\mathrm{cm^{-2}}$ $\mathrm{sr^{-1}}$ normalized at 10^4 $\mathrm{T^2m^2}$with a detailed study of the intrinsic background reproduction and systematic errors. It corresponds to the 6–15 % of the observed cosmic X-ray background (CXB) surface brightness in 2–6 keV, and is not contradictory to the current understanding of the CXB , that 75–80 % of the CXB are resolved into the sum of point sources. It limits the ALP-photon coupling constant to be $g_{\mathrm{a}\gamma\gamma} < 4.4 \times 10^{-7}$ $\mathrm{GeV^{-1}}$ $\left(\frac{m_\phi}{10\ \mathrm{keV}}\right)^{5/4}$ $\left(\frac{\tau_\phi}{4.32\times10^{17}\ \mathrm{s}}\right)^{1/2}$ $\left(\frac{B_\perp L}{100\ \mathrm{Tm}}\right)^{-1}$ $\left(\frac{\rho_\phi}{1.52\ \mathrm{keV\ cm^{-3}}}\right)^{-1/2}$ $\left(\frac{H_0}{2.20\times10^{-18}\ \mathrm{s^{-1}}}\right)^{1/2}$ $\left(\frac{f}{1.92}\right)^{1/2}$, assuming that a single type of dark matter decays to be the ALP. The upper limits for narrow line emission in 1–7 keV shown by Sekiya et al. (2016) is also interpreted to be the ALP density around the Galaxy to be $g_{\mathrm{a}\gamma\gamma} < 8.4 \times 10^{-8}$ $\mathrm{GeV^{-1}}$ $\left(\frac{B_\perp L}{140\ \mathrm{Tm}}\right)^{-1}$ $\left(\frac{\tau_\phi}{4.32\times10^{17}\ \mathrm{s}}\right)^{1/2}$ $\left(\frac{S_\phi}{50\ \mathrm{M_\odot pc^{-2}}}\right)^{-1/2}$. This search is complementary with other ALP search experiments in the mass range of ALPs.

Acknowledgments

I have been supported by many people in the last six years. If it had not been for their help, I would have never been able to finish my work.

I would like to express the deepest appreciation to my supervisor associate professor, Noriko Y. Yamasaki. She has lead me very thoughtfully and carefully both in scientific and experimental points of view. I feel that I could not learn so much without her encouragement. I would also like to thank Professor Kazuhisa Mitsuda who has given me a lot of perceptive advice for treating scientific results. I have gained a lot of insight from his strict attitudes for science. I am most grateful to Professor Masahiro Takada, who inspired me to search for ALP emissions in X-ray bands, and I am thankful for the useful discussions we shared.

I would like to thank my thesis committee members, Professor Masahiro Teshima, Professor Shoji Asai, associate professor Shigetaka Moriyama, associate professor Yasuhiro Kishimoto, and associate professor Izumi Tsutsui for valuable suggestions that improved the contents of this thesis.

I would like to show my greatest appreciation to associate professor Tomotake Matsumura, Dr. Yoh Takei, Dr. Norio Sekiya, nad Dr. Kazuhiro Sakai for useful discussions during my Ph.D. period. Also, special thanks to my colleagues at ISAS: Dr. Shu Koyama, Dr. Yuto Ichinohe, Dr. Masachika Iwai, Kenichiro Nagayoshi, Takahiro Kikuchi, Akira Chiba, Tasuku Hayashi, Masatoshi Hoshino, Haruka Muramatsu, Yuki Tsurugasaki, Keisei Maehisa, Yuki Nakashima, and Takahiro Nakayama. I have greatly benefited from Mr. Baluta Chris and Secretary Akiko Yokoyama in my lab life.

Finally, I want to acknowledge my parents and my sister for giving me the chance to study. Advice and comments from Dr. Tadao Kazuno have been a great help in my research experience. I have had a lot of supports and encouragement from Kyoko Iwata. Without this support, I would have never been able to keep studying.

Contents

List of Tables

List of Figures

Abbreviations

ADMX:	Axion Dark Matter eXperiment.
AGN:	active galactic nucleus.
ALP:	Axion-like particle.
ARF:	Ancillary response files of the *Suzaku* XIS detectors.
BGO:	Bismuth Germanium Oxide crystal.
BI:	Back-illuminated CCDs of XIS onboard *Suzaku*.
CAST:	CERN Axion Solar Telescope.
CIE:	Collisional ionization equilibrium.
CL:	Confidence level.
COR:	Cut-off-rigidity of the cosmic rays.
COR2:	The name of cut-off-rigidity in the calibration database of *Suzaku*.
CXB:	Cosmic X-ray background.
DYE_ELV:	Elevation angle from the day Earth rim.
ELV:	Elevation angle between the target and the Earth's limb of satellite.
FI:	Front-illuminated CCDs of XIS onboard *Suzaku*.
FoV:	Field of view of a telescope.
HTC:	High temperature component as unresolved plasma emission in the XDB.
HXD:	Hard X-ray detector onboard *Suzaku*.
IAXO:	International Axion Observatory.
IGRF-12:	International Geomagnetic Reference Field:the 12th generation as a mathematical model of Earth's magnetic field.
LAB survey:	The Leiden/Argentine/Bonn Survey.
LHB:	Local hot bubble.
LOC_ID:	Location ID.
MWH:	Milky way halo.
NEP:	North Ecliptic Pole.
NTE:	Night Earth observation when *Suzaku* sees the night side of the Earth.
NXB:	Non-X-ray background.
ObsID:	The unique observation number. Observation id.

PI:	Pulse Invariant of *Suzaku*/XIS.
PIN diode:	A semiconductor diode, which has intrinsic semiconductor region between a p-type semiconductor and an n-type semiconductor region.
PIN-UD:	PIN upper discriminator.
QCD:	Quantum chromodynamics.
RMF:	Redistribution matrix file of XIS energy.
SAA:	South Atlantic Anomaly.
SEP:	South Ecliptic Pole.
SWCX:	Solar wind charge exchange.
XDB:	X-ray diffuse background.
XIS:	X-ray imaging spectrometer; the CCDs onboard *Suzaku*.
XRT:	X-ray telescope onboard *Suzaku*.

1 Introduction

The Standard Model of particle physics has succeeded to explain various physical phenomena in wide energy range for particles with high accuracy. There are, however, several given parameters and rules with unknown and unresolved origins. One example is the strong Charge-Parity (CP) problem of why CP violation has not been observed experimentally in quantum chromodynamics (QCD), including CP symmetry breaking (Baker et al., 2006). Axion-Like Particle (ALP) is defined as pseudoscalar particles beyond the Standard Model, which is deduced from consequence of a quantum field to conserve CP symmetry in the strong interaction (Peccei & Quinn, 1977; Weinberg, 1978). The nature of dark matter requested from recent cosmological observations is not understood in the framework of the Standard Model particles. The ALP is also attractive in the frame of astrophysics, because if the density of the ALP is large enough, it fits the standard cosmology with cold dark matter (CDM). Besides, it is a possibility that ALPs are created by the collapse of other CDM-candidate particles.

The expected mass of ALP is too light to be measured directly in the present technique. An ALP converts into an observable photon by the inverse Primakoff process in an electromagnetic field. The ALP-photon conversion probability is proportional to a squared product of the magnitude of a magnetic field orthogonal to the ALP path and the length of this region, $P_{\mathrm{a}\to\gamma} \propto (B_{\perp}L)^2$, in the massless limit of an ALP (Sikivie, 1983). Several trials to detect solar-axion-origin photons, which are converted by an artificial magnetic field, have been performed. The CERN Axion Solar Telescope (CAST) is one of the experiments attempting to obtain the ALP signal produced in the Sun with "helioscope" on the ground (e.g. Andriamonje et al., 2007). The Axion Dark Matter eXperiment (ADMX) is also performed as another probe of ALP in a few μeV mass ranges, assuming that the energy density of dark matter is explained in the ALPs left over from the Big Bang (Rosenberg, 2015). However, the significant detection of ALP has not been achieved at present.

In the case of decay to ALPs from a dark matter, the isotropic distribution of ALPs is suggested. Since ALPs produce photons in a magnetic field, they should contribute to diffuse background emission in astrophysical observations of the corresponding wavelength. Even if ALPs are in isotropic distribution, the photons observed from space observatories should not be isotropic or stable. Due to the orbital motion of the observatory, the Earth's magnetic field strength in the line of sight is not stable even though the same sky region is pointed. Therefore, the contribution from ALPs in the diffuse background emission can be searched for as a modulated emission by the integrated magnetic field strength along the line

of sight. Ground-based experiments to search such effects have been performed, and possible detection by a satellite observation using Earth's magnetic fields is claimed because a long line of sight with an order of the Earth's diameter can compensate the weak magnetic field (Davoudiasl & Huber, 2006).

In this thesis, we investigate the possible contribution of ALP-originated emissions in the X-ray diffuse background, with a *Suzaku* satellite whose non-X-ray background is the lowest among the X-ray observatories in 0.5–12 keV band. In Chapter 2, we review the theoretical framework of axion and ALPs and current experimental results. In Chapter 3, we focus on the detection possibility by X-ray observatories and perform trade-off studies, and Chapter 4 shows the actual strategy and archival data selection with *Suzaku* satellite. Chapter 5 describes the observational search of a signature as the continuum emission by ALPs. In Chapter 6, the past X-ray studies of an unknown line emission are examined from the point of view of ALPs. The discussion and comparison with other studies are shown in Chapter 7, and conclusion are stated in Chapter 8.

2 Review of ALPs with X-ray Observation

2.1 Axion and ALPs from the strong CP problem in particle physics

The Charge-Parity (CP) conservation in the strong interaction is one of the unsolved questions in the quantum chromodynamics (QCD), which is the theory of strong interactions (e.g. Kim & Carosi, 2010). The QCD could provide a violation of CP symmetry, as shown in the effective QCD Lagrangian as:

$$\mathcal{L} = \theta \frac{g_s^2}{32\pi^2} G^a_{\mu\nu} \tilde{G}^{a\mu\nu}, \tag{2.1}$$

where θ is a constant parameter, g_s is the QCD gauge coupling constant, $G^a_{\mu\nu}$ is the gluon field strength, and $\tilde{G}^a_{\mu\nu}$ is its dual. Baker et al. (2006) reported that experimental bound on the electric dipole moment of neutron contributed from the Lagrangian in Equation 2.1 is $|d_n/e| < 2.9 \times 10^{-26}$ cm. From this result, the θ parameter is restricted to $< 0.7 \times 10^{-11}$ (Kim, 1987). The strong CP problem is why a θ term is unnaturally small. The most well-known solution is the Peccei-Quinn theory (Peccei & Quinn, 1977), which introduces the PQ symmetry requiring the new scalar particle called axion. The axion is a pseudo-Nambu-Goldstone boson (Weinberg, 1978; Wilczek, 1978), which has a Lagrangian as

$$\mathcal{L}_{PQ} = \frac{g_s^2}{32\pi^2} \frac{a}{F_a} G^a_{\mu\nu} \tilde{G}^{a\mu\nu}, \tag{2.2}$$

where a is the axion field, and F_a is the scale of PQ symmetry breaking. In this case, the θ parameter is rewritten with $\theta + a/F_a$. A CP potential becomes the minimum value by $\theta + a/F_a = 0$, to obtain the following QCD Lagrangian of CP-violation:

$$\mathcal{L} \to \mathcal{L}' = \left(\theta + \frac{a}{F_a}\right) \frac{g_s^2}{32\pi^2} G^a_{\mu\nu} \tilde{G}^{a\mu\nu} = \mathcal{L} + \mathcal{L}_{\rm PQ} \sim 0. \tag{2.3}$$

Eventually, the CP angle of a θ term in Equation (2.1) is adjusted to be zero without fine-tuning.

The "standard" axion based on the above PQ symmetry was not found by an experiment at an early stage, and its existence was denied. More generally, the light pseudoscalar particles beyond the Standard Model are referred to as "Axion-Like Particles" (ALPs). The coupling of an axion-like field a to two photons focused on the axion and ALP search experiments becomes

$$\mathcal{L}_{a\gamma\gamma} = \frac{g_{\rm a\gamma\gamma}}{4} F_{\mu\nu} \tilde{F}^{\mu\nu} a = g_{\rm a\gamma\gamma} \vec{E} \cdot \vec{B} a \ , \tag{2.4}$$

where $g_{a\gamma\gamma}$ is an ALP-photon coupling constant, $F_{\mu\nu}$ is the electromagnetic field tensor, $\tilde{F}^{\mu\nu}$ is its dual, and $\vec{E}$ and $\vec{B}$ are the electric and magnetic fields, respectively. This is the well known Primakoff effect, as well as the $\pi^0\gamma\gamma$ coupling. In a general ALP, the mass of ALP is not related to the ALP-photon coupling constant. Therefore, various models of ALP having high conversion are intensely investigated.

2.2 Previous works of axion and ALPs searches

Many axions are produced by the Primakoff effect at the center of the Sun. The axion flux on the Earth from the Sun is estimated at $\sim 10^{12}$ cm^{-2} s^{-1} $(m_a/\mathrm{eV})^2$. A solar axion is changed to an X-ray photon (~ 4 keV) by the process detailed in next section. CERN Axion Solar Telescope (CAST) and Sumico (at University of Tokyo) experiments are performed as an investigation for the solar axion using axion helioscope which are equipped with a 9.26 m $\times$ 9 T magnet and a 2.3 m $\times$ 4 T magnet, respectively. In Sumico experiment, Inoue et al. (2008) reported that a limit on axion-photon coupling constants is $g_{a\gamma\gamma} < 5.6 - 13.4 \times 10^{-10}$ GeV^{-1} for the $0.84 < m_a < 1.00$ eV at 95 % CL. Andriamonje et al. (2007) and Arik et al. (2014) have shown $g_{a\gamma\gamma} < 0.88 \times 10^{-10}$ GeV^{-1} for the $m_a < 0.02$ eV at 95 % CL and $g_{a\gamma\gamma} < 3.3 \times 10^{-10}$ GeV^{-1} for the $0.64 < m_a < 1.17$ eV in the CAST experiment, respectively. The International Axion Observatory (IAXO, Irastorza et al., 2013) improved the sensitivity of $g_{a\gamma\gamma} - m_a$ to overcome all previous solar searches proposed to detect solar axion and ALPs. In the case of $m_a < 10^{-5}$, axion is one of the candidates for the cold dark matter. When dark matter consists of axion, the axion is converted into a photon in the microwave with the electromagnetic interaction. Experiments through this axionic dark matter is examined in the local galactic dark matter halo have begun, such as Axion Dark Matter eXperiment (ADNX, Rosenberg, 2015). All past observations have failed to detect axion and ALPs. Carosi et al. (2013) summarized primary examples of limits for axions/ALP physical parameters, as shown in Figure 2.1.

In recent years, the detection and undetection of X-ray line emission around $E_\gamma = 3.5$ keV of unknown origin have been reported in several works. Bulbul et al. (2014) searched and detected the line signature from the spectral stacked 73 observations of galaxy clusters with *XMM-Newton*. Furthermore, Boyarsky et al. (2014) showed the weak line emissions at 3.5 keV in X-ray spectra of the M31 galaxy and the Perseus cluster observed by *XMM-Newton*. On the other hand, Urban et al. (2015) proposed that the detection of the line feature is not originated to decay from dark matter with *Suzaku*. Tamura et al. (2015) reported that the existence of the linear structure is denied with the *Suzaku* spectra of the Perseus cluster, indicating a possibility of modeling error. In blank-sky observations as the target of dark matter associated with our galaxy, both Boyarsky et al. (2014) with the *XMM-Newton* and Sekiya et al. (2014) with the *Suzaku* have not seen any significant signatures of the line

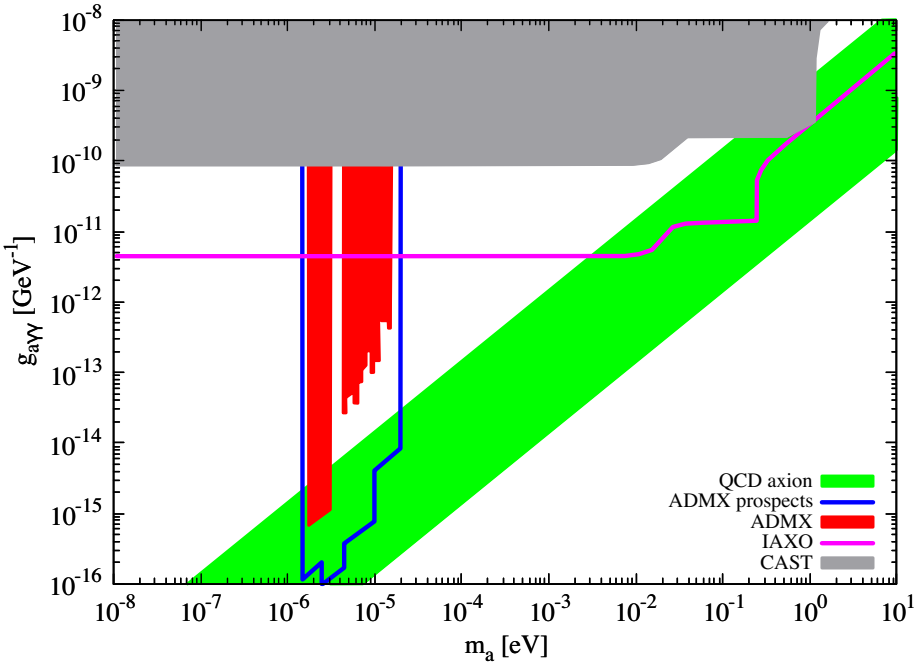

Figure 2.1 Restriction of the axion-photon and ALPs-photon coupling constant as a function of axion mass (Figure adapted from Carosi et al. (2013)).

feature.

The origin of the X-ray emission at 3.5 keV suggests that the photon is processed by not only the dark matter decay as discussed above (DM $\rightarrow \gamma$), but also the decay or magnetic conversion from dark matter through the medium of ALP (DM $\rightarrow$ ALP $\rightarrow \gamma$). Some studies (e.g. Acharya & Pongkitivanichkul, 2016) have shown that the decay of heavy moduli as a dark matter candidate produce monochromatic and relativistic ALPs. When an ALP has the energy of keV, an X-ray photon is derived from the spontaneous decay or conversion by the magnetic field in the whole Universe. Cicoli et al. (2014), Conlon & Day (2014), and Conlon & Powell (2015) proposed that the dark matter associated with clusters or galaxies decays to ALPs, and the X-ray line emission is converted from ALPs by inverse Primakoff effect in the cluster or galaxy magnetic field.

We can estimate the ALP spectrum by the decay of the unknown particles as the candidate of dark matter; an example is the moduli, associated with local structure (e.g. galaxy) or whole universe in a uniform. Through the two-body decay case: DM $\rightarrow$ 2 ALPs, the ALP has the monochromatic energy $E_a = m_\phi/2$, where m_ϕ is the mass of dark matter. The emissivity of the DM $\rightarrow$ 2 ALPs process is simply expressed by the energy density of dark matter, $\rho_\phi(r)$, the decay rate, $\Gamma_{\phi\rightarrow 2a}$, and m_ϕ:

$$\epsilon_a = \frac{2\rho_\phi(r)\,\Gamma_{\phi\rightarrow 2a}}{m_\phi}. \tag{2.5}$$

For the dark matter distributed locally, the ALP intensity, which has a monochromatic spectrum, $I_{a,\mathrm{line}}$ [counts s^{-1} cm^{-2} sr^{-1}], is estimated as:

$$I_{a,\mathrm{line}} = \int_{\mathrm{l.o.s.}} \frac{2\Gamma_{\phi\to 2a}}{4\pi m_\phi}\rho_\phi\left(r\right)\, dr = \frac{S_\phi \Gamma_{\phi\to 2a}}{2\pi m_\phi} \quad \left(E_a = m_\phi/2\right), \tag{2.6}$$

with

$$S_\phi = \int_{\mathrm{l.o.s.}} \rho_\phi(r)\, dr, \tag{2.7}$$

where S_ϕ is dark matter column density (Sekiya et al., 2016). However, when dark matter distributed over the universe uniformly is assumed, we observe the continuum spectrum of the superposition of such monochromatic spectrum due to the effect of cosmological redshift. Kawasaki & Yanagida (1997) and Asaka et al. (1998) described the photon flux from the decay of the uniform moduli. Since the ALP is very light or massless, ALP also undergoes the effect of a cosmic expansion similar to a photon. According to this literature, the ALP intensity integrated into line spectra from the past to today is given by:

$$\frac{dN}{dE_a} = \int_{\mathrm{l.o.s.}} \frac{\Gamma_{\phi\to 2a}}{4\pi m_\phi}\rho_\phi\left(r\right) dr \times 2\delta\left(E_a\left(1+z\right) - m_\phi/2\right) \tag{2.8}$$

$$= \frac{\sqrt{2}c\Gamma_{\phi\to 2a}\rho_{\phi_0}}{\pi H_0}\; m_\phi^{-\frac{5}{2}}\; E_a^{\frac{1}{2}}\; f\left(\frac{m_\phi}{2E_a}\right) \tag{2.9}$$

where ρ_{ϕ_0} is the present energy density, z is the redshift, H_0 is present Hubble constant, and $f\left(x\right)$ denotes the function of Ω_{m0} and $\Omega_{\Lambda 0}$ are the density parameter of the matter and the cosmological constant, respectively:

$$f(x) = \left\{\Omega_{m0} + \left(1 - \Omega_{m0} - \Omega_{\Lambda 0}\right)/x - \Omega_{\Lambda 0}/x^3\right\}^{-\frac{1}{2}}. \tag{2.10}$$

The spectral shape of ALPs is transcribed as a simple power-law function whose power of a number is 1/2, which is the photon index of $-1/2$.

2.3 Possibility of ALPs search with X-ray observatory

Davoudiasl & Huber (2006, 2008) proposed that the method of searching for solar axion occurs not through an artificial magnetic field but through a geometric field with an X-ray satellite. By using a magnetic field spreading beyond the Earth's radius, the axion-photon conversion rate proportional to $(B_\perp L)^2$ described in Chapter 3, becomes several times by a ground experiment as shown in Table 2.1. The detection of a seasonal fluctuation of X-ray background depending on Earth's magnetic field is reported by Fraser et al. (2014) with *XMM-Newton*. According to the paper, the X-ray flux of 4.6×10^{-12} erg s^{-1} cm^{-2} deg^{-2} in 2–6 keV has been interpreted by the solar axion from geomagnetic conversion, which has 2.2×10^{-22} GeV^{-1} for an axion mass in the μeV range. However, Roncadelli & Tavecchio (2015) proposed not to relate this background with axions produced by the Sun. To preserve

the momentum of the photon by the Primakoff process in case of relativistic ALP, the *XMM-Newton* satellite cannot observe the photon originated from solar ALP because it never points toward the Sun. Roncadelli & Tavecchio (2015) showed that the observational result in Fraser et al. (2014) cannot be explained by this origin from the solar ALP, though the study does not mention the origin of the X-ray signal.

When ALPs are all or partly dark matter, there is radiation from a whole sky on the celestial spheres. Several cases can be considered. If dark matters distribute isotropically in the Universe and decay to axions or ALPs, it can be converted to photons by magnetic fields. Asaka et al. (1998) showed that the expected photon energy spectrum follows a power-law with a photon index of $-1/2$ as shown in Equation (2.9). If dark matters directly convert to photons, an emission line with fixed energy is expected. In both cases, these emissions should be regarded as a part of the diffuse background in the corresponding wavelength at present observations. In X-ray band, Sekiya et al. (2016) set the tightest upper limits for line emission between 1 and 7 keV. If the observations are performed by space observatories, the strength of the electromagnetic field in the line of sight is not constant, due to their orbital motion around the Earth. It means that the diffuse background emission originating from axions and ALPs cannot be stable and could be considered not to be isotropic. It is a novel technique to search for the axion and ALP signature. We will investigate these possibilities in detail in the next chapter.

Table 2.1 Summary of $B_\perp L$ values in experiments and studies for ALP search

Reference	Telescope	Magnet source	Target	$B_\perp L$ [Tm]
Inoue+2008	Sumico	superconducting magnet	solar axion	9.2
Arik+2014	CAST	superconducting magnet	solar axion	83
Rosenberg+2015	ADMX	superconducting magnet	dark matter axion	8.5*
Davoudiasl+2008	X-ray satellites†	Earth	solar axion	~ 20
Cicoli+2014	*XMM-Newton*	cluster core	ALP (from 3.5 keV)	$\sim 10^{11}$
Conlon+2014	*XMM-Newton*, *Chandra*	Milky Way and M31	ALP (from 3.5 keV)	$\sim 10^{9}$
This thesis	*Suzaku*	Earth	ALPs	80-300

* The RF cavity of 0.5 m diameter × 1.0 m long is in the bore of an 8.5 T solenoid magnet.

† A detection possibility of solar axion was investigated about 55 satellite orbits.

3 Method to detect ALPs by X-ray observations

3.1 Overview of procedure

As a new effective approach for detecting axion-like particles(ALPs), we adopted a method observing the signal converted to an X-ray photon by the Earth's magnetic field with a satellite. The conversion probability of ALPs into a photon, $P_{\mathrm{a}\to\gamma}$, is directly proportional to $(BL)^2$, where $B = |\vec{B}|$ and L is the length of the magnetized region in the next section (Section 3.2). Given the realistic satellite orbits, it is possible to estimate the geomagnetic conversion of ALPs, as well as the case of solar axions shown in Davoudiasl & Huber (2006, 2008).

The spectral shapes of ALPs have two possibilities: a line emission and a continuum such as a power-law. Sekiya et al. (2016) gave the tightest line detection limit in the X-ray diffuse background (XDB) with blank sky data of the *Suzaku* satellite. Based on the data set in Sekiya et al. (2016), we could estimate the line emission limit from ALP, and obtain the upper limit of ALP-photon coupling constant. Applying a similar study by Sekiya et al. (2016) is a straightforward approach to examine the contribution from ALPs to XDB for detection of a continuum. In this chapter, we considered these points of view and found the best approach for this search.

3.2 Probability of ALPs - photon conversion

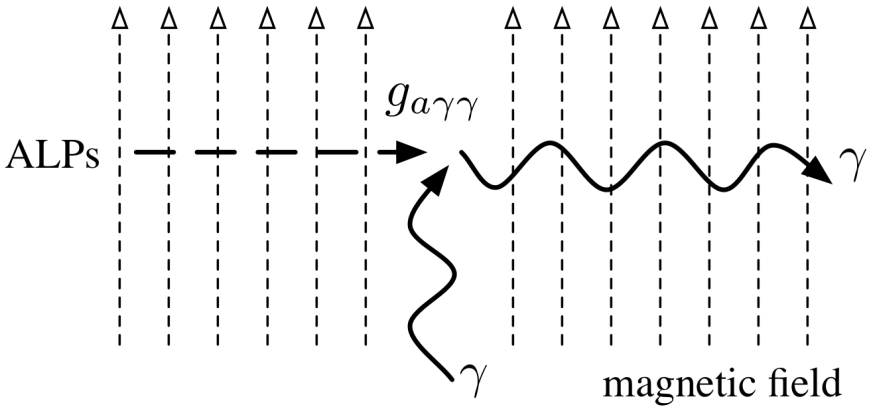

Figure 3.1 A diagram of ALP-photon conversion in a magnetic field via the inverse Primakoff process

ALP can be detected by photons converted through an interaction with the external electromagnetic field called inverse-Primakoff effect. The Lagrangian of the ALP in an electromagnetic field is

$$\mathcal{L} = -\frac{1}{4}F_{\mu\nu}F^{\mu\nu} + \frac{1}{2}(\partial_\mu a\ \partial^\mu a - m_a^2 a^2) + \frac{g_{\mathrm{a}\gamma\gamma}}{4} a F_{\mu\nu}\tilde{F}^{\mu\nu}, \tag{3.1}$$

where m_a is ALP mass, $g_{\mathrm{a}\gamma\gamma}$ is ALP-photon coupling constant, $F_{\mu\nu}$ is the electromagnetic field tensor, and $\tilde{F}_{\mu\nu}$ is its dual. We can calculate the ALP-photon conversion rate in a vacuum and a uniform magnetic field $\vec{B}$. Raffelt & Stodolsky (1988) proposed that only the photon component which has the polarization parallel to the magnetic field mix with ALP. When we assume that the fields plane-wave solutions $\exp(i(\omega t - kz))$, the relevant wave equation is

$$i\partial_z \begin{pmatrix} A \\ a \end{pmatrix} = \begin{pmatrix} \omega & g_{\mathrm{a}\gamma\gamma}B/2 \\ g_{\mathrm{a}\gamma\gamma}B/2 & \omega - m_a^2/2\omega \end{pmatrix} \begin{pmatrix} A \\ a \end{pmatrix} \tag{3.2}$$

where A is the amplitude of the "parallel" photon component and the magnitude of the axion-like field (van Bibber et al., 1989). From a first-order perturbative solution, we obtain the amplitude of transition rate written as follows:

$$\langle A(z) \,|\, a(0)\rangle = \frac{g_{\mathrm{a}\gamma\gamma}}{2}\int_0^z dz' \,|B_\perp| \exp\left(-i\frac{m_{\mathrm{a}}^2}{2\omega}z'\right). \tag{3.3}$$

The ALP-photon conversion probability in a vacuum is given by van Bibber et al. (1989)

$$\begin{aligned} P_{\mathrm{a}\to\gamma}(t,z) &= |\langle A(z) \,|\, a(0)\rangle|^2 \\ &= \left|\frac{g_{\mathrm{a}\gamma\gamma}}{2}\int_0^z B_\perp(z',t)\exp\left(-i\frac{m_{\mathrm{a}}^2}{2E_{\mathrm{a}}}z'\right)dz'\right|^2, \end{aligned} \tag{3.4}$$

with

$$B_\perp(z',t) \equiv \left|\vec{B}(z',t)\times\vec{e}_{\mathrm{a}}(t)\right|. \tag{3.5}$$

Here, E_{a} is the ALP energy and $B_\perp(z,t)$ is the magnitude of a magnetic field orthogonal to the ALP path $\vec{e}_{\mathrm{a}}$. The ALP-photon momentum transfer q is defined as:

$$q = \frac{m_{\mathrm{a}}^2}{2E_{\mathrm{a}}}, \tag{3.6}$$

where m_{a} is the ALP mass in vacuum. Assuming the $B_\perp(z',t)$ is uniform in the range of $0 < z' < L$, we can write Eq. (3.4) as:

$$P_{\mathrm{a}\to\gamma} = \left(\frac{g_{\mathrm{a}\gamma\gamma}B_\perp}{2}\right)^2 2L^2\ \frac{1-\cos(qL)}{(qL)^2}. \tag{3.7}$$

In the limit of vanishing ALP masses $m_a \to 0$, the conversion rate is simply given by

$$P_{\mathrm{a}\to\gamma} = \left(\frac{g_{\mathrm{a}\gamma\gamma}B_\perp L}{2}\right)^2. \tag{3.8}$$

Hence, the conversion probability of ALP into a photon is directly proportional to $(B_\perp L)^2$ in the massless limit. For example, in an orbital observation utilizing the Earth's magnetic field, Eq. (3.8) becomes

$$P_{\mathrm{a}\to\gamma} \simeq 2.45\times10^{-21}\ \left(\frac{g_{\mathrm{a}\gamma\gamma}}{10^{-10}\ \mathrm{GeV}^{-1}}\right)^2\left(\frac{B_\perp}{\mathrm{T}}\right)^2\left(\frac{L}{\mathrm{m}}\right)^2. \tag{3.9}$$

$$= 2.45\times10^{-21}\cdot g_{10}^2, \tag{3.10}$$

where $g_{10} = g_{\mathrm{a}\gamma\gamma}/10^{-10}\ \mathrm{GeV}^{-1}$. If the ALP has a finite mass, $1-\cos(qL)$ is not equal to $(qL)^2/2$ in Eq. (3.7). That is to say, the coherence condition

$$qL < \pi\ \rightarrow\ m_{\mathrm{a}} < \sqrt{\frac{2\pi E_{\mathrm{a}}}{L}} \tag{3.11}$$

is restricting the sensitive mass range of ALPs. The conversion X-ray count rate in an energy range $E, E+dE$ is replaced by

$$\mathrm{CR}(E) = S\Omega\frac{dF_a}{dE}P_{\mathrm{a}\to\gamma}\ dE \quad \text{photons s}^{-1} \tag{3.12}$$

where S is an effective area of an instrument, Ω is an effective solid angle, and dF_a/dE is ALPs flux.

3.3 Understandings of X-ray Diffuse Background

In the whole sky, there is X-ray diffuse emission, even if we observe blank sky which has no apparent X-ray source. The X-ray Diffuse Background (XDB) consists of the radiation from hot gas in the Milky Way and extragalactic point sources. Additionally, emissions from ALPs may contribute if they exist. The model spectrum of the XDB has been investigated by previous works (e.g. Yoshitake et al. (2013)). The emission model of XDB is composed of the following components:

1. The Local Hot Bubble (Snowden et al., 1990) and Solar Wind Charge Exchange (Yoshitake et al., 2013)
2. The hot interstellar medium of Milky Way Halo (Yao et al., 2009; Sakai et al., 2014)
3. The extra-galactic unresolved point sources called the Cosmic X-ray Background (Kushino et al., 2002; Smith et al., 2007)
4. High-temperature component (Sekiya et al., 2014)

The blend of the Local Hot Bubble (LHB) and Solar Wind Charge Exchange (SWCX) corresponds to an unabsorbed thermal plasma with $kT \sim 0.1$ keV. The LHB has been considered a hot and thin gas around our Solar system with a temperature of 10^6 K (Snowden et al., 1990) led by the explosion of supernovae. The SWCX is radiation from the electric charges exchanging reactions between a highly ionizing ion from Solar wind and a neutral

particle in near-Earth. Although a collisional ionization equilibrium (CIE) plasma is different from the physical process of line emission from SWCX, we adopted a single component of CIE plasma as well as previous works e.g. (Yoshino et al., 2009; Yoshitake et al., 2013) in this thesis.

The Milky Way Halo (MWH) is a hotter spherical gas which spreads from the galactic disk. This interstellar medium is represented by an absorbed CIE plasma with a temperature of $kT = 0.2 - 0.4$ keV and density of $\sim 10^{-3}\mathrm{cm}^{-3}$ (Yao et al., 2009; Sakai et al., 2014).

Mushotzky et al. (2000) and Moretti et al. (2003) show that the Cosmic X-ray Background (CXB) is an extra-galactic emission stacked with a lot of faint point sources, such as active galactic nucleus (AGN). The origin at $\sim 80\%$ of total CXB has been reported to be a discrete source resolved by observations of *Chandra* and *XMM-Newton*. The emission model of CXB is represented by a power-law with its photon index of $\Gamma = 1.4$ (Kushino et al., 2002) or modified power-law functions (Smith et al., 2007).

In recent years, some studies have shown that the High-Temperature Component (HTC) exists in some locations (Sekiya et al., 2014). This can be interpreted through the hot and optically thin plasma with a temperature of $kT \sim 1$ keV. Little is known about the origin, physical size, density, and distance of HTC.

In the study of this thesis, "SWCX+LHB"+"Galactic absorption"×("MWH" + "CXB" + "HTC") is applied as the model of XDB emission for ALPs search.

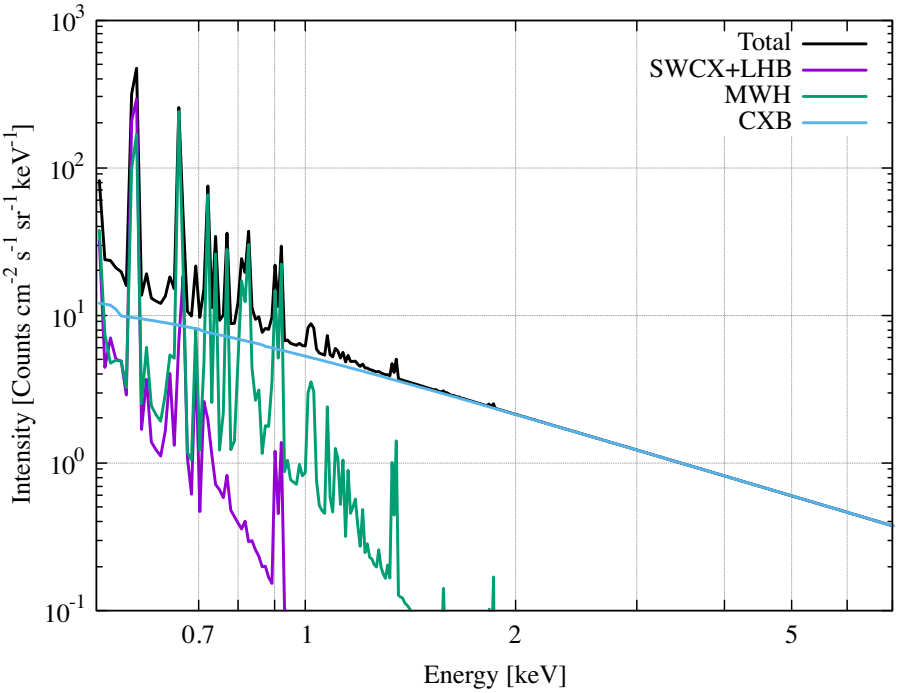

Figure 3.2 Typical photon spectrum of X-ray diffuse emission. Note that detector response function, and energy resolution are not taken into account.

3.4 Satellite/Instrument selection

To investigate faint X-ray flux originating from ALPs, the most sensitive method is an observation by an imaging spectrometer, such as a CCD camera, located on an X-ray observatory. We compared the instruments of three X-ray satellites, *Suzaku*, *XMM-Newton*, and *Chandra*. Table 3.1 summarizes the orbital parameters and a performance characteristic of each CCD camera.

The contribution of the CXB flux is dominant on the 2–10 keV energy band. Picking up the component depending on $P_{a\to\gamma}$, distinguished from the CXB, is required. Therefore, not only the good stability of background but also the large variation of the conversion rate in each observation are of great importance. To accurately estimate ALPs-photon conversion rate, we must calculate the magnitude of the magnetic field vertical to the line-of-sight in Equation (3.8). In the case study of solar axion in *XMM-Newton* orbit (Figure 3.3), Fraser et al. (2014) reported that the calculated amplitude of the seasonal variation of geomagnetic conversion of axion is by a factor of ~ 2. The fluctuation of the CXB due to the stack of various observations and the ambiguity of the interplanetary magnetic field must be considered as a systematic uncertainty. In *Suzaku* orbit (Figure 3.4), due to the observation from the inside of the Earth's magnetic field, the ALPs-photon conversion changes by a factor of ~ 5 in the same line-of-sight.[*1] It is also advantageous to expect a low and stable non-X-ray background (NXB) with *Suzaku*/XIS (Table 3.1). The uncertainty in the detector background is expected to be smaller than the variation of the geomagnetic conversion of ALPs caused by orbital motions. In this thesis, *Suzaku*/XIS is to be adopted for the search to the continuum from ALPs.

[*1] Detailed description in Chapter 5

Table 3.1 Summary of orbit and CCD imaging spectrometer on X-ray observatories.

Satellite	*Suzaku*	*XMM-Newton*	*Chandra*
Orbit	low earth	highly elliptical	highly elliptical
Perigee [km]	524	7.0×10^3	13.2×10^3
Apogee [km]	531	113.8×10^3	135.7×10^3
Inclination [deg]	31.38	66.17	76.9
Period [min]	95.19	2861.59	3809.54
CCD name	XIS	MOS+PN	ACIS-I (FI)
			ACIS-S(FI/BI)
Field of view	$17'.8 \times 17'.8$	$30'$ in diameter	$16' \times 16'$
Energy range [keV]	0.2–12	0.1–15	0.5–12
Effective area $[\mathrm{cm}^2]$	390 at 1.5 keV (BI)	922 at 1 keV (2MOS)	380 at 4 keV
		1227 at 1 keV (PN)	
NXB *	1–10	5–100	10–1000

* In unit of $\mathrm{cm}^{-2}\ \mathrm{s}^{-1}\ \mathrm{sr}^{-2}\ \mathrm{keV}^{-1}$.

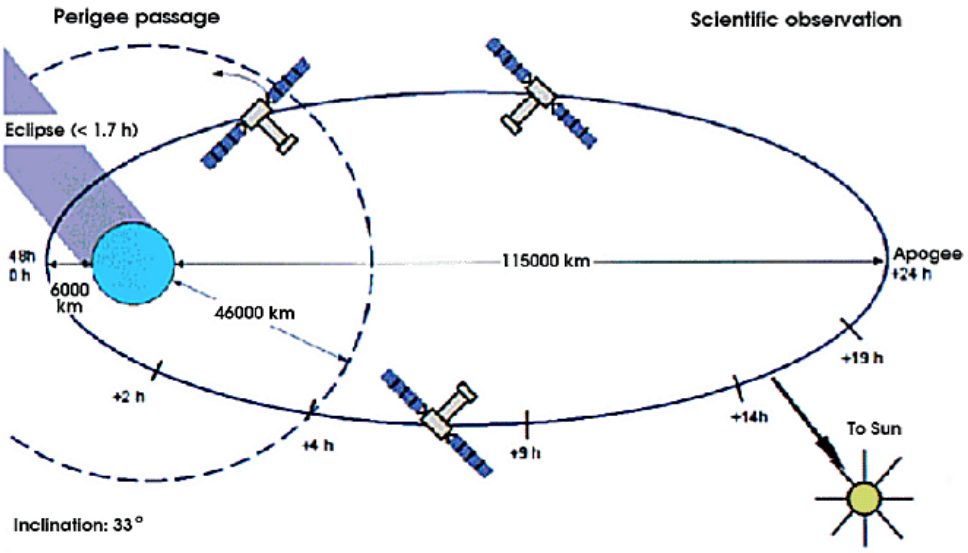

Figure 3.3 Schematic drawing of the *XMM-Newton* orbit. Original figure provided by Dornier Satellitensysteme GmbH. *XMM-Newton* Users Handbook (https://heasarc.gsfc.nasa.gov/docs/xmm/uhb/XMM_UHB.html).

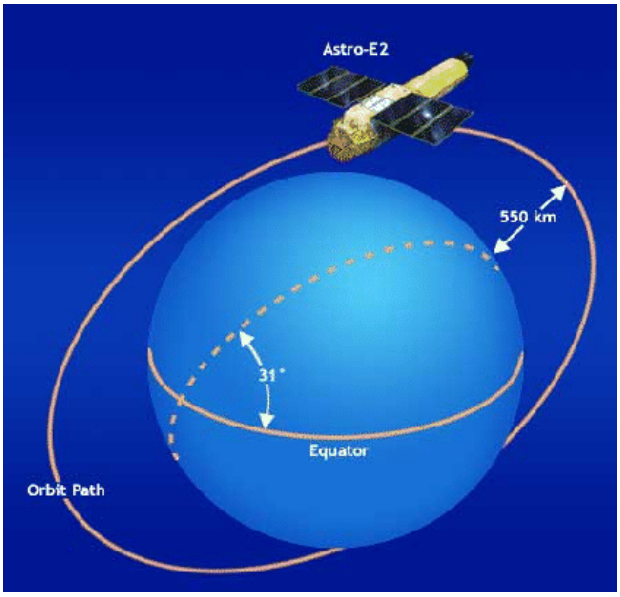

Figure 3.4 The *Suzaku* in low earth orbit. The *Suzaku* Technical Description (http://www.astro.isas.ac.jp/suzaku/doc/suzakux_td/).

4 Strategy to search for ALPs signature with *Suzaku*

4.1 Over view of XRT-XIS modules on *Suzaku*

4.1.1 *Suzaku* satellite

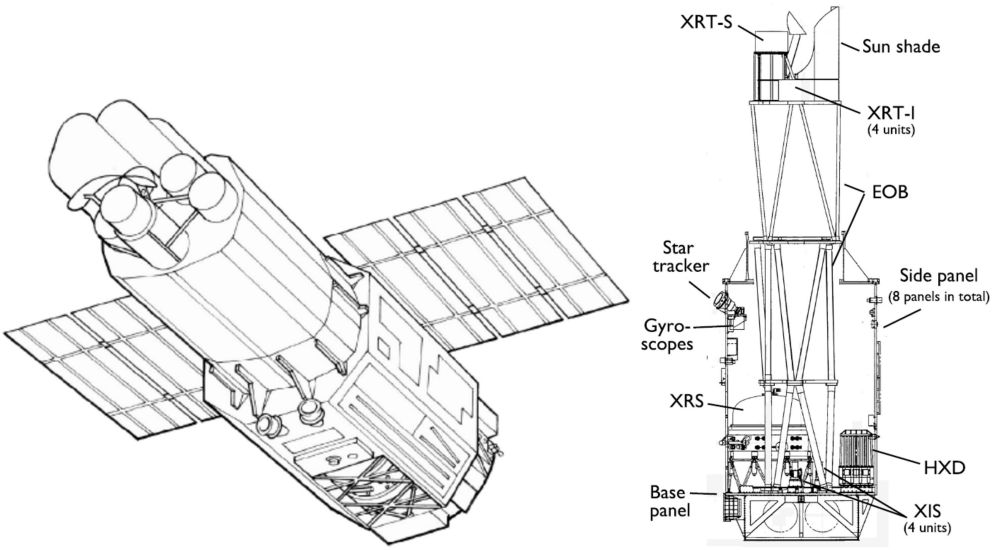

Figure 4.1 Overview of *Suzaku* satellite (Mitsuda et al., 2007, Figure 1. & Figure 2.).

Suzaku is the fifth Japanese X-ray astronomy satellite (Mitsuda et al., 2007), which was launched by the M-V rocket from the Uchinoura Space Center on 2005 July 10. This size is a diameter of 2.1 m and a total length of 6.5 m in Figure 4.1. *Suzaku* was put into a near-circular orbit at an altitude of 568 km, an inclination of 31.9 degrees, and a period of about 96 minutes. Since the satellite operation could not be continued due to battery depletion, the observation lasting for 10 years on 2015 August 26 ended. The *Suzaku* has two instruments for observing the very wide energy band from 0.2 to 600 keV. One of those consists of four pairs, which include an X-Ray Telescope (XRT, Serlemitsos et al., 2007) as a reflecting mirror and an X-ray Imaging Spectrometer (XIS, Koyama et al., 2007) as a focal plane detector. The other is a Hard X-ray Detector (HXD, Takahashi et al., 2007) for gamma-ray observation from 10 keV to 600 keV. HXD is not used in this thesis.

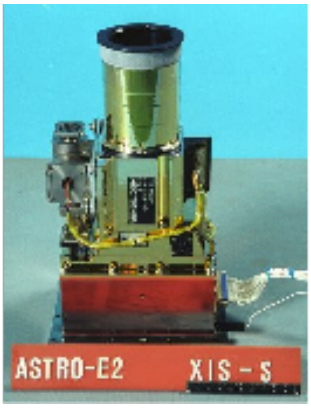

Figure 4.2 Pictures of XRT and XIS onboard *Suzaku*

4.1.2 XRT-XIS module

Suzaku has 4 XRT-XIS modules for soft X-ray observation. The XRT is a thin-foil-nested Wolter-I type telescope, which consists of two reflecting surfaces of the hyperboloid and paraboloid (Figure 4.2). In XRT, the optics with two conical approximations is used. The XIS composed of 4 CCDs with the sensitivity in soft X-rays (Figure 4.2). The breakdown is three front-illuminated (FI: energy range 0.4–12 keV) and one back-illuminated (BI: energy range 0.2–12 keV). The radiation source of ^{55}Fe for the energy calibration is installed. The details of the XRT and XIS performance are summarized in Table 4.1. Since one of the CCDs showed an anomaly on 9 November 2006, the observation by XIS2 was stopped.[*1] In this thesis, we used two of FI-CCDs (XIS0, 3) and one of the BI-CCD (XIS1).

4.1.3 Instrumental background of *Suzaku*/XIS

The instrumental background events of *Suzaku*/XIS originated from the cosmic rays and the X-ray fluorescence event that excited structures of the satellite by the cosmic rays, called Non-X-ray background (NXB). In order to remove the events of the charged particles, the observed events are classified into eight grades by the spread of CCD pixels as shown in Figure 4.3. In the case of *Suzaku*/XIS, the events of Grade 0, 2, 3, 4, and 6 are regarded as X-ray events because the events caused by cosmic rays spread more than 2×2 pixels (Yamaguchi et al., 2006). The instrumental backgrounds that cannot be eliminated by the "*ASCA* Grade method" are stacked from night Earth (NTE) observations, i.e., the *Suzaku*'s field of view is completely filled by night (not sunlit) Earth where the celestial X-ray emission is occulted and the scattering of atmospheric X-rays does not reach XISs. A NXB database of *Suzaku*/XIS is constructed from NTE events. The spectrum of the NXB consists of several

[*1] http://www.astro.isas.jaxa.jp/suzaku/doc/suzakumemo/suzakumemo-2007-08.pdf

Table 4.1 Performance of XRT-XIS module (first step guide)

XRT	Focal distance	4.75 m
	Field of view	17' at 1.5 keV, 13' at 8 keV
	Effective area	440 cm^2 at 1.5 keV, 250 cm^2 at 8 keV
	Angular resolution	2' (Half Power Diameter)
XIS	Field of view	$17.8' \times 17.8'$
	Energy range	0.2–12 keV
	Pixel number	1024×1024
	Size of pixel	24 μm $\times$ 24 μm
	Energy resolution	$\sim$ 130 eV at 6 keV
	Time resolution	8 s
XRT-XIS	Effective area	340 cm^2(FI), 390 cm^2(BI) at 1.5 keV
		350 cm^2(FI), 100 cm^2(BI) at 8 keV

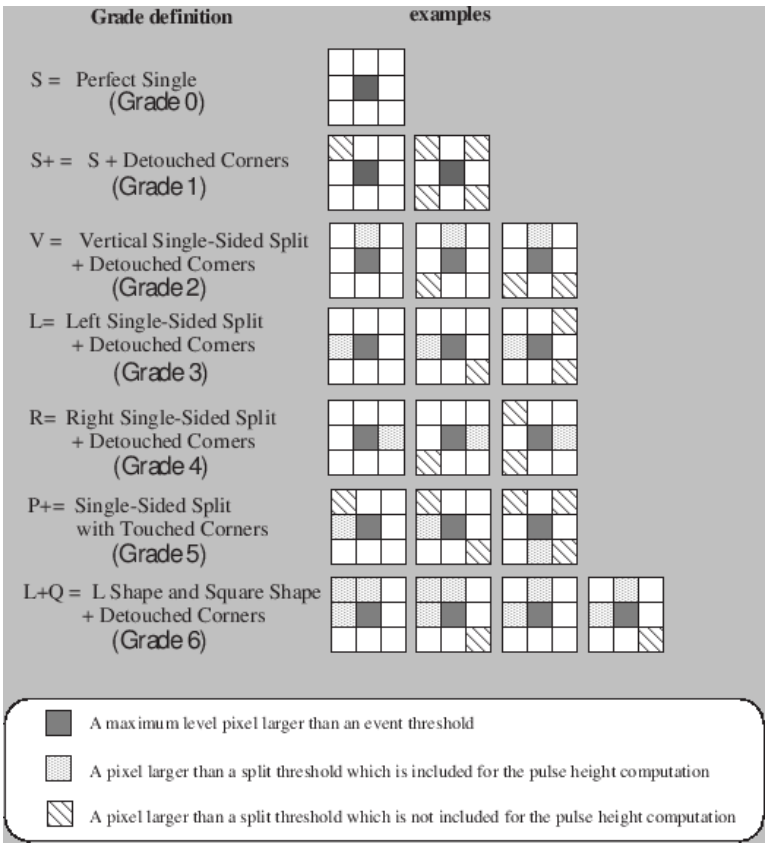

Figure 4.3 *ASCA* grade method (The *ASCA* Data Reduction Guide: http://heasarc.gsfc.nasa.gov/doc/asca/abc/)

emission lines and a continuum as shown in Figure 4.4. Since the pixel expansion for high

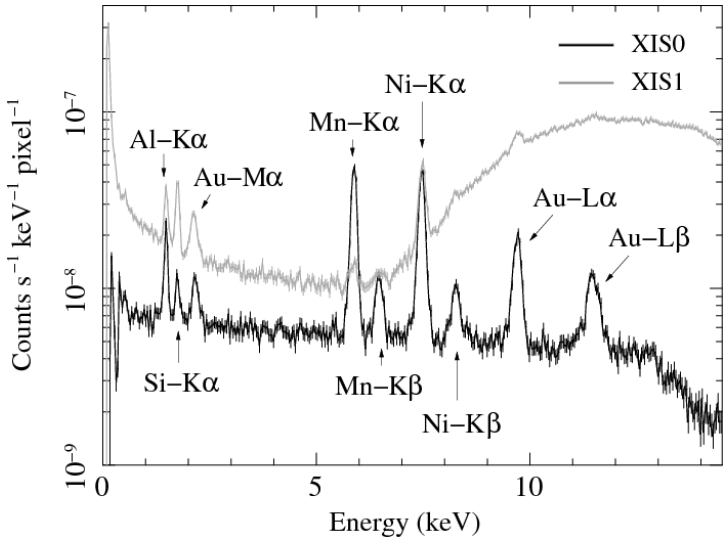

Figure 4.4 Spectra of NXB in FI-CCD (XIS0) and BI-CCD (XIS1) with 1024×1024 pixels (Tawa et al., 2008, Figure 1.). The spectra consists of X-ray fluorescence summarized in Table 4.2 (Yamaguchi et al., 2006; Tawa et al., 2008) and continuum emission caused by interaction of cosmic rays with the satellite structure (Murakami et al., 2006).

energy particles is smaller in BI-CCD than in FI-CCD, it is difficult to distinguish from X-ray events by the *ASCA* Grade method. Therefore, the NXB count rate of the BI is larger than that of the FI-CCD, especially at high energy region. The energies of line emissions are summarized in Table 4.2. These line emissions are identified as characteristic X-ray lines from materials in the XIS and XRT (Yamaguchi et al., 2006).

Table 4.2 Energies and origins of line emissions of the NXB spectra (Yamaguchi et al., 2006; Tawa et al., 2008)

Lines	Energy[keV]	Origin
Al-Kα	1.486	Optical bloking filter, housing, XIS substrate
Si-Kα	1.740	XIS (Si flurescence)
Au-Mα	2.123	Housing, XIS substrate, heat-sink
Mn-Kα	5.895	Calibration source
Mn-Kβ	6.490	Calibration source
Ni-Kα	7.470	Housing, heat-sink
Ni-Kβ	8.265	Housing, heat-sink
Au-Lα	9.671	Housing, XIS substrate, heat-sink
Au-Lβ	11.51	Housing, XIS substrate, heat-sink

Murakami et al. (2006) shows by the GEANT4 Monte-Carlo simulation that the NXB spectral shape of the continuum emission can be explained by the the cosmic ray interactions with the components of the XISs. They assumed the spectral shape of the cosmic rays at the *Suzaku* altitude shown in Figure 4.5. Figure 4.6 shows the simulated and observed NXB

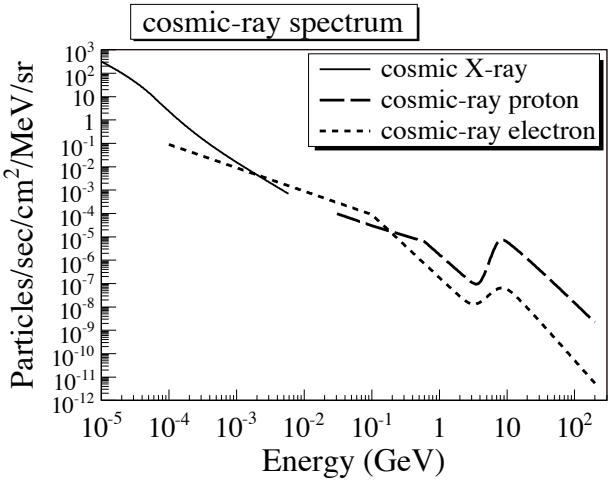

Figure 4.5 The spectra of cosmic rays (Murakami et al., 2006, Figure 4.). They ignored neutrons and ions heavier than H^+. Using this spectra as input, the XIS signals are calculated by the Monte Carlo simulation.

spectra after applying the *ASCA* Grade method. The continuum component of the NXB

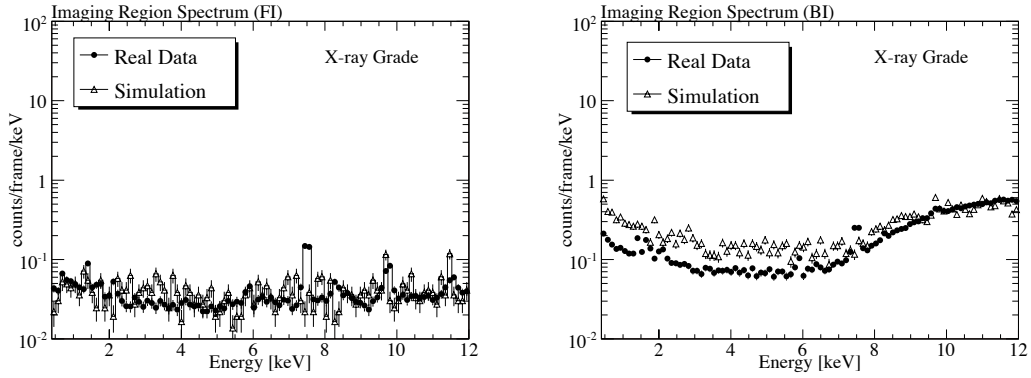

Figure 4.6 The continuum component of simulated and observed NXB spectra (Murakami et al., 2006, Figure 1. upper). After *ASCA* Grade method is applied, the observed spectral shapes of both FI-CCD and BI-CCD are reproduced by their simulation with accuracy of ~ 20 %.

can be interpreted as the instrumental background originating from the cosmic ray. The level of the entire NXB spectrum varies depending on the intensity of cosmic rays. Tawa et al. (2008) sorted the NTE events by Cut-off-Rigidity (COR) at the *Suzaku* orbit and confirmed that the NXB count rate depends on the COR as shown in Figure 4.7. The

COR values were calculated using the Corrected Geomagnetic Coordinates (CGM) model T96 called the "COR2" in the calibration database of *Suzaku*. Based on these studies, a standard method to estimate the NXB during the sky (celestial target and diffuse background emission) observation is designed. Details of this method are described in Section 5.2. We note that the count rates of the NXB and typical X-ray background are compatible, and the reproducibility of the NXB is the main factor of systematic uncertainty. Tawa et al. (2008) stacked 300-day NTE data to reduce the Poisson errors and reported that the reproducibility of the NXB count rates for the typical 50 ks observation were 3.4 % in 1–7 keV band including both continuum and line emission. Archived NTE database and software are public in the *Suzaku* analysis.

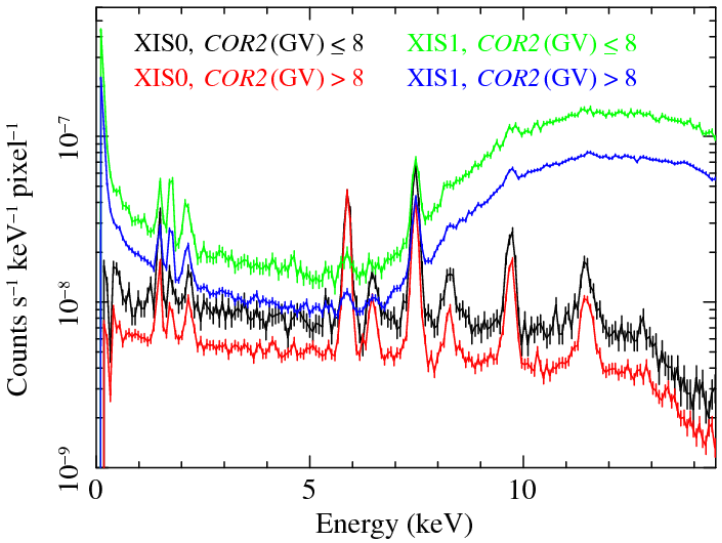

Figure 4.7 The COR dependence of NXB spectra in COR2 $\leq$ 8 GV/c and 8 $<$ COR2 GV/c. (Tawa et al., 2008, Figure 3 right.) Black and red lines indicate the XIS0. Green and blue lines indicate the XIS1. The spectral level in COR2 $\leq$ 8 GV/c is higher than that in 8 GV/c $<$ COR2.

The ratio of the typical spectra of NXB and XDB is $\sim$ 1 in the energy band of 2 to 5 keV. Thus, the reproducibility of the NXB restricts the sensitivity of the ALPs search as a system error. The NXB spectrum is calculated from the means of the weighted sum of the NTE spectra during 300 days by taking into account a long-term variation of the *Suzaku* orbit. We have to evaluate the effect of the short-term variation of the cosmic ray intensity as a systematic error. The standard estimation method of NXB spectra by COR is described in Chapter 5.3.

4.2 Magnetic field model of the Earth

We use the International Geomagnetic Reference Field:the 12th generation (IGRF-12, Thébault et al., 2015) as a mathematical model of terrestrial magnetism. The IGRF is represented by a spherical harmonic expansion, whose coefficients are determined from magnetic observatories, ground surveys around the world, and low Earth-orbiting satellites. The coefficients have been higher order from 10 to 13 since 2000 and have made the model accuracy of ~ 0.01 nT since 2005. This model is not suitable to compute the magnetic field vector of local phenomena, such as a magnetic storm. However, it is a promising model to investigate the magnetic field situation in a low Earth orbit.

4.3 Geomagnetic conversion of ALPs in the *Suzaku* field of view

To detect on the ALPs flux with the satellite data, the magnetic flux in the field of view on a position in a geographic coordinate system is integrated along a line of sight from Equation (3.4) in the coherent condition (Equation (3.11)). In the case of the *Suzaku* observation, geomagnetic conversion of ALPs at $\vec{x}$ is rewritten as

$$P_{\mathrm{a}\to\gamma}\left(\vec{x}\right) \simeq \left| \frac{g_{\mathrm{a}\gamma}}{2} \sum_{n=0}^{N} \left(\vec{B}_{\mathrm{E}}\left(\vec{z}\right) \times \vec{l} \right) dL \right|^2 , \tag{4.1}$$

$$\vec{z} = \vec{x} + \left(n \cdot dL\right) \vec{l} \tag{4.2}$$

where $\vec{B}_{\mathrm{E}}\left(\vec{z}\right)$ is a magnetic field, $|\vec{B}_{\mathrm{E}}\left(\vec{z}\right) \times \vec{l}| \equiv B_{\perp}$ is the transverse magnetic field along the line of sight, $\vec{l}$ is a unit vector of the line of sight, and $N \cdot dL = L_{\max}$ is a boundary of the Earth's magnetic field.

The orbit of *Suzaku* is calculated by reference to the "*atFunctions*,"[*2] which is a C library of basic functions developed for the orbit and attitude calculation of the *ASCA* satellite. *atFunctions* has been used for the *Suzaku* operation in the Uchinoura space center. In this thesis, all position vectors during the 10-year *Suzaku* operation are calculated every 60 seconds from orbital elements. According to Equation (4.1) in the geocentric coordinate system bound to the Earth, the geomagnetic conversion rate is determined when dL is 10 km.

Figure 4.8 indicates calculation samples when the *Suzaku* satellite is on the equator. As a typical example, we compute two cases of line-of-sights orthogonal (e.g. A383) and parallel (e.g. NEP) to the magnetic pole. The results of the calculation applied by IGRF-12 is shown

[*2] http://www.darts.isas.ac.jp/pub/legacy.gsfc.nasa.gov/software/lheasoft/lheasoft6.0.4/headas/attitude/lib/atFunctions/

in Figure 4.9. The magnitude of Earth's magnetic field becomes $< 1/100$ in $L_{\rm max} \simeq 6{\rm R_E}$. In the case of A383, $|\vec{B}_{\rm E} \times \vec{l}|$ is equal to $|\vec{B}_{\rm E}|$. On the contrary, the vertical component is smaller than the magnetic field strength in the observation of NEP. From the above magnetic flux, we estimate the ALPs-photon conversion $P_{\rm a\to\gamma}$ about various momentum transfers in Equation (3.6). In the all q value, Figure 4.10 shows that $P_{\rm a\to\gamma}$ converges on a constant value above $\sim 5{\rm R_E}$. Moreover, that is a maximum value when q is close to the coherent condition (Equation (3.11)). We adopt the distance limit $L_{\rm max}$ of $\sim 6{\rm R_E}$ from the center of the Earth. In this case, we are sensitive to $m_a \sim 10^{-6}$ eV, where m_a is the mass of ALP. Thus, the photon generation efficiency, $P_{\rm a\to\gamma}$, by ALPs in the field of view (FoV) depends on the position and observing direction of the satellite in its orbit relative to the Earth. It will show time variability in contrast to the truly diffuse background. We will distinguish that the ALP originated emission from the X-ray diffuse background (XDB) with this principal.

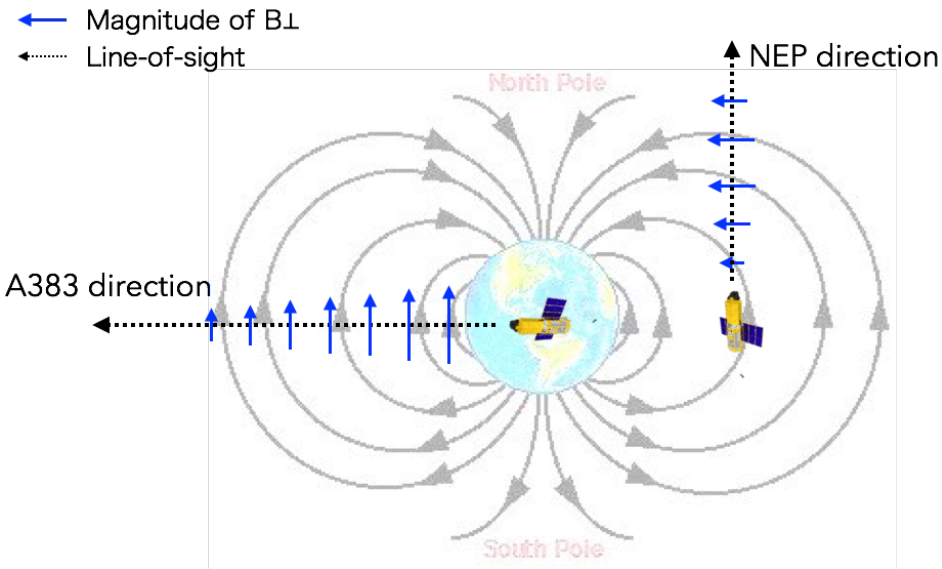

Figure 4.8 Examples of the relative position and observation direction of *Suzaku* satellite to the Earth magnetosphere.

4.4 Target selection for ALPs search

In order to search for X-ray continuous emission from ALPs, we selected four observational targets from *Suzaku*/XIS data of XDB. The XDB emission is included in all of the observational data. First, we filtered out the archival data of *Suzaku*/XIS from 2005 to 2015 in accordance with the condition proposed by Sekiya et al. (2016) as shown below:

1. No bright sources (i.e., the original observational purpose was a study of blank sky fields) or maskable faint compact sources are in the XIS FoV;

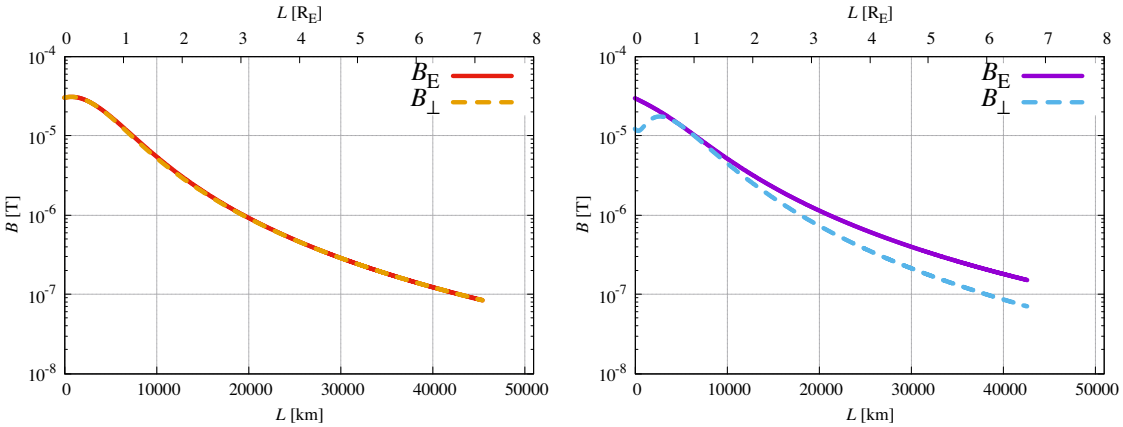

Figure 4.9 Transverse magnetic field along the line of sight of *Suzaku* satellite, calculated by IGRF model and actual satellite position. Left: The target of A383. Right: The target of NEP.

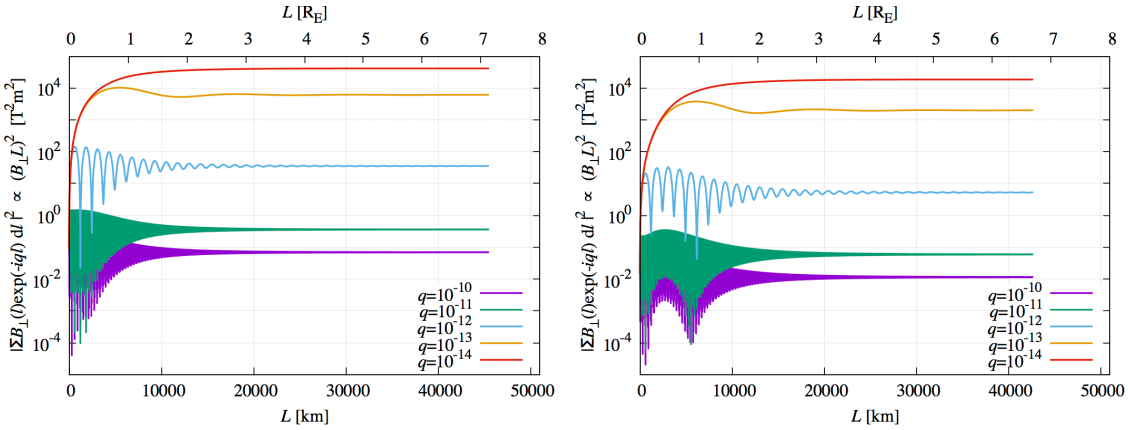

Figure 4.10 ALPs-photon conversion efficiency, $(B_\perp L)^2$.

2. Galactic latitudes of $|b| > 20°$ so as to avoid the X-ray emission peculiar to the Galactic disk (Masui et al., 2009);
3. Separate from the region occupied by the North Polar Spur and other local X-ray sources;
4. The XIS was operated in the normal clocking mode and the 3 × 3 or 5 × 5 editing mode;

One of the most uncertainty is the fluctuation of the cosmic X-ray background (CXB) in the energy bands above 2 keV. The cause of this fluctuation is the number variance of point sources within the XIS FoV. Following the same approach as in Hoshino et al. (2010), we can estimate that the intensity of the CXB in the XIS FoV fluctuates as $\sigma_{\rm CXB}/I_{\rm CXB} \propto \Omega^{-0.5} S_c^{0.25}$, where Ω is the effective solid angle in the FoV, and S_c is the energy flux of the faintest point source. We took a nominal value of $\Omega_{Suzaku} \sim 0.07$ deg^2 (70 % of FoV) and

$S_c \sim 1.0 \times 10^{-14}$erg s^{-1} cm^{-2} in XIS observation. Based on the *Ginga* experience with the value of $\sigma_{\rm CXB}/I_{\rm CXB} = 5$ %, $\Omega_{Ginga} = 1.2$ deg^2, and $S_{c,Ginga} = 6 \times 10^{-12}$erg s^{-1} cm^{-2} in Hayashida & Inoue (1989), $\sigma_{Suzaku}/I_{Suzaku}$ is 4 % or more. However, since there is little time-variation, the CXB fluctuation is regarded as almost "0" in the same direction. Secondly, in this thesis, we require the following additional condition:

5. Total exposure time is more than 200 ks.

As a result, the 8 *Suzaku*/XIS directions were selected as shown in Table 4.3. We selected a data set of the 4 directions (Lockman hole, MBM16, SEP, NEP), because the other directions contain radiation components except for XDB (e.g. outflow of AGN). APM 08279+5255 is a quasar whose observational aim is the X-rayed outflow (Saez & Chartas, 2011). Grupe et al. (2012) shows that MKN 335, Seyfert galaxy, has X-ray variability even on timescales of hours. ABELL 1689 (OFFSET) is an extended halo of the intracluster medium, and NGC 720 OFFSET is an interstellar medium of the elliptical galaxy, respectively (Kawaharada et al., 2010; Tawara et al., 2008). As presented in Table 4.3, there are several observations in 7 directions. The observations in the same direction are distinguished by a unique observation number called ObsID. After a standard data processing as necessary, we handled the all data sets. Their observational details were summarized in Appendix A.

Table 4.3 Long exposure observation of X-ray diffuse background with *Suzaku* satellite

Field name	Number of observations	Total exposure time [ks]
Lockman hole	11	542.5
MBM16	6	446.9
APM 08279+5255	3	321.7
MKN 335*	2	298.8
ABELL 1689 (OFFSET)	3	264.2
NGC 720 OFFSET	1	223.9
NEP	4	205.0
SEP	4	204.2

* ToO (Time of Opportunity) observation.

5 Search for X-ray emission from ALPs

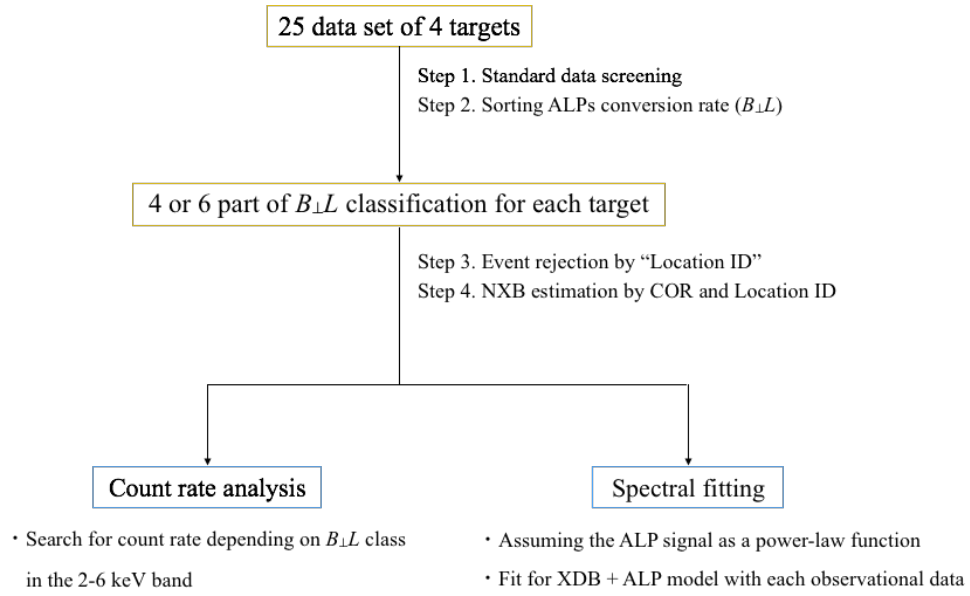

Figure 5.1 Process flow of data analysis in Chapter 5.

5.1 Standard data screening

In this thesis, we analyzed all *Suzaku* data utilizing the Ftools in HEAsoft version 6.16[*1] and XSPEC version 12.8.2.[*2] Errors shown in tables are 90% confidence level without notification. For all analysis, cleaned event files of the FI-CCDs (XIS0 and 3) and the BI-CCD (XIS1) by *Suzaku* standard pipeline products had been used to obtain enough photon statistics. In the low energy band (< 0.7 keV), time-varying emission due to Solar wind charge exchange (SWCX) exists as described in Section 3.3. Furthermore, since the effective area is small in a high energy band (> 7 keV for FI and > 5 keV for BI), the photons from the Non-X-ray background (NXB) dominated in this energy band during blank sky observations. Although the BI-CCD has high NXB rate and poor reproducibility in the whole energy band, we used the BI-CCD that has higher sensitivity to the X-ray diffuse background (XDB) components except the cosmic X-ray Background (CXB) than FI-CCDs in a narrow energy band of 0.7–5.0 keV. The photon counts from anomalous (hot and flickering) pixels

[*1] Software package to modify Flexible Image Transport System (FITS) data files; http://heasarc.nasa.gov/heasoft/

[*2] An X-Ray spectral fitting package;https://heasarc.gsfc.nasa.gov /xanadu/xspec/

were detected and rejected by the `cleansis`[*3]. As a part of the standard screening, we screened out the *Suzaku*/XIS event data to reduce the X-ray contamination to XDB spectra with the following conditions:

- Time filter: to exclude the duration when the *Suzaku* passes through the South Atlantic Anomaly (SAA) because high particle flux makes the instrument unusable.
- Elevation filter: to exclude duration when the elevation angle (`ELV`) between the target and the Earth's limb $< 5^\circ$ and when the elevation angle from the day Earth limb (`DYE_ELV`) $< 20^\circ$, to reduce the contamination of emission from the Earth's atmosphere.
- COR filter: to exclude the `COR2`[*4] > 8 GV/c to reduce charged particle background detailed in Section 5.3.

Furthermore, we removed resolved point sources contaminating the XDB emission, similar to Sekiya et al. (2016), according to the following procedure:

1. XIS images of the 0.5–7.0 keV range were extracted.
2. Point sources in the XIS FoV were detected and rejected by using a wavelet function of similar size to the point-spread function of the XRT-XIS using `wavdetect` from the *Chandra* Interactive Analysis of Observations, version 4.6.
3. Point sources whose flux were larger than 1.0×10^{-14}erg s^{-1} cm^{-2} in the 0.5–7.0 keV range were removed with circular regions centered at their positions. The radius of the circular regions $> 1'.5$ was determined such that these regions included > 90 % of the source photons.

Brunner et al. (2008) reported that the 409 point sources were detected and reached a sensitivity limit of 9×10^{-16} erg s^{-1} cm^{-2} in the 2.0–10.0 keV by the deepest survey in Lockman hole with the *XMM-Newton*. Accordingly, in the case of Lockman hole observation, we removed point souses as circular regions centered at their positions whose flux is more than 1.0×10^{-14} erg s^{-1} cm^{-2} in Brunner et al. (2008).

[*3] `cleansis` is one of Ftool detailed in Appendix C

[*4] The name of cut-off-rigidity in the calibration database of *Suzaku*.

5.2 Sorting by ALP-photon conversion rate

Figure 5.2 shows an example calculation of the time dependence of ALP-photon conversion in the case of "Lockman hole" (ObsID:109014010) data. From Equation (4.1), $P_{a\to\gamma}$ is proportional to $(B_\perp L)^2$. For ALP search, we calculated the location of *Suzaku* every 60 seconds and the geomagnetic conversion of ALPs detailed in Section 4.2. The variances of $B_\perp L$ value range from several dozen to a few hundred at a sky observation. The histogram of $(B_\perp L)^2$ distribution averaging over 60 seconds each at each observational direction are shown in Figure 5.3. The area of these histogram represents the exposure time. The observational time was divided into $4 \sim 6$ parts by $B_\perp L$ value, on condition that time intervals were almost equal for each target. Figure 5.4 shows an example of above binning of $B_\perp L$ value. We summarized the bin interval of each observational target in Table 5.1. In this thesis, we compared the X-ray spectra among each $B_\perp L$ bin to detect the ALP signature.

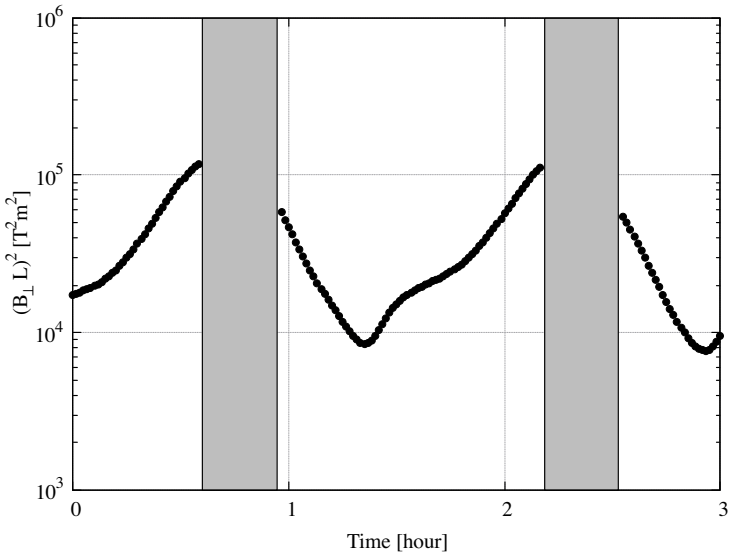

Figure 5.2 Time dependence of $B_\perp L$ in the Lockman hole observation. *closed circles*: the sky observation. *gray shading*: eclipse of the Earth i.e. the Earth exists between a target and *Suzaku*

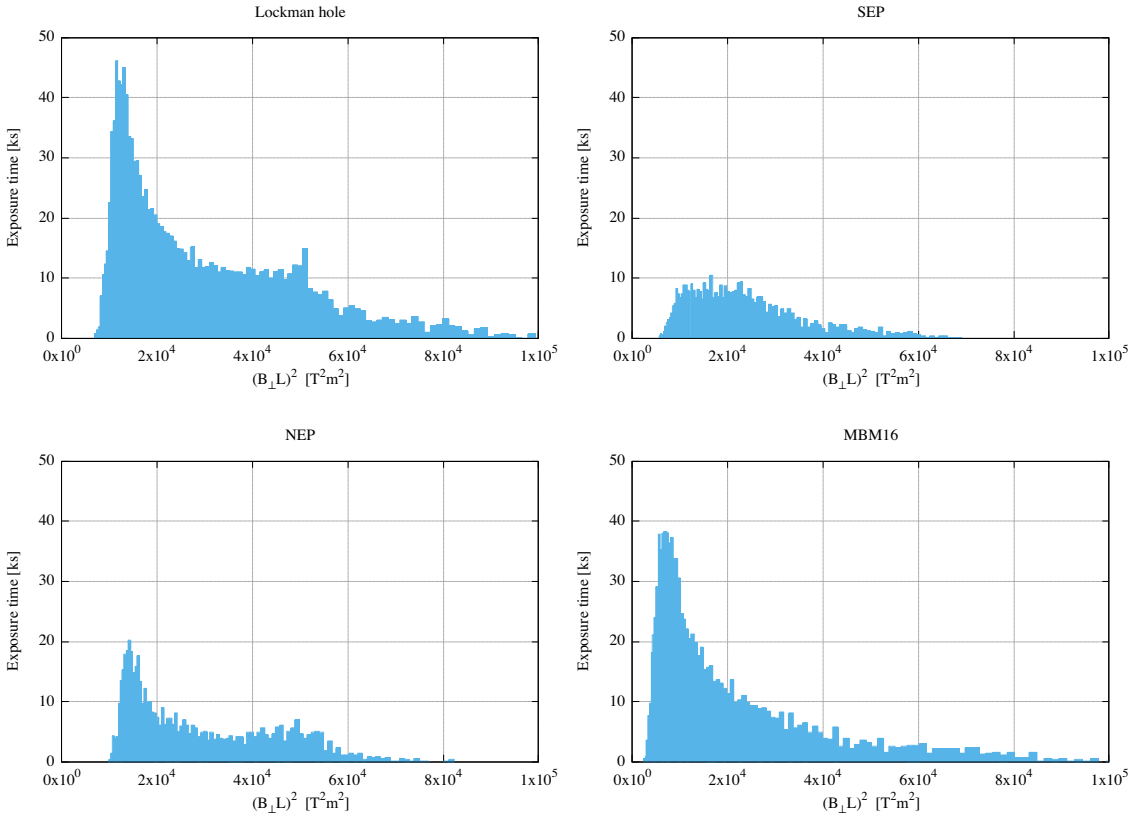

Figure 5.3 The histograms of $(B_\perp L)^2$ during observation of 4 direction.

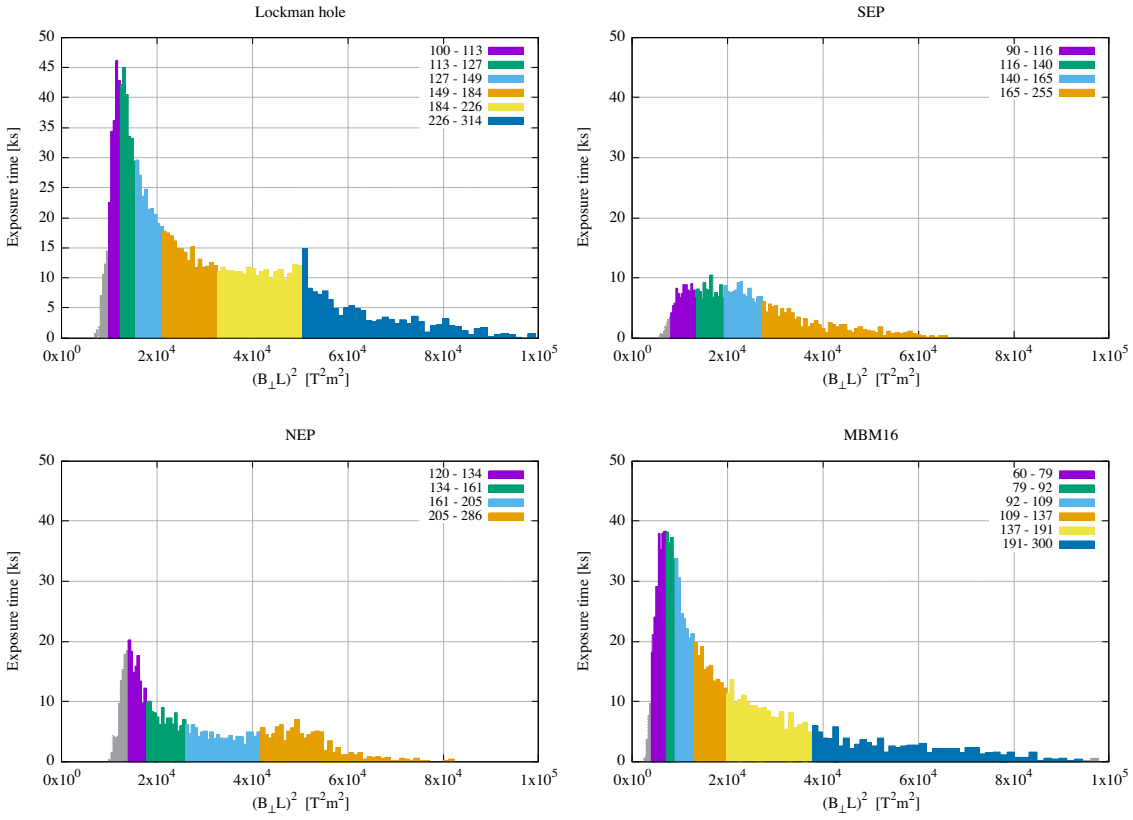

Figure 5.4 Examples of binning of exposure time, to obtain an almost equal number of photons in each class of $B_\perp L$

Table 5.1 Classification of $B_\perp L$ for each observation and corresponding exposure time.

Field Name	$B_\perp L$ interval [Tm]	$\langle (B_\perp L)^2 \rangle$ [T^2m^2]	Total exposure time [ks]
Lockman hole	100 – 113	11470	190.5
	113 – 127	14256	182.3
	127 – 149	18879	175.2
	149 – 184	27423	174.8
	184 – 226	42230	178.4
	226 – 314	64060	111.7
MBM16	60 – 79	5128	159.9
	79 – 92	7309	149.5
	92 – 109	9934	142.1
	109 – 137	14884	140.8
	137 – 191	25985	148.0
	191 – 300	53639	84.95
SEP	90 – 116	10837	93.98
	116 – 140	16384	88.75
	140 – 165	23104	86.39
	165 – 255	37404	95.21
NEP	120 – 134	15977	93.86
	134 – 161	21550	92.88
	161 – 205	33379	94.47
	205 – 286	51393	94.00

5.3 Standard estimation method of Non-X-ray Background with *Suzaku*

As shown in Section 4.1.3, the non-X-ray background (NXB) in XIS is understood by fluorescent lines and continuum emission by the cosmic rays. The Night Earth (NTE) database is used to estimate the NXB by a standard method shown below:

1. Stacking the NTE observation over during a few hundred days including the observational day (typically ±150 days).
2. Sorting these events by COR values.
3. Averaging these spectra for each COR range.
4. Summing the average spectra weighted by the exposure time ratio of each COR range.

The weighted NXB model spectrum, S_w, becomes

$$S_w = \frac{\sum_{i=1}^{n} T_i S_i}{\sum_{i=1}^{n} T_i} = \sum_{i=1}^{n} \frac{T_i}{T_{\rm total}} S_i, \tag{5.1}$$

where n is the number of COR ranges, T_i is exposure time of each COR range, $\sum_{i=1}^{n} T_i = T_{\rm total}$ is total exposure time of the on-source observation, and S_i is the averaged NTE spectrum for a COR range. In this method, Tawa et al. (2008) evaluated the NXB model in an exposure time of 50 ks can be reproduced with an accuracy of 3.4 % of the averaged count rate in 1–7 keV energy range.

There could be that the short-term variability of charged particles is due to solar activities like the coronal mass ejection, magnetic storms can cause short-term variability of NXB (e.g. Whittaker et al., 2013). We valuated the intrinsic variability of NXB data by following the Tawa et al. (2008) method as,

1. Stacking the NTE events in ± 150 days of the date of the target observation,
2. Dividing the stacking NTE event into 5 ks exposure bins,
3. Calculating count rate in 2.0–5.6 keV band during 5 ks time bin,
4. Calculating the standard deviation for 5 ks averaged NTE count rate and comparing with Poisson fluctuation,

for 4 observational directions for the ALP search. The obtained averaged NTE count rate and its standard deviation (1σ) are plotted as a function of time in Figure 5.5. These plots show that there is a long term decline of the NXB count rate. The trend is followed by the usage of ± 150 days data for the NTE accumulation. The typical number of counts for the accumulated NTE data is 10^5, thus the expected standard deviation by the Poisson statistics is roughly $0.2 \sim 0.4\%$. The calculated and expected 1σ deviation by Poisson statistics is summarized in Table 5.2. The calculated 1σ errors are always much larger than the expected

Poisson errors. It indicated that the NXB is not stable even in *Suzaku* and fluctuate more than simple Poisson statistics. Tawa et al. (2008) estimated the intrinsic variability for each XIS as 18.2±1.1%, 22.4±1.3%, 15.5±1.1% respectively for XIS0, 1, and 3 by *Suzaku* data obtained in 2005–2008 for a 50 ks exposure. The variability could be getting larger in time. In Section 5.4, we will try to investigate the fluctuations in long and short time range, and estimate the systematic errors of the NXB reproducibility.

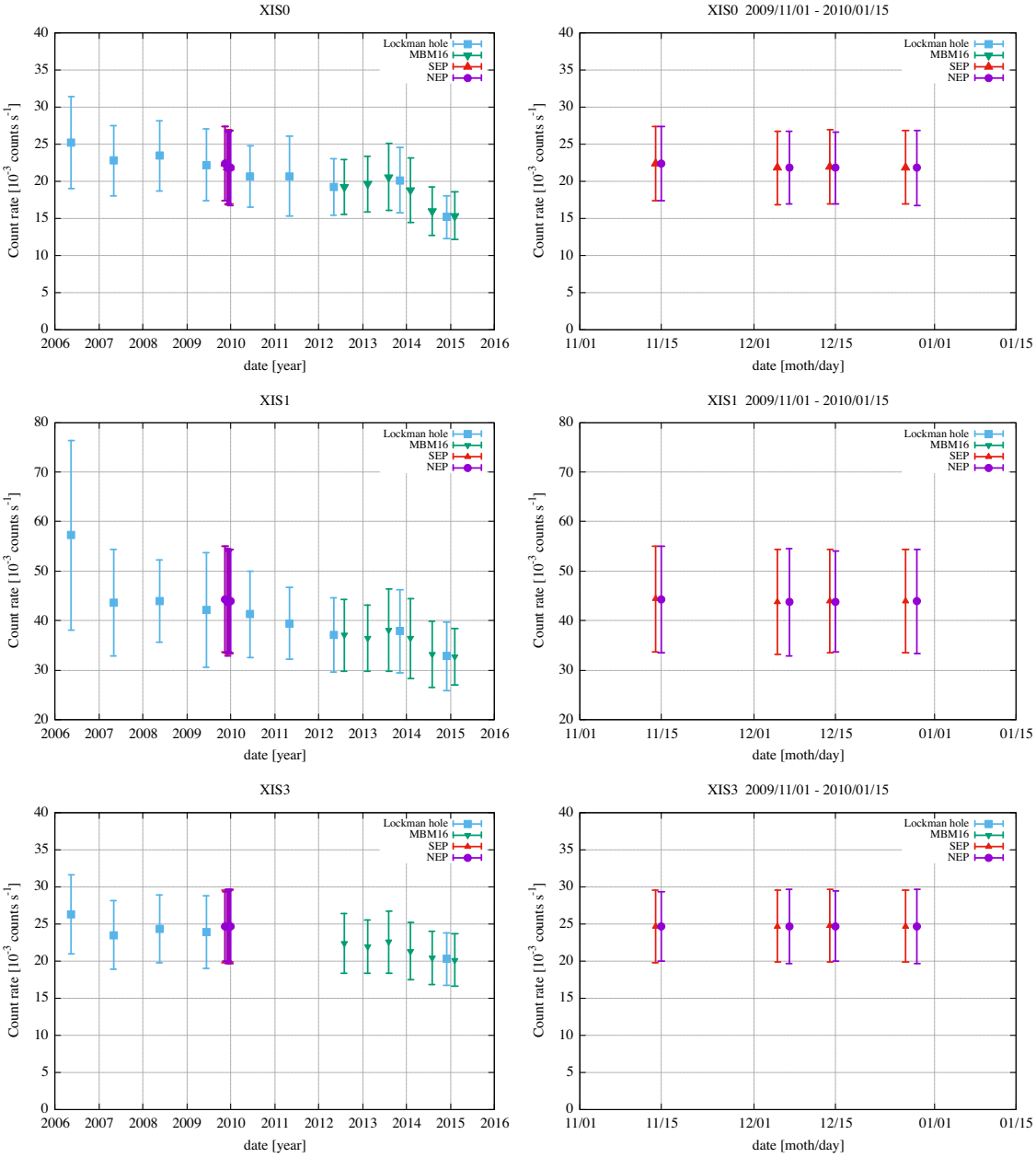

Figure 5.5 The averaged count rate and their standard deviation for XIS 0, 1 3 accumulated over 5 ks exposure during the night Earth observation as a function of time. The colors and marks indicate that the corresponding target observations use the same night Earth data as the NXB. The rate and deviation are compared with the evaluation of the intrinsic fluctuation by Tawa et al. (2008)

Table 5.2 Summary of statistics of the NXB data for each observation.

Field Name	Sensor	Averaged count rate* $[10^{-3}$ count $s^{-1}]$	Standard deviation$(1\sigma)^{\dagger}$ [%]	Poisson error$(1\sigma)^{\ddagger}$ [%]
Lockman hole	XIS0	20.9	29.7	0.27
	XIS1	41.0	46.6	0.19
	XIS3	23.7	22.3	0.38
MBM16	XIS0	18.7	24.0	0.34
	XIS1	36.2	23.1	0.24
	XIS3	21.7	19.3	0.31
SEP	XIS0	22.0	22.8	0.43
	XIS1	44.0	24.3	0.31
	XIS3	24.7	19.9	0.40
NEP	XIS0	21.9	23.1	0.43
	XIS1	43.9	24.7	0.31
	XIS3	24.7	20.2	0.41

* Obtained from the NTE event in the 2.0–5.6 keV band.

† Calculated standard deviation of 1σ normalized by average count rate.

‡ Estimated Poisson error of 1σ by total corrected photon number, normalized by average count rate.

5.4 Evaluation of the systematic errors in NXB estimation method

5.4.1 Investigation of fluctuation of NXB in short time range

Table 5.2 in previous section showed that the count rates of the NTE events fluctuates more than those expected from the Poisson statistics. NTE events are taken from the period where the FoV is covered by the night Earth. We thus use the events at 12–15 keV during the target observation as a real-time monitor of the NXB event. The X-ray reflection efficiency above Au L-edge decrease rapidly to be less than 1% (Serlemitsos et al., 2007), CCD detected events between 12 and 15 keV can be a good measure. The count rates of NTE events in 2.0–5.5 keV and 12–15 keV as a function of the `COR2` in 2006 are shown in Figure 5.6. The trend is the same, and the event rate in XIS1 in 12–15 keV is 3 times larger than that in 2–5 keV. In Tawa et al. (2008), the intrinsic fluctuation is evaluated as $\sqrt{\sigma^2_{\rm calc} - \sigma^2_{\rm Poisson}}$. We update this method as follows;

$$P_{\rm NXB}\left(X = k\right) = \frac{\lambda\left(k,\sigma\right)^k e^{-\lambda(k,\sigma)}}{k!}, \quad \lambda\left(k,\sigma\right) = \frac{1}{\sqrt{2\pi\sigma^2}} \exp\left(-\frac{\left(k-\mu\right)^2}{2\sigma^2}\right), \tag{5.2}$$

where k is an observation frequency per interval, $\lambda\left(k,\sigma\right)$ is an average number of events per interval, σ is an estimated systematic error by the variation of $\lambda\left(k,\sigma\right)$, and μ is an average of observed NXB events. It assumes that the variations of the mean value of the count rates follows a Gaussian distribution, and the detected count follows a Poisson distribution. Thus the observed count rate is expressed by a convolution of these functions. We use the Pearson's chi-squared test (Pearson, 1900) to set a quantitative upper limit for the short term variability. A sample of these test is shown in Figure 5.7.

1. Counting the number of events in 12–15 keV during the 60 s for each `COR2` range
2. Calculating an average of the count every 60 seconds, μ, from the light curves (green histogram in Figure 5.7)
3. Assuming a certain value σ, and simulating a $P_{\rm NXB}$ by Monte-Carlo method as shown in Equation (5.2) (lines in Figure 5.7)
4. Comparing the observed and simulated histograms by Pearson's chi-squared test and obtaining 95% upper limit for σ

We calculated the upper limits of σ/μ for each observation and each COR bin. The 95% upper limits of σ/μ of the short-term fluctuation of the NXB for each observation, is summarized in Table 5.3, where the upper limits for different upper CORs are averaged with a weighting factor proportional to the exposure time.

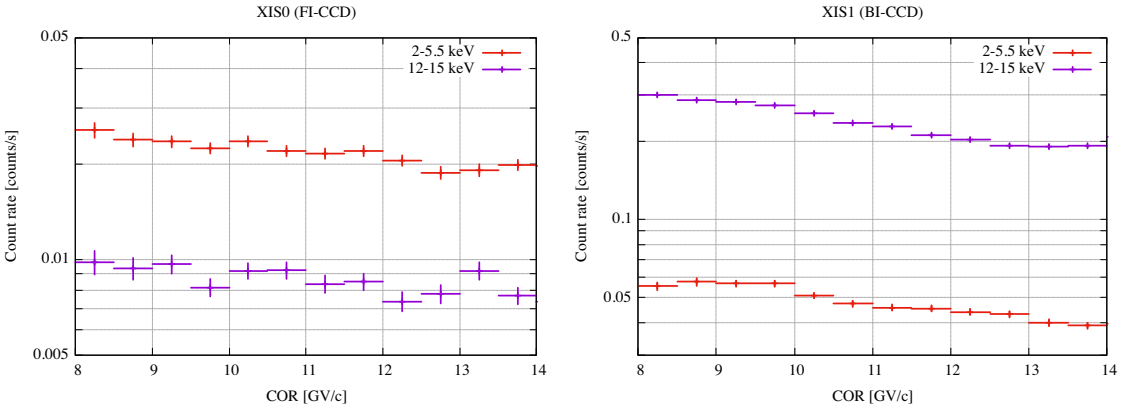

Figure 5.6 The count rates in 2–5.5 keV and 12–15 keV as a function of the `COR2` estimated from the NTE event in Lockman hole observation. *Left*: XIS0(FI-CCD). *Right*: XIS1(BI-CCD). Note that the errors are calculated by Poisson statistics, i.e., square-root of corrected number of photons divided by exposure time.

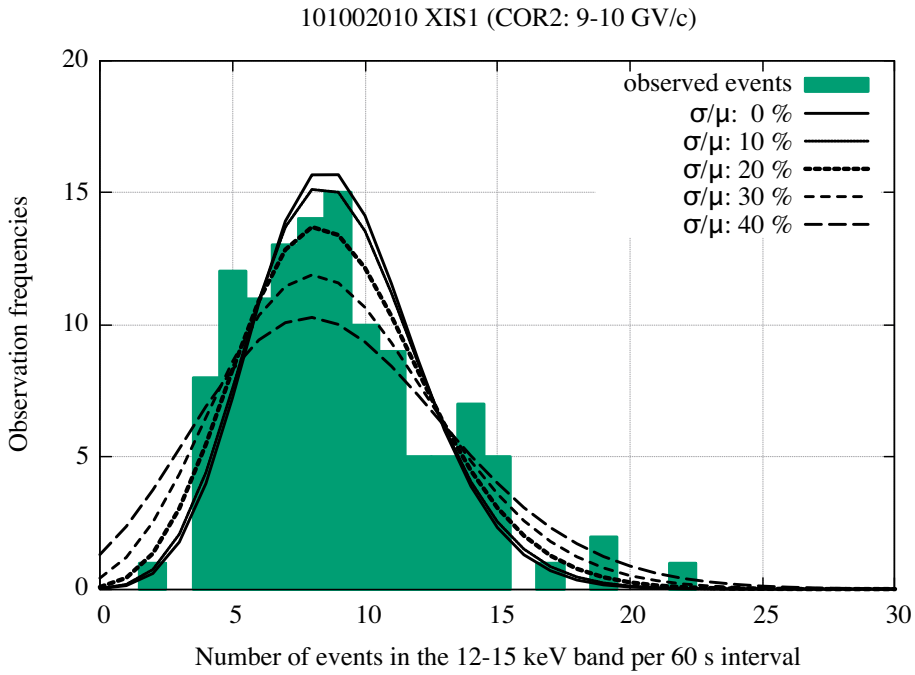

Figure 5.7 A sample of histogram for observed events in 12–15 keV of XIS1 in `COR2` range of 9 to 10 GV/c and the probability distribution of each σ/μ estimated from Equation (5.2).

Table 5.3 The summary of the 95 % upper limits the short-term fluctuation of the NXB.

Field name	ObsID	Estimated systematic error of σ/μ [%]
Lockman hole	101002010	28
	102018010	27
	103009010	28
	104002010	34
	105003010	29
	106001010	37
	107001010	39
	108001010	28
	109014010	26
MBM16	507076010	38
	507076020	36
	508078010	37
	508078020	38
	509073010	34
	509073020	30
SEP	504069010	30
	504071010	33
	504073010	31
	504075010	32
NEP	504070010	37
	504072010	27
	504074010	31
	504076010	22

5.4.2 NXB trend in long time range and introducing Location ID cut

As shown in Figure 5.5, the NTE event rate is declining as a function of time. Figure 5.8 left shows the count rate of NXB at `COR2` of 12–13.5 GV/c during the night Earth observation for 100 days. The main reason of the trend is considered to be the decline of the orbital attitude of *Suzaku*, as shown in the right panel of Figure 5.5. The Solar cycle modulation is not clear.

In averaging night earth events for 100 days or less, sufficient statistics cannot be obtained to reproduce the NXB at the time of observation. On the other hand, when averaging for more than one year, the reproducibility of NXB will be affected by long-term fluctuation as shown in Figure 5.8 right. Hence, we decided to adopt the 300 day average of the NTE event, i.e., ± 150 days of the date of the observation, the same as in the standard NXB estimation.

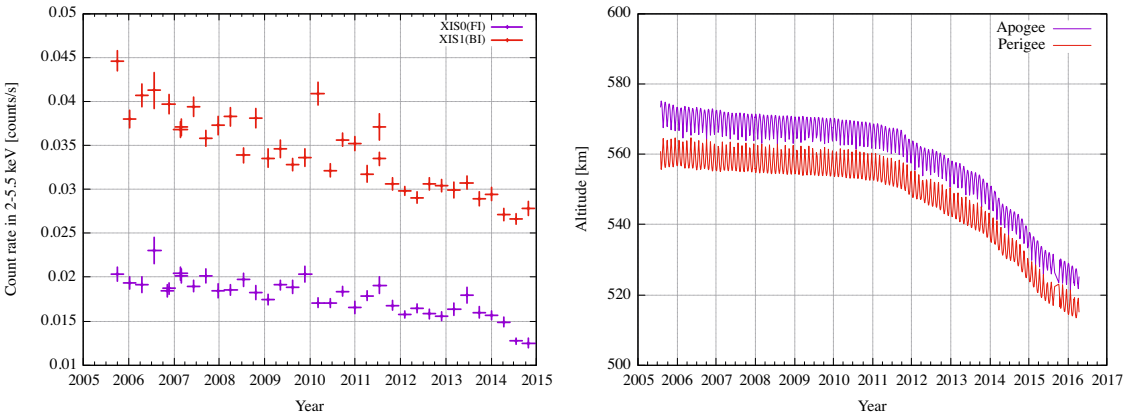

Figure 5.8 Left: The count rate when `COR2` values are between 12 GV/c and 13.5 GV/c, Right: The altitude of *Suzaku* orbit.

The nominal `COR2` used in the *Suzaku* analysis is shown in Figure 5.9, which was calculated in 2005. Due to the change of the magnetic field and satellite orbit, the COR is changing. The map in Figure 5.10 is a COR map prepared for Astro-H (Takahashi et al., 2016), based on the magnetic field data at 2016/1/1. The two maps are slightly different, as shown in Figure 5.11. It indicates that the COR sort method has a potential risk when the `COR2` table in the *Suzaku* standard data analysis package is not updated.

The $B_{\perp}L$ value is determined by the observational direction and the location of the satellite in relation to Earth, and the NXB is estimated by COR which is also allocate on the satellite position. However, if there is a location where the non-X-ray background rate is different from other places with the same COR value such as the SAA, it cannot be classified whether the origin is a signal from the Earth location or ALPs by standard estimation of NXB. Hence,

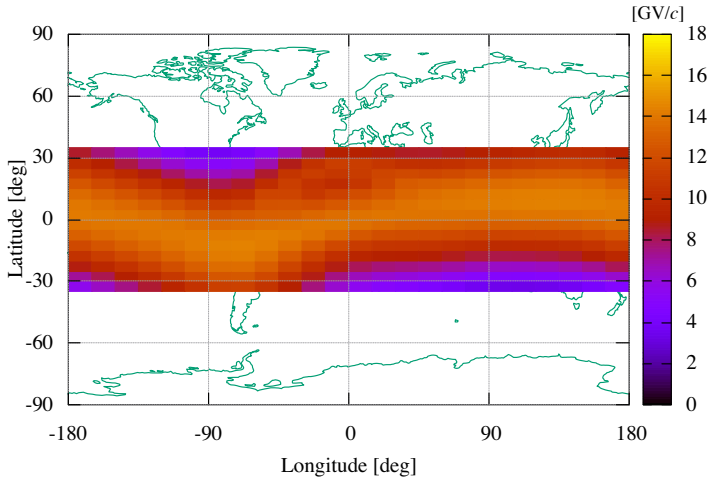

Figure 5.9 The cut-off rigidity map calculated Corrected Geomagnetic Coordinates (CGM) model T96 (http://www.ngdc.noaa.gov/IAGA/vmod/igrf.html) at an altitude of 570 km on 2006/04/21.

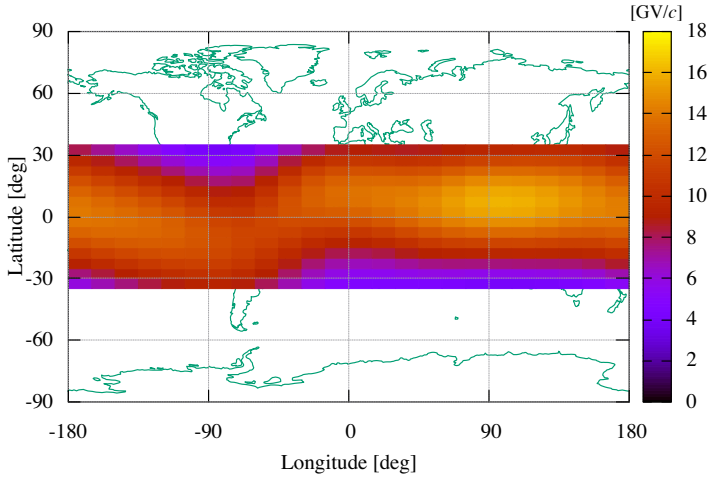

Figure 5.10 The cut-off rigidity map calculated for the date 2016.0 from the IGRF-12 at an altitude of 570 km on 2016/01/01.

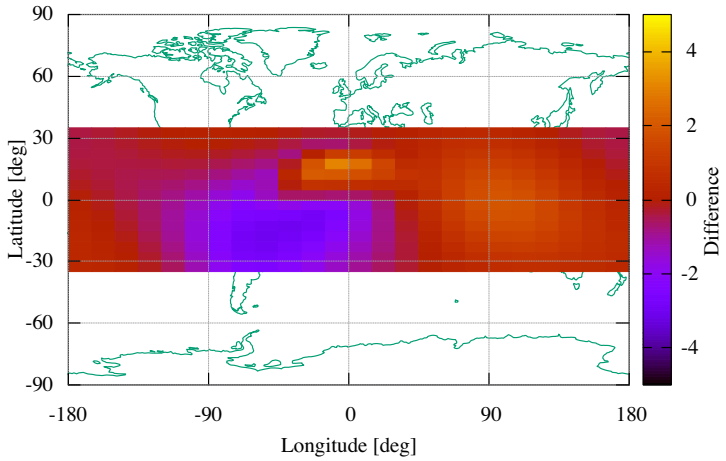

Figure 5.11 The difference of cut-off rigidity to subtract Figure 5.9 from Figure 5.10.

we defined the location ID (LOC_ID) in a geographic coordinate system as shown in Figure 5.12. The longitude is made 18 division from -180° to 180°, and the latitude is made 13 division from -32.5° to 32.5°. The number as LOC_ID is assigned to the grid from 1 to 234. Incidentally, "LOC_ID=0" shows the all outside this area.

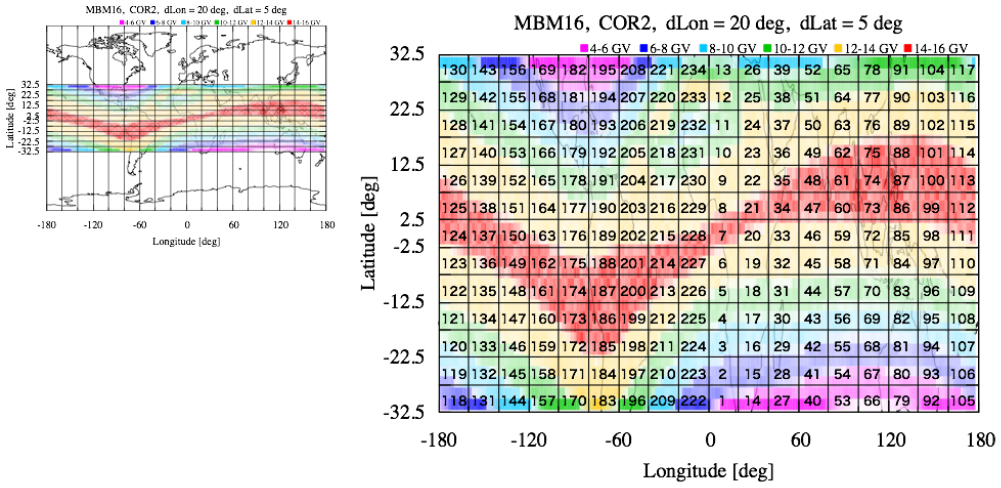

Figure 5.12 Definition of location ID and calculated COR2 values.

We investigated whether the background rate at LOC_IDs of the same COR2 is consistent or not. If there is some anomaly, we will discard events at such LOC_IDs. Figure 5.13 shows an example of count rate at LOC_ID from 120 to 180 from all NTE events (2007∼2015) with averaged COR2 values. As shown in Figure 5.13, in most cases of LOC_ID, the count

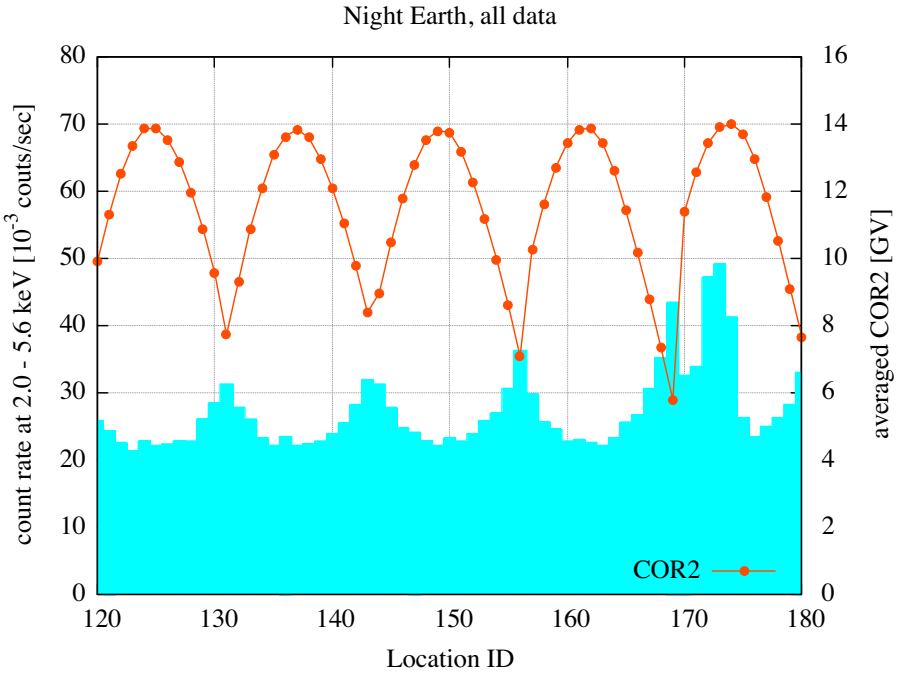

Figure 5.13 Count rate of non X-ray background during the night Earth observation as a function of Location ID. Averaged COR at that location ID is also plotted with the right axis.

rate is inversely correlated with the `COR2` value (e.g. `LOC_ID`=120–160). In the following (`LOC_ID`=170–175 in Figure 5.13), though the `COR2` value is large in local, the count rate is larger. These high NXB anomalies cannot be removed by standard data reduction. We sorted out the `COR2` and `LOC_ID` using the following method:

1. Stacking the NTE event ± 150 days of the date of the observation
2. Averaging the count rate for each `LOC_ID`
3. Sorting the `LOC_ID` by `COR2` values into 4 classes whose range are 8–10, 10–12, 12–13.5 and 13.5–20 GV/c
4. In each COR class, the average and standard deviation of the count rate is calculated regardless of a `LOC_ID`.
5. If the count rate at that `LOC_ID` deviates from the distribution more than 3σ level, the data of a `LOC_ID` is discarded.
6. Repeat 4-5 until all count rate distribution is within $\pm 3\sigma$ range.

An example of the above selection as shown in Figure 5.14 indicates that the method can eliminate the `LOC_ID` of high count rates in each COR class. The `LOC_ID` discarded by observational data has been decided by this condition detailed in Appendix B.

In addition to the standard NXB data estimation by ftools "`xisnxbgen`" based on Tawa

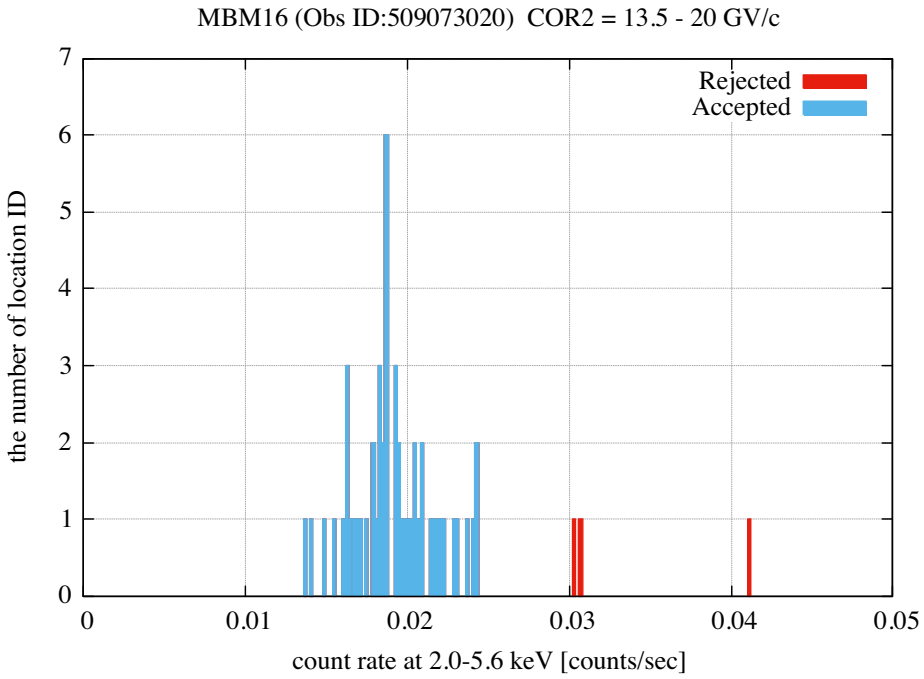

Figure 5.14 The histogram of count rate in the COR2 range from 13.5 GV/c to 20 GV/c as a selection example.

et al. (2008), the NXB spectra were estimated by the sorting parameter of LOC_ID. In other words, we replaced the location ID with the COR value shown in Section 5.3. In this thesis, the NXB sorted by location ID is represented with the subscript LOC_ID.

5.5 Count rate dependence on $(B_\perp L)^2$ in the 2–6 keV band

We investigated the count rate dependence on the ALP-photon conversion rate, which is proportional to $(B_\perp L)^2$ without any assumptions of a spectral shape. Figure 5.15 shows the count rates in the 2–6 keV band as a function of $(B_\perp L)^2$ before and after the NXB subtraction. The count rates are the sum of XIS0, XIS1, and XIS3 in each target observation. The raw count rates are shown by the open marks, and NXB subtracted ones are shown by the filled marks. The NXB was estimated by the standard method as described in Section 5.3, which uses night Earth database sorted by `COR2` (Tawa et al., 2008). The count rate differs by the observed target, which might reflect the difference in the surface brightness of the X-ray diffuse background. The $(B_\perp L)^2$ dependence is a downward trend except for the Lockman hole, contrary to the expectation of emission from ALPs which is proportional to $(B_\perp L)^2$. These trends are hard to originate from the XDB emission or possible ALP

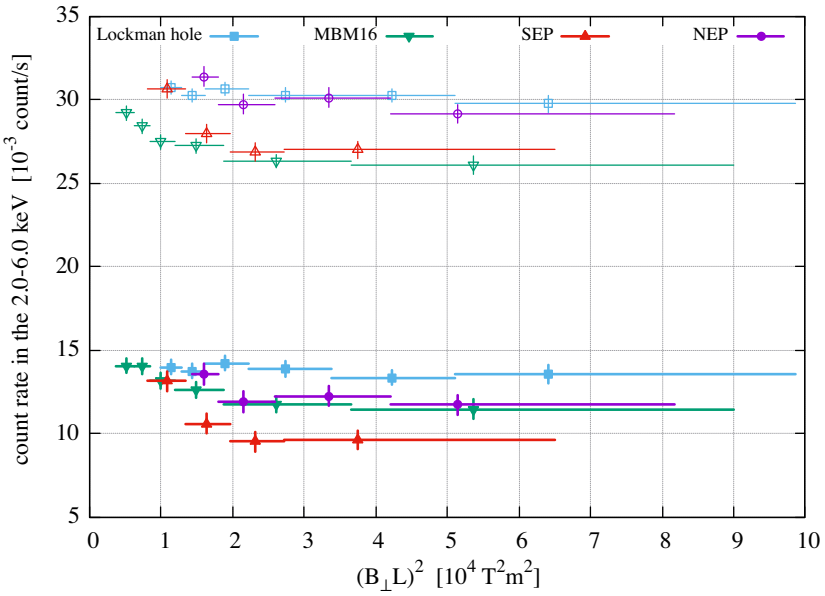

Figure 5.15 Measured count rate as a function of $(B_\perp L)^2$ in four observational directions. Error bar of the count rate indicates 1σ statistical error ranges assuming the Poisson distribution of observed counts. Shapes of marks shows observation directions, as a rectangle:Lockman hole, downward triangle: MBM16, upward triangle: SEP, circle: NEP, *Open mark*: raw count rates, and *Closed mark*: count rate after the subtraction of estimated NXB.

emission. Thus, we suspect that it comes from the NXB which depends on $(B_\perp L)^2$. Figure 5.16 shows the count rates of NXB estimated by the *Suzaku* standard method (Tawa et al., 2008) and used in the subtraction in Figure 5.15. They were produced by `COR2` sorted

calibration database, and reflect COR2 dependence, however did not reproduce the $(B_\perp L)^2$ dependence as shown in Figure 5.15. We then applied LOC_ID data selection as described in

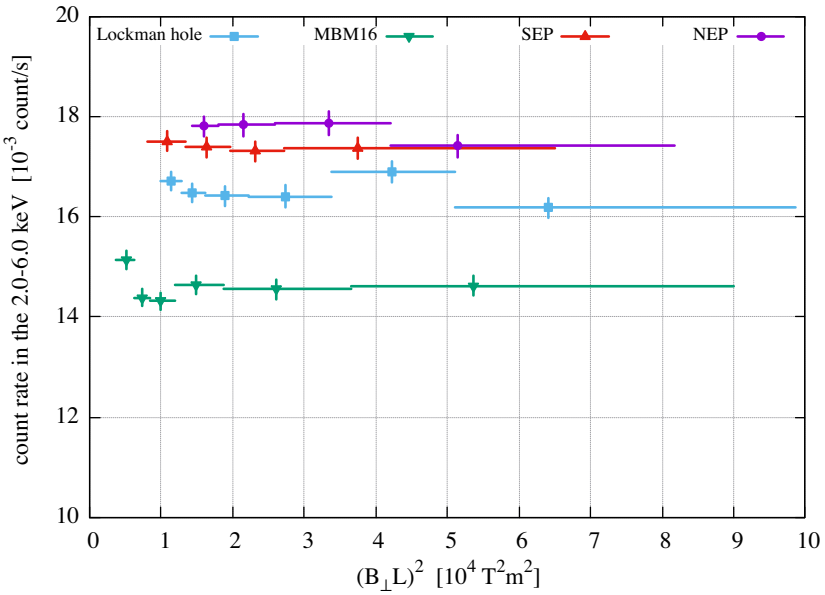

Figure 5.16 Estimated NXB count rate by *Suzaku* standard method described in Section 5.4 (Tawa et al., 2008), and used for subtraction in Figure 5.15. Marks shows observational direction as same as in Figure 5.15. No apparent $(B_\perp L)^2$ dependence is shown.

Section 5.4.2, and reproduce the count rates from the sky and subtract the estimated NXB as shown in Figure 5.17. The count rate at the low $(B_\perp L)^2$ part became flatter than Figure 5.15. However, the whole trend in each observation shows only little changes.

As described in Section 5.3 and 5.4, the NXB has the uncertainty of NXB reproducibility by *Suzaku* standard method (Tawa et al., 2008), and the systematic errors caused by long-term and short-term trend are were evaluated. Considering these systematic uncertainties, the errors of estimated NXB need to be larger than those estimated only by the Poisson statistics with 10–20 % of the best-estimated medium value. If we added systematic errors of 10%, the $(B_\perp L)^2$ dependence of the count rate shown in Figure 5.17 is wiped out. However, it might be too much, because the count rates for each observation at higher $(B_\perp L)^2$, such as $(B_\perp L)^2 > 2 \times 10^4$ Tm indicates that the subtraction of the NXB works.

Then we fitted the count rate vs. $(B_\perp L)^2$ by a linear function and evaluate the component which is proportional to $(B_\perp L)^2$ at a certain region of $(B_\perp L)^2$:

$$\mathrm{CR} = C_{\mathrm{const}} + D_{\mathrm{slope}} \cdot (B_\perp L)^2 \quad \text{at} \quad (B_\perp L)^2 > (B_\perp L)^2_0, \tag{5.3}$$

where CR is the count rate in the 2.0–6.0 keV as shown in Figure 5.17, C_{const} is a constant which represents CXB component, D_{slope} is a slope which represents ALP component, and

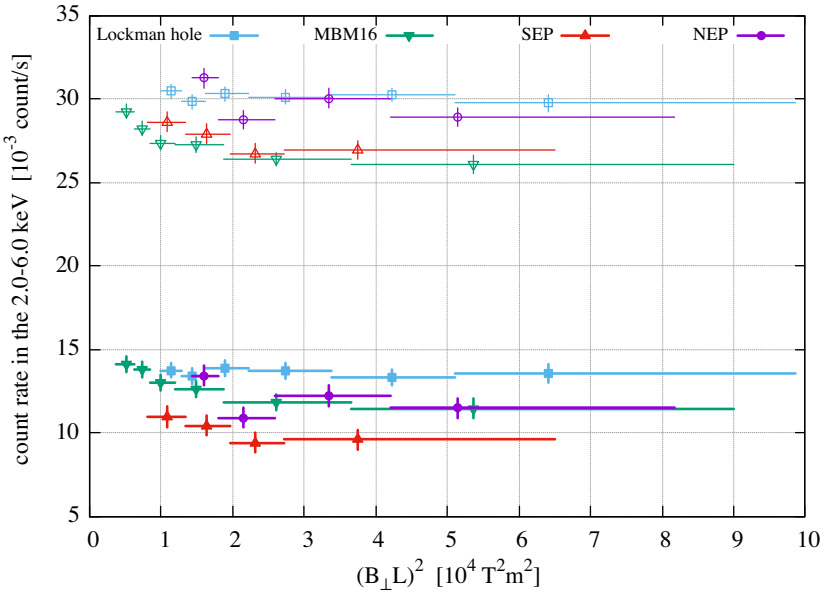

Figure 5.17 Measured count rate as a function of $(B_\perp L)^2$ in 4 observational directions with the data selected by `LOC_ID`. Error bar of the count rate indicates 1σ statistical error ranges assuming the Poisson distribution of observed counts. Marks show observational direction as same as in Figure 5.15.

$(B_\perp L)_0^2$ is a lower limit of fitting range as shown in Figure 5.18. The results of fitting are

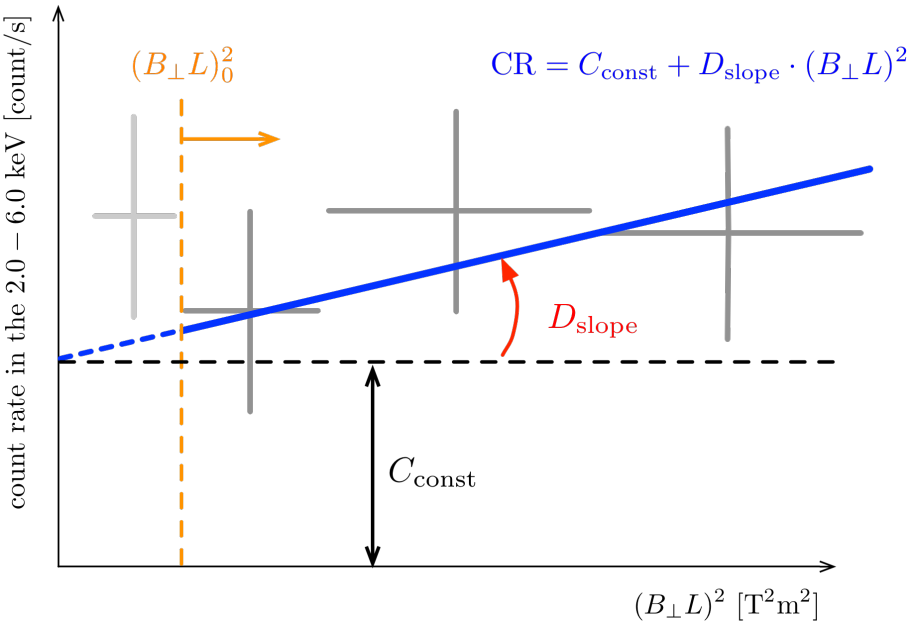

Figure 5.18 A schematic drawing of fitting the count rate by a linear function in Equation (5.3).

summarized in Figure 5.19 and Table 5.4 with 1σ statistical errors. Table 5.4 shows that

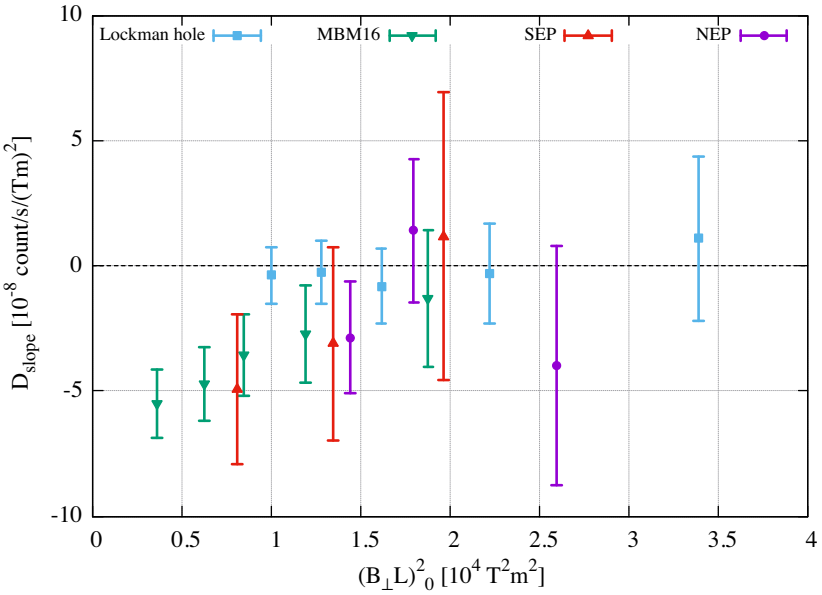

Figure 5.19 The slopes of the linear function as a function of lower bounds of the fitting range $(B_\perp L)_0^2$. These plots are estimated from Figure 5.17 and represent the count rate of ALP component. Error bar indicates 1σ statistical error ranges.

Table 5.4 The summary of constant and linear functions fitting by using the data in Figure 5.17. Errors are at 1σ confidence level from error propagation.

Field Name	$C_{\rm const}{}^*$ at $B_\perp L = 0$	$D_{\rm slope}{}^\dagger$
Lockman hole	13.7 ± 0.7	-3.2 ± 19.9
MBM16	12.2 ± 1.1	-13.1 ± 27.2
SEP	9.1 ± 1.8	11.9 ± 57.7
NEP	11.0 ± 1.1	14.1 ± 28.5

All errors indicate 1σ confidence level.

* Constant component which represents XDB in unit of 10^{-3} counts s^{-1}

† ALP component which is propotional to $(B_\perp L)^2$ in unit of 10^{-9} counts s^{-1} T^{-2} m^{-2} or 0.01×10^{-3} counts s^{-1} $\left(10^4\ \mathrm{T}^2\mathrm{m}^2\right)^{-1}$

the slopes of the linear function which represents the count rate of ALP component are not significantly positive within 1σ. Except the Lockman hole direction, the lower $(B_\perp L)_0^2$ gives values which are negative with 1 σ errors. We regard that this negative trends are artifacts and adopt the upper limits obtained at higher $(B_\perp L)^2$ ranges. As shown in Figure 5.19, it gives a threshold value of 1.8×10^4 $\mathrm{T}^2\mathrm{m}^2$ defined by the NEP observation.

The reason for the $(B_\perp L)^2$ negative dependence for XIS count rate at lower $(B_\perp L)^2$ part is not clear. One hypothesis is that the magnetic field strength perpendicular to the sight line or the satellite position affects intensity, spectrum, and species of the particle background. To investigate this hypothesis, we check a count rate of other *Suzaku* instrument, Hard X-ray Detector (HXD, Takahashi et al., 2007) which uses Si PIN diodes detectors shielded by BGO (Bismuth Germanium Oxide) crystals. There is an house-keeping monitor data of PIN-UD (PIN upper discriminator), which is a count rate summed for 64 channel PIN at upper discriminator levels about 90 keV in X-ray energy or equivalent to proton energy above 100 MeV within BGO shield (Kokubun et al., 2007). Tawa et al. (2008) showed that the PIN-UD count rate shows a strong correlation with `COR2`, and is a good particle background indicator. In SEP observation with strong $(B_\perp L)^2$ dependence, we verified the PIN-UD count rate sorted by $(B_\perp L)^2$ as same as the XIS count shown in Figure 5.17. The PIN-UD rates in Figure 5.20 shows the same trend as those of XIS. It suggests that the apparent $(B_\perp L)^2$ dependence in XIS count rate comes from particle background. Reproducing XIS background using the HXD PIN data is, however, beyond the scope of this thesis, because the HXD background shows fast (See Figure 19 in Kokubun et al. (2007)) changes due to activation of heavy scintillators after SAA passages, and long-term accumulation of those radio-active components. Also, the background simulation by Murakami et al. (2006) shown in Section 4.1.3 does not assume inhomogeneous irradiation of cosmic rays.

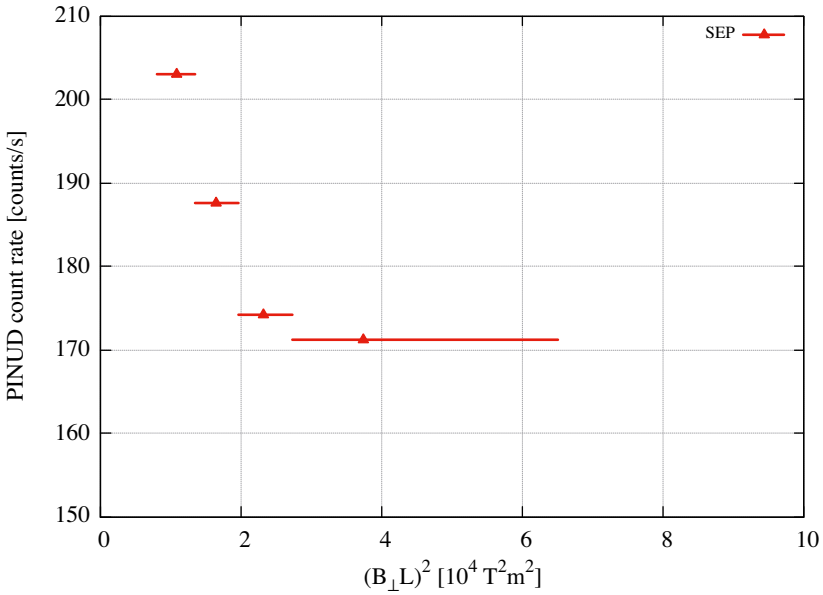

Figure 5.20 Example of PIN-UD count rate as a function of $(B_\perp L)^2$ in SEP observation.

The 3σ upper limits of count rates in proportion to $(B_\perp L)^2$ were calculated from the slopes with `COR2` sorted NXB in Table 5.4. These calculated limits by photon statistics

of $D_{\mathrm{slope},3\sigma} \times 10^4$ T^{2}m^2 are summarized in Table 5.5, as the count rate from the ALP components at $(B_\perp L)^2 = 10^4$ T^{2}m^2. These results in Section 5.4 does not assume the shape of spectrum for both ALP and CXB, thereby being difficult to examine the origin of ALP any further. It is also necessary to verify the results considering the systematic uncertainty obtained in Section 5.4. Therefore, in this section, we only indicate this value as a suggestion when not assuming a model of ALPs. As shown in Chapter 2, a decay of dark matter to ALPs at the cosmological distance will make a continuum emission with a power-law shape with a photon index of $-1/2$, which is different from the observed CXB spectrum. We will investigate the possible ALP component by the observed energy spectrum with fluctuated NXB model in next section.

Table 5.5 The statistical 3σ upper limits of ALPs originating component at $(B_\perp L)^2 = 10^4$ T^{2}m^2 calculated from $D_{\mathrm{slope},3\sigma} \times 10^4$ in Table 5.4, not including the assumption of spectrum shape.

Field Name	count rate*
Lockman hole	0.57
MBM16	1.1
SEP	2.0
NEP	1.0

* In unit of 10^{-3} counts s^{-1} in 2–6 keV by XIS0 + XIS1 + XIS3 at 10^4 T^2 m^2.

5.6 Search for continuum emission depending on ALP conversion efficiency

5.6.1 Spectral analysis with XDB model

Here we analyzed the energy spectrum of each observation, with a typical X-ray background model described in Chapter 3. We describe details of spectral fitting method and results of Lockman hole observations in this section, and figures of MBM16, SEP and NEP observations are presented in Appendix D. In the case of Lockman hole observation, we performed simultaneous fits for 23 datasets observed nine times per 10 years with 3 XISs. When the datasets are classified in $(B_\perp L)^2$ value, the number of dataset is 138. Those are fitted simultaneously by the same physical model to express the XDB.

In preparation for spectral analysis, in addition to the 138 energy spectra, we calculated the XIS energy redistribution matrix by the standard method. A matrix which describes the energy redistribution probability by the detector is called a "Redistribution Matrix File (RMF)". The mirror effective area is shown by a diagonal matrix called "Ancillary Response File (ARF)". They are calculated for each observation period with `xisrmfgen` and `xissimarfgen` (Ishisaki et al., 2007) ftools[*5], respectively. By the definition in Equation (1) in Ishisaki et al. (2007), the product matrix $\mathcal{R}(E_i, PI_j)$ of RMF×ARF gives the complete energy redistribution possibility times the effective area, which means X-ray irradiation with an energy spectrum of $S(E_i)$ is detected at at the Pulse Invariant (PI) as $M(PI_j) = \sum_i \mathcal{R}(E_i, PI_j)\, S(E_i)$. We generated the NXB spectra with `xisnxbgen` ftool[*6] by the improved `LOC_ID` methods described in Section 5.3 and 5.4. Thus, we performed spectral analysis for the four targets with energy spectra, RMSs, ARFs, and NXB spectra.

In the spectral analysis, some photons in each spectral bin become small because the data is classified in $B_\perp L$. The XDB model includes the narrow band emission, and large binning will lose the characteristics. As the goodness of fit the χ^2 statistics are often used, and sometimes C-statistics are used, which assumes that the count in each bin is Poisson distribution. In χ^2 and C-statistics, the likelihoods of data given models are Gaussian distribution (Lampton et al., 1976) and Poisson distribution (Cash, 1979), respectively. The process flow of our search is described below.

1. XDB model fit for summed spectrum of all $(B_\perp L)^2$ class evaluated by χ^2/dof
2. XDB model fit for summed spectrum of all $(B_\perp L)^2$ class evaluated by C/dof
3. XDB model simultaneous fit of $(B_\perp L)^2$ sorted spectra evaluated by C/dof

We fitted the energy spectra for the XDB emission model: (i) SWCX and LHB + (ii)

[*5] Ftools `xisrmfgen` and `xissimarfgen` detailed in Appendix C
[*6] Ftool `xisnxbgen` detailed in Appendix C

MWH + (iii) CXB + (iv) HTC, detailed in Section 3.3. For the optically-thin thermal CIE emission model, the *apec* model[*7] was applied to estimate the SWCX and LHB blend, MWH and HTC. The solar abundance table of *apec* model was given by Anders & Grevesse (1989), and the red-shift was set to zero. The temperature of *apec* in the SWCX and LHB blend was fixed to $kT = 0.1$ keV (Yoshitake et al., 2013). The CXB was represented by a *power-law* emission model[*8] which had photon index $\Gamma \sim 1.4$ (Kushino et al., 2002). In this analysis, this photon index was a free parameter to consider the fluctuation of CXB. Therefore, the following model was applied as the XDB model concerning Sekiya et al. (2016):

XDB model

$$apec_{\rm SWCX+LHB} + phabs(apec_{\rm MWH} + power\text{-}law_{\rm CXB} + apec_{\rm HTC})$$

where *phabs*[*9] was galactic absorption by the interstellar medium of the Milky Way. The galactic hydrogen column density ($n_{\rm H}$) was estimated from accurate observational data (LAB survey; Kalberla et al., 2005).

The fitting results were summarized in Table 5.6. The best-fit values of XDB parameters of each target are identical within 90% error. The parameters of XDB models in all four observations are consistent with the other works about XDB (e.g. Sekiya et al., 2016). The goodness of the fit, $\chi^2/{\rm dof} = 1.23$ (973), was, however, not acceptable. Sekiya et al. (2016) fitted the summed blank sky data of exposure time of $2.3 \sim 4.5$ Ms sorted by observation year with the same XDB model and obtained a goodness of fit χ^2 of 0.99(d.o.f 434) $\sim$ 1.44(d.o.f 434). They tuned the line intensity in the NXB by their data itself, which was able to be applied due to very long exposure dataset with enough photon statistics. They also added fudge factors to the standard response to deleting residuals in Crab nebula calibration data from a simple power-law fitting, although it is hard to distinguish whether these discrepancy comes from gain drift or change of detection frequency. Without these fine tuning, our fit obtained the same level of the goodness of fit, thus we do not pursue these approach and use the same DXB model. We checked the residuals of fit results by eye to confirm that there are no bunch of positive or negative peaks at a certain energy band, where no emission lines or change of detector efficiencies are expected.

A part of this discrepancy would come from the short fluctuation of the NXB, which is $\sim 30\%$ in Table 5.3. The ratio of the NXB and subtracted sky spectra is $1/2 \sim 1/6$. We evaluated the NXB fluctuation in the next subsection.

[*7] *apec* model in XSPEC detailed in Appendix C.
[*8] *power-law* model in XSPEC detailed in Appendix C.
[*9] *phabs* model in XSPEC detailed in Appendix C.

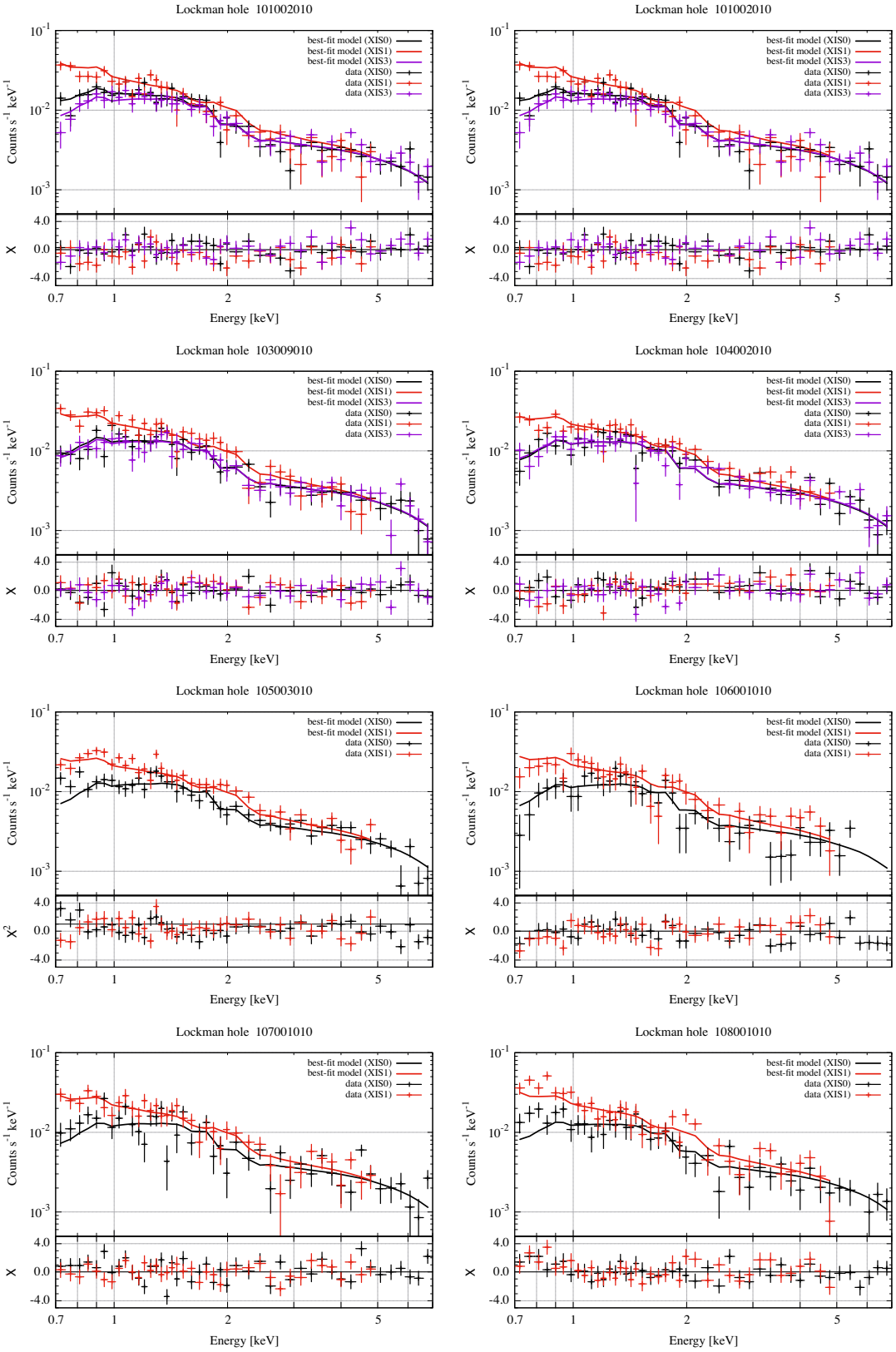

Figure 5.21 Spectral fit results for Lockman hole direction of each ObsID(101002010-108001010)

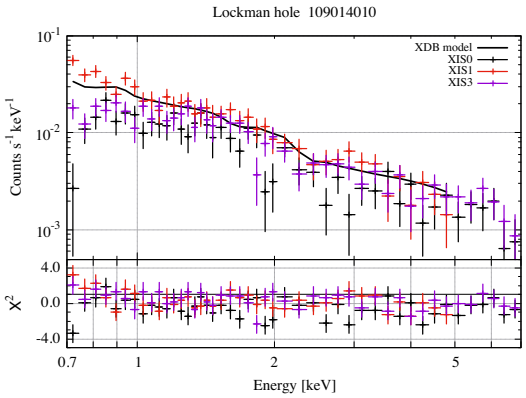

Figure 5.22 Same as Figure 5.21 but for other ObsID (109014010).

Table 5.6 Summary of parameters of the XDB model by spectral fitting in Lockman hole observation.

Parameter	Summed(χ^2)[¶]	Summed(C)[‖]	$(B_\perp L)^2$ sort(C)[‖††]
$n_{\rm H}$[*] (10^{20} cm^{-2})	0.58(fix)	0.58(fix)	0.58(fix)
Norm$_1$[†]	0(fix)	0(fix)	0(fix)
kT_2 (keV)	$0.14^{+0.03}_{-0.02}$	$0.17^{+0.01}_{-0.01}$	$0.17^{+0.01}_{-0.01}$
Norm$_2$[†]	$24.2^{+38.6}_{-12.1}$	$15.9^{+4.5}_{-2.0}$	$14.8^{+1.2}_{-0.9}$
$\Gamma_{\rm CXB}$[‡]	$1.33^{+0.02}_{-0.02}$	$1.33^{+0.01}_{-0.01}$	$1.33^{+0.01}_{-0.01}$
$S_{\rm CXB}$[§]	$7.6^{+0.1}_{-0.2}$	$7.8^{+0.1}_{-0.1}$	$7.8^{+0.1}_{-0.1}$
kT_3 (keV)	$0.64^{+0.07}_{-0.05}$	$0.61^{+0.07}_{-0.07}$	$0.62^{+0.14}_{-0.09}$
Norm$_3$[†]	$0.5^{+0.2}_{-0.2}$	$0.3^{+0.2}_{-0.1}$	$0.3^{+0.2}_{-0.1}$
χ^2 or C/dof(dof)	1.23(973)	1.27(973)	1.05(5878)

[*] The column densities of galactic absorption for the MWH, CXB and HTC component were fixed to the weighted average value estimated from Kalberla et al. (2005)

[†] The emission measure of CIE plasma integrated over the line-of-sight for SWCX+LHB, MWH and HTC (the normalization of *apec* model): $(1/4\pi)\int n_{\rm e} n_{\rm H} ds$ in unit of 10^{14} cm^{-5} sr^{-1}.

[‡] The photon index of the *power-law* model for the CXB.

[§] The surface brightness of the CXB (the normalization of *power-law* model): in unit of photons s^{-1} cm^{-2} sr^{-1} at 1 keV.

[¶] The goodness of the fit is χ^2/dof.

[‖] The goodness of the fit is C/dof.

[††] Simultaneous fit with $(B_\perp L)^2$ sorted spectra.

5.6.2 Spectral analysis with XDB and ALP model

Here we performed the spectral analysis with XDB and an additional ALP origin emission with a spectral shape of a power law and a photon index of $-1/2$ with its intensity proportional to $(B_\perp L)^2$. Thus, the ALP continuous emission was represented by a single *power-law* emission model with a photon index of $\Gamma = -1/2$ (where Γ is defined as a power law index in negative value to be dN/dE $\propto E^{-\Gamma}$) being in proportion to $(B_\perp L)^2$ values, *constant*×*power-law* (Asaka et al., 1998). The *constant* shows the ratio of averaged $(B_\perp L)^2$ values in Table 5.1. Eventually, we applied the following model as ALP for each spectral fitting:

ALP model

$$constant_{(B_\perp L)^2} \times power\text{-}law_{\rm ALPs}\ \left(\tfrac{dN}{dE} \propto E^{+1/2}\right).$$

If there is an ALP component, it will contribute the higher energy part, because of its positive slope of the energy spectrum. As the observed number of photons is fixed, the distribution of the NXB and ALP components at higher energy bands affects allowable volume of the ALP component. Thus, we will take into account the possible fluctuations of the NXB as studied in Section 5.4. In the previous subsection, we fit the all observations of the same targets with the same XDB model, with the fixed energy spectra subtracted by the estimated NXB. Here, we need to set the NXB component to be variable within the systematic errors obtained in Table 5.3, and to fit all 138 $(B_\perp L)^2$/ObsID/CCD dataset simultaneously with the same XDB + ALP model. It requires a new approach.

A standard approach to fit the X-ray data such from *Suzaku* is described as below. A model spectrum $M(E)$ including XDB and ALP is presumed from consideration for observed events $D(PI)$ and subtracted by the estimated and fixed NXB spectrum $N(PI)$, where PI is Pulse Invariant of *Suzaku*/XIS as shown in Figure 5.23. In other words, the model spectrum is estimated by comparison to the following equation:

$$D\left(PI_j\right) - N\left(PI_j\right) \longleftrightarrow \sum_i^n \mathcal{R}\left(E_i, PI_j\right) \cdot M\left(E_i\right) \cdot \Delta E_i, \tag{5.4}$$

where $\mathcal{R}(E, PI)$ is the instrumental response matrix (RMF×ARFs) calculated by the standard method shown in Section 5.6.1, and ΔE is the energy resolution of *Suzaku*/XIS. The statistical errors of $D(PI_j)$ and $N(PI_j)$ is expected from Poisson distribution, and used for the χ^2 or Cash statistics to obtain the fitting results.

In order to consider the fluctuations of the NXB, we defined NXB to be variable model as follows:

$$N\left(PI_j\right) = \sum_i^n \mathcal{R}'\left(E_i, PI_j\right) \cdot aM_N\left(E_i\right) \cdot \Delta E_i, \tag{5.5}$$

where $\mathcal{R}'\left(E_i, PI_j\right)$ is a diagonal matrix, and a is a NXB normalization parameter. Since

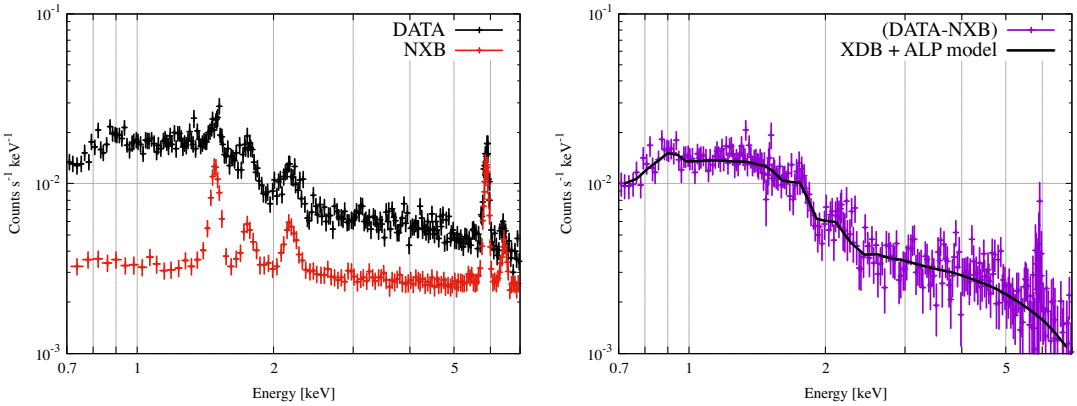

Figure 5.23 Examples of energy spectrum folded by detector response matrix, obtained toward Lockman hole. *Left*: observed spectrum and NXB spectrum. *Right*: the observed spectrum subtracted by the NXB spectrum and best-fit XDB + ALP model by method of Equation (5.4)

the fluctuation of NXB does not change the spectral shape, evaluating the systematic error independently for each bin results in an overvaluation. By comparing the interpolation model of NXB obtained by each observation in addition to the XDB + ALP model and the observed event, it is possible to evaluate the ALP flux in consideration of the NXB ambiguity as follows:

$$D\left(PI_j\right) \longleftrightarrow \sum_i^n \left\{\mathcal{R}\left(E_i, PI_j\right) \cdot M\left(E_i\right) \cdot \Delta E_i + \mathcal{R}'\left(E_i, PI_j\right) \cdot aM_N\left(E_i\right) \cdot \Delta E_i\right\}. \tag{5.6}$$

The fitted spectra obtained in this method is shown in Figure 5.24. This method can be applied because NXB is integrated with observations for 300 days and its statistical error is much smaller than systematic error.

We fitted all the dataset with different $(B_\perp L)$/ObsID/CCD simultaneously by the same XDB+ALP+NXB emission model parameters at $(B_\perp L)^2 > 1.8 \times 10^4$ T^{2}m^2 and with corresponding estimated NXB model spectra and normalization variable "$\{a\}$" for each dataset. The best-fit parameters from the fitting of the Lockman hole spectrum were summarized in Table 5.7. There are untabulated set of parameters of normalization, $\{a\}$, of NXB component, which are able to vary in each 138 dataset. The best-fit NXB normalization parameters of each four observations were summarized in Appendix D. The fluctuation of NXB normalization parameters within 90 % confidence level coincides with the range of short term fluctuation of NXB in Section 5.4. When the normalization of both NXB and ALP become larger, the intensities in the high energy band relative to the CXB become larger, although the observed number of photon is limited. Thus the fitted normalization parameter of the NXB and the ALP has a negative correlation. The value of $S_{\rm ALP}$ and the associated error show that the surface brightness from ALP is consistent with 0 within 90 % confidence level.

Figure 5.25 shows the confidence contour of the surface brightness of ALP and CXB in

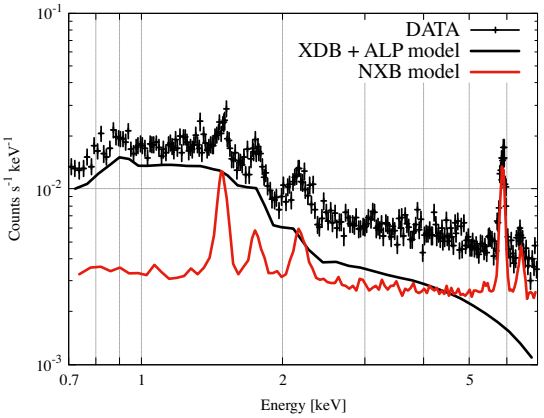

Figure 5.24 Example of observed energy spectrum folded by detector response matrix obtained toward Lockman hole, XDB + ALP model and NXB model by the method of Equation (5.6). The used observation data and nominal estimated NXB are as same as Figure 5.23

Table 5.7 Summary of parameters of the XDB + ALP + NXB model by spectral fitting in Lockman hole observation with high $(B_\perp L)^2$ class ($> 1.8 \times 10^4$ T^{2}m^2).

Parameter		Parameter	
$n_{\rm H}$* (10^{20} cm^{-2})	0.58(fix)	kT_3 (keV)	0.61‖
Norm$_1$†	0(fix)	Norm$_3$†	$0.5^{+0.4}_{-0.5}$¶
kT_2 (keV)	$0.14^{+0.08}_{-0.09}$	$\Gamma_{\rm ALP}$‡	-0.5(fix)
Norm$_2$†	28^{+622}_{-20}	$S_{\rm ALP}$**	$0.012^{+0.015}_{-0.016}$
$\Gamma_{\rm CXB}$‡	$1.42^{+0.13}_{-0.13}$	C/dof(dof)	1.11(2865)
$S_{\rm CXB}$§	$7.7^{+0.6}_{-0.6}$		

All errors indicate 90% confidence level.

* The column densities of galactic absorption for the MWH, CXB and HTC component were fixed to the weighted average value

† The emission measure of CIE plasma integrated over the line-of-sight for SWCX+LHB, MWH and HTC (the normalization of *apec* model): $(1/4\pi)\int n_{\rm e} n_{\rm H} ds$ in unit of 10^{14} cm^{-5} sr^{-1}.

‡ The photon index of the *power-law* model for the CXB and ALPs components.

§ The surface brightness of the CXB (the normalization of *power-law* model): in unit of photons s^{-1} cm^{-2} sr^{-1} at 1 keV.

** The surface brightness of the ALP (the normalization of *power-law* model): in unit of photons s^{-1} cm^{-2} sr^{-1} at 1 keV and 10^4 T^{2}m^2.

¶ Parameter pegged at fitting limit: 0.

‖ Since the normalization of *apec* allows 0 within the error range, the temperature is not determined.

Lockman hole observation. Since this contour is calculated by stepping all parameters one by one, and the surface brightness of CXB and ALP in the 2.0–6.0 keV band, $\mathrm{SB_{CXB}}$ and $\mathrm{SB_{ALP}}$, are calculated by

$$\mathrm{SB_{CXB}} = \int_2^6 S_{CXB} E^{-\Gamma_{CXB}} E \ \mathrm{dE} \tag{5.7}$$

and

$$\mathrm{SB_{ALP}} = \int_2^6 S_{ALP} E^{0.5} E \ \mathrm{dE} \tag{5.8}$$

respectively. The contour line is not the shape of the clean oval, because we do not take these surface brightness directly in the fitting function. The upper limit at 99 % *CL* of ALP flux evaluated by Figure 5.25 and Figure 5.26 of the all 4 observation fields and the expected count rate with an assumption of $\Gamma = -1/2$ power-law is summarized in Table 5.9. The largest upper limit at 99 % *CL* for ALP component with a photon index of $-1/2$ is obtained from the SEP observation where the surface brightness of the CXB is the lowest among these four, as to be 2.8×10^{-9} erg $\mathrm{s^{-1}}$ $\mathrm{cm^{-2}}$ $\mathrm{sr^{-1}}$ normalized at 10^4 $\mathrm{T^2 m^2}$.

Corresponding count rates were calculated to cross-check the results in Table 5.5. The count rates in the Table 5.9 were larger than ones in Table 5.5. Since we considered the systematic uncertainty of the reproducibility of the NXB even after assuming the shape of the spectrum, upper limits of count rate was mitigated in this subsection. It is possible that we investigate the physical properties of ALPs from this result, becase this spectral shape is estimated from the cosmic ALP density in Equation (2.9). We will examine these possibilities in detail in the Chapter 7.

Table 5.8 Summary of parameters of the XDB + ALP + NXB model by spectral fitting in MBM16, SEP and NEP observation with high $(B_\perp L)^2$ class. The XDB parameters are all consistent with the previous study of the X-ray background. The SWCX+LHB component which gives a OVII line at 574 eV are known to be spatially non-uniform and time-variable. In the spectral fitting for MNM16 and NEP, the normalization were consistent with 0, or that component were not statistically significant. Thus we treated these to be null values. The MWH emissions are represented by one or two thermal component, whose temperature kT are typically (0.15–0.35) keV and (0.6–0.8) keV. The power law indices for the CXB were set free, but consistent with the typical value of 1.4.

Parameter	MBM16	SEP	NEP
$n_{\rm H}{}^*$ (10^{20} cm^{-2})	16.90(fix)	4.72(fix)	3.92(fix)
Norm$_1{}^\dagger$	0(fix)	$33.4^{+88.9}_{-33.4}$¶	0(fix)
kT_2 (keV)	$0.32^{+0.24}_{-0.23}$	-	$0.21^{+0.18}_{-0.13}$
Norm$_2{}^\dagger$	$2.1^{+23.0}_{-1.3}$	0(fix)	$4.1^{+13.5}_{-3.9}$
$\Gamma_{\rm CXB}{}^\ddagger$	$1.33^{+0.16}_{-0.16}$	$1.50^{+0.25}_{-0.23}$	$1.53^{+0.18}_{-0.18}$
$S_{\rm CXB}{}^\S$	$6.5^{+1.1}_{-1.0}$	$5.6^{+0.9}_{-0.8}$	$6.9^{+0.7}_{-0.8}$
kT_3 (keV)	-	$0.66^{+0.08}_{-0.06}$	0.69††
Norm$_3{}^\dagger$	0(fix)	$2.1^{+0.5}_{-0.6}$	$0.3^{+0.7}_{-0.3}$¶
$\Gamma_{\rm ALP}{}^\ddagger$	-0.5(fix)	-0.5(fix)	-0.5(fix)
$S_{\rm ALP}{}^{**}$	$0.005^{+0.022}_{-0.024}$	$0.011^{+0.027}_{-0.030}$	$0.012^{+0.020}_{-0.022}$
C/dof(dof)	1.03(1505)	0.99(1000)	1.10(1503)

All errors indicatte 90% condfidence level.

* The column densities of galactic absorption for the MWH, CXB and HTC component were fixed to the weighted average value

† The emission measure of CIE plasma integrated over the line-of-sight for SWCX+LHB, MWH and HTC (the normalization of *apec* model): $(1/4\pi)\int n_{\rm e} n_{\rm H} ds$ in unit of 10^{14} cm^{-5} sr^{-1}.

‡ The photon index of the *power-law* model for the CXB and ALPs components.

§ The surface brightness of the CXB (the normalization of *power-law* model): in unit of photons s^{-1} cm^{-2} sr^{-1} at 1 keV.

** The surface brightness of the ALP (the normalization of *power-law* model): in unit of photons s^{-1} cm^{-2} sr^{-1} at 1 keV and 10^4 T^{2}m^2.

‖ The goodness of the fit is C/dof.

¶ Parameter pegged at fitting limit: 0.

†† Since the normalization of *apec* allows 0 within the error range, the temperature is not determined.

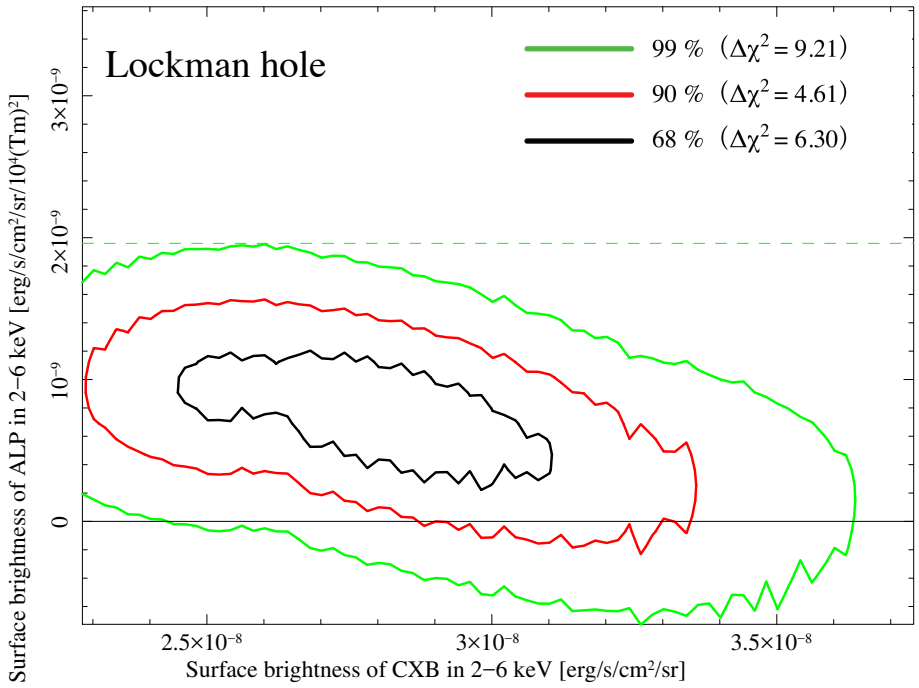

Figure 5.25 The confidence contour between surface brightness of CXB and ALP calculated from the photon index ($\Gamma_{\rm CXB}$ and $\Gamma_{\rm ALP}$) and normalization ($S_{\rm CXB}$ and $S_{\rm ALP}$) as shown in Table 5.7 with Equation (5.7) and (5.8) obtained for all Lockman hole observations, where the NXB normalization parameters were allowed to go free. 3 confidence levels: 68%(*black*), 90%(*red*) and 99%(*green*). *Dashed line*: 99% upper limit for ALP surface brightness.

Table 5.9 Summary of upper limit at 99 % *CL* of surface brightness as shown by dashed line in Figure 5.25 and 5.26, and corresponding cont rate for ALPs originating power-law component in 2–6 keV band.

Field Name	99% UL for ALP surface brightness [10^{-9} erg s^{-1} cm^{-2} sr^{-1} at 10^4 T^2 m^2 in 2–6 keV]	Corresponding count rate [10^{-3} counts s^{-1} at 10^4 T^2 m^2 in 2–6 keV]	Best-fit CXB surface brightness [10^{-9} erg s^{-1} cm^{-2} sr^{-1} in 2–6 keV]
Lockman hole	2.0	10.9	28.3
MBM16	1.6	9.1	26.9
SEP	2.8	14.6	18.6
NEP	1.9	8.9	22.0

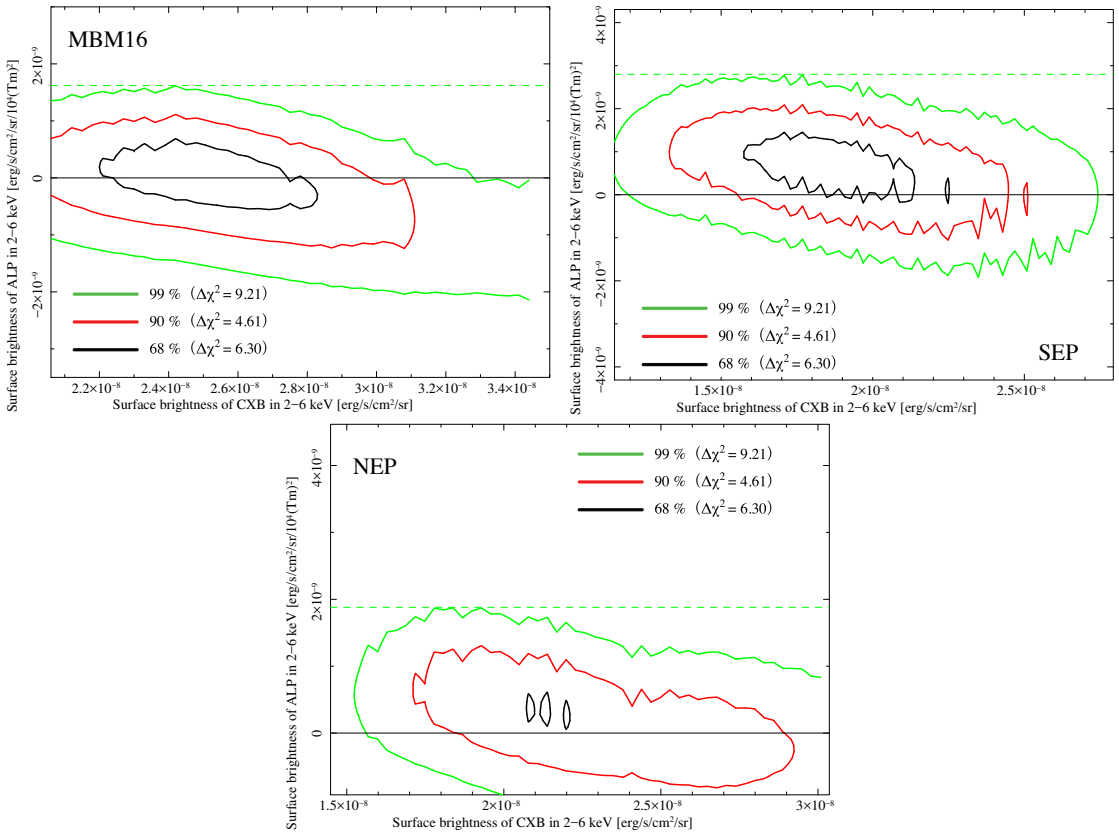

Figure 5.26 The confidence contour between surface brightness of CXB and ALP calculated from the photon index ($\Gamma_{\rm CXB}$ and $\Gamma_{\rm ALP}$) and normalization ($S_{\rm CXB}$ and $S_{\rm ALP}$) as shown in Table 5.8 with Equation (5.7) and (5.8) obtained for all MBM16, SEP, and NEP observations, where the NXB normalization parameters were allowed to go free. *Upper-left*: MBM16 observation. *Upper-right*: SEP observation. *Lower*: NEP observation. 3 confidence levels: 68% (*black*), 90% (*red*) and 99% (*green*). *Dashed line*: 99% upper limit for ALP surface brightness.

6 Unidentified X-ray line emission as a signature from an ALP

6.1 Calculation of sensitivity to ALPs with the 187 individual XDB data

In recent years, Sekiya et al. (2016) has shown the upper limit of the line intensity from decaying dark matter associated with the Milky Way with the deepest XDB observation by stacking 187 individual *Suzaku*/XIS data with total exposure time of 12 Ms. This restriction is applicable not only for decaying dark matter but also for ALP line emission converted by the Earth's magnetic field. The X-ray line intensity $I_{\rm line}$ originating from ALPs is expressed in a product of ALP line intensity $I_{\rm a,line}$ and its conversion rate, $I_{\rm line} = I_{\rm a,line} \times P_{\rm a\to\gamma}$. The obtained upper limit for line emission photons becomes

$$I_{\rm a,line} < \frac{I_{\rm line}}{\int P_{\rm a\to\gamma}\ dt}, \tag{6.1}$$

$$\int P_{\rm a\to\gamma}\ dt \propto \int (B_\perp L)^2\ dt \simeq \left\langle (B_\perp L)^2 \right\rangle . \tag{6.2}$$

We computed the geomagnetic conversion of ALP by the method detailed in Section 4.3 for all 187 observations used by Sekiya et al. (2016). Figure 6.1 shows the stacked histogram of $(B_\perp L)^2$ for each XIS. The exposure time of XIS2 is extremely short because this CCD was stopped from 2006. From these calculations, we obtained that the root means square of $B_\perp L$ is 140 Tm and that the averaged ALPs-photon conversion from Equation (3.9) is:

$$P_{\rm a\to\gamma} \simeq 4.80 \times 10^{-17} \cdot g_{10}^2 \ \left(\frac{B_\perp L}{140\ {\rm Tm}} \right)^2 . \tag{6.3}$$

6.2 Upper limit of line emission for 0.5–7 keV

Sekiya et al. (2016) reported the 3σ upper limits on the line intensity of to be 0.83 photons s^{-1} cm^{-2} sr^{-1} in the 0.5–1.0 keV and 0.021 photons s^{-1} cm^{-2} sr^{-1} in the 1.0–7.0 keV. From Equation (6.3), we obtained the upper limits on the ALP line intensity as shown in Figure 6.2:

$$I_{\rm a,line} \cdot g_{10}^2 < 1.7 \times 10^{16}\ {\rm axions\ s^{-1}\ cm^{-2}\ sr^{-1}} \quad {\rm in\ the\ 0.5-1.0\ keV\ band}, \tag{6.4}$$

$$< 4.4 \times 10^{14}\ {\rm axions\ s^{-1}\ cm^{-2}\ sr^{-1}} \quad {\rm in\ the\ 1.0-7.0\ keV\ band}. \tag{6.5}$$

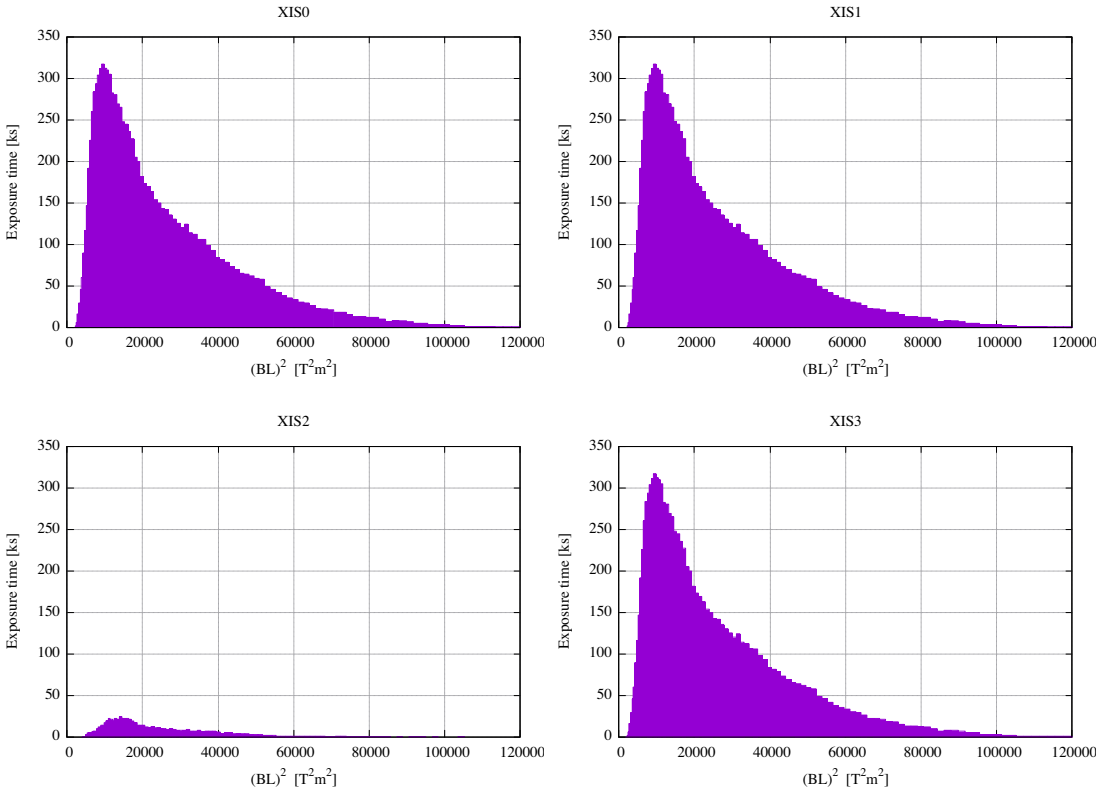

Figure 6.1 The histogram of $(B_\perp L)^2$ stacked with 187 observation of *Suzaku*/XIS

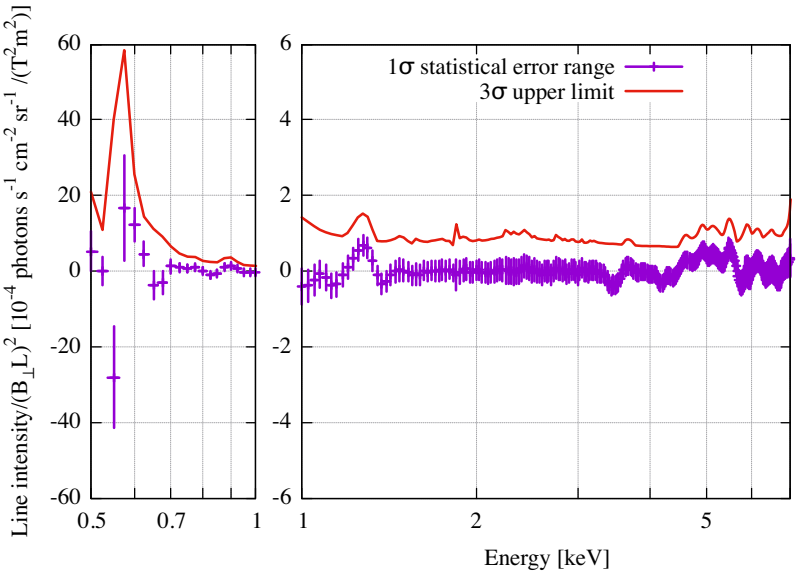

Figure 6.2 Expected ALP line intensity, its 1σ statistical error range and its 3σ upper limit calculated from Sekiya et al. (2016).

7 Discussion

7.1 Summary of X-ray signatures in this ALP search

In order to search the Axion-like particle (ALP) originated X-ray emission, we used *Suzaku* satellite data which has a low Earth orbit, relatively stable and low particle background. The Earth's magnetosphere crossing the field of view from *Suzaku* to the target up to $6R_E$ is expected to convert the ALPs to X-rays via inverse Primakoff process. We obtained the upper limit at 99 % *CL* of the line emission in Chapter 6 and the continuum emission in Chapter 5 originating from the following situations of ALPs as summarized in Table 7.1:

(a) Distributed in the near-Earth presents any-unknown continuum spectral shape.
(b) Distributed in the near-Earth presents line emission.
(c) Cosmological distribution presents continuum emission with a photon index of $-1/2$: $\left(\frac{dN}{dE} \propto E^{+1/2}\right)$

In the ALP search for continuous emission (a) and (c), we did not obtain significant signals above the reproducibility of the non-X-ray background (NXB), as summarized in Table 5.9. First, we selected the 4 suitable blank sky observations from *Suzaku* archive, and applied the standard data screening for all these data. Second, the observed events were divided into 4 or 6 parts by the ALPs-photon conversion rate, which is proportional to $(B_\perp L)^2$ as summarized in Table 5.1 to average the number of events in each class. Third, we evaluated the short and long term fluctuation of the NXB, and obtained systematic errors for these reproducibility. Also we introduced a new criteria for data screening, which is the location ID (detailed in Section 5.4). For case (a), we evaluated the count rate which is proportional to $(B_\perp L)^2$, without assuming any spectral shape of the ALP and also the background emission. It is simplest and minimum assumption. The 3σ upper limit for the count rate by *Suzaku* in 2–6 keV band is 2.0×10^{-3} counts s^{-1} at $(B_\perp L)^2 = 10^4$ T^2 m^2 as shown in Table 5.5 at SEP observation. However, any more investigation cannot be done about this limit, since it is necessary to assume a physical parameter such as a shape of energy spectrum and consider a systematic error. For case (c), we represented the blank sky energy spectra by the X-ray diffuse background (XDB) model, which consists of an unabsorbed collisional ionization equilibrium (CIE) plasma emission model for Solar Wind Charge Exchange and the Local Hot Bubble ($kT \sim 0.1$ keV), an absorbed CIE plasma emission model for the Milky Way Halo ($kT = 0.1$–0.4 keV), an absorbed power-law emission model for Cosmic X-ray Background, and an unabsorbed hot CIE plasma emission model for High Temperature Component (kT

= 0.4–1.2 keV). Then emissions originating in ALPs were searched, assuming the spectral shape of a power-law with a photon index of $-1/2$ in Asaka et al. (1998) (detailed in Section 2.2), and its intensity is proportional to $(B_\perp L)^2$ was not found. The upper limit at 99% *CL* for the surface brightness is 2.8×10^{-9} erg s^{-1} cm^{-2} sr^{-1} or 3.9×10^{-2} $(E/1\ \mathrm{keV})^{+0.5}$ photons s^{-1} cm^{-2} keV^{-1} sr^{-1} or 0.31 photons s^{-1} cm^{-2} sr^{-1} between 2 and 6 keV at $(B_\perp L)^2 = 10^4$ T^2 m^2 as shown in Table 5.9 at SEP observation, with consideration of systematic errors of the spectral shape of the XDB and fluctuation of the NXB. As we explained our assumption in Chapter 3, the ALP-photon conversion rate are described as in Equation (3.10):

$$P_{\mathrm{a}\to\gamma} = 2.45 \times 10^{-21}\ g_{10}^2 \left(\frac{B_\perp L}{\mathrm{Tm}}\right)^2$$

with $g_{10} = g_{a\gamma\gamma}/10^{-10}$ GeV^{-1}. The X-ray intensity originating from ALPs, I_{photon}, becomes

$$I_{\mathrm{photon}} = P_{\mathrm{a}\to\gamma} I_{\mathrm{a}} = 2.45 \times 10^{-17}\ I_{\mathrm{a}}\ g_{10}^2 \left(\frac{B_\perp L}{100\ \mathrm{Tm}}\right)^2 . \tag{7.1}$$

The upper limit of the ALP intensity times ALP-photon coupling constant,

$$I_{\mathrm{a}} \cdot g_{10}^2 = \frac{I_{\mathrm{photon}}}{2.45 \times 10^{-17}} \left(\frac{B_\perp L}{100\ \mathrm{Tm}}\right)^{-2} < \frac{0.31}{2.45 \times 10^{-17}} \left(\frac{B_\perp L}{100\ \mathrm{Tm}}\right)^{-2}, \tag{7.2}$$

is derived from the above equations and the surface brightness.

These upper limits for the continuum emission from ALP are 6–15 % of the observed CXB surface brightness, and are not contradictory to the deep X-ray surveys which resolves 75–80 % of the CXB by the sum of distant point sources, such as AGN (Brandt & Alexander (2015) and references therein).

The upper limit of narrow line emission in X-ray energy band as 0.02 photons s^{-1} cm^{-2} sr^{-1} by Sekiya et al. (2016) could be converted to the upper limit for the ALP intensity as shown by Equation (6.1)–(6.5).

In summary, we used the equations in Chapter 2, and observational results summarized in Table 7.1, we estimated the 99% upper limit of ALP intensity times ALP-photon coupling constant, $I_{\mathrm{a}} \cdot g_{10}^2$, as follows:

(b) $I_{\mathrm{a,line}} \cdot g_{10}^2 < 4.4 \times 10^{14}$ axions s^{-1} cm^{-2} sr^{-1},
(c) $I_{\mathrm{a}} \cdot g_{10}^2 < 1.7 \times 10^{16}$ axions s^{-1} cm^{-2} sr^{-1} $\left(I_a = \int dN/dE_a\right)$.

7.2 Systematic uncertainty

The relationship between $(B_\perp L)^2$ and both the count rate and the X-ray surface brightness is different from our working hypothesis that the ALP origin emission is proportional to the $(B_\perp L)^2$ in the FoV. It might indicate that there is an unknown mechanism to absorb or convert photons by the magnetic fields, or to emit photons at lower $(B_\perp L)^2$. There are

Table 7.1 Summary of upper limit for ALP origin emissions from Chapter 5 and 6. The result of count rate analysis, spectral fitting, and narrow line described in Table 5.5, Table 5.9, and Sekiya et al. (2016), respectively.

Field Name	Count rate analysis	Spectral fitting			Narrow line
	count rate[†]	surface brightness[‡]	count rate[†¶]	CXB ratio [%]	intensity[§]
Situation	(a)		(c)		(b)
Lockman hole	0.57	2.0	10.9	7.1	-
MBM	1.1	1.6	9.1	5.9	-
SEP	2.0	2.8	14.6	15.1	-
NEP	1.0	1.9	8.9	8.6	-
187 data set	-	-	-	-	0.02

[†] In unit of 10^{-3} counts s^{-1} normarized at 10^4 T^2m^2.

[‡] In unit of 10^{-9} erg s^{-1} cm^{-2} sr^{-1} normarized at 10^4 T^2m^2 in 2-6 keV band.

[§] In unit of photon s^{-1} cm^{-2} sr^{-1} for 1-7 keV.

[¶] Including NXB fluctuations.

also possibilities that the lower $(B_\perp L)^2$ region tends to have lower magnetic fields at orbits, and the NXB fluctuate more than the Poisson error estimation by ± 150 days average. We evaluated the systematic uncertainty in this ALP search, which included XDB and NXB reproducibility uncertainties.

In this analysis, we cautiously provided the XDB model by using two statistical methods of parameter estimation[*1] for double-checking. There are enough photon counts with each event and NXB; therefore, we could apply the likelihood by the Gaussian distribution. However, it is necessary to apply the likelihood of Poisson distribution because there are few photon counts in each energy bin with the events divided by $B_\perp L$. We compared the Gaussian data with the Gaussian background to Poisson data with Gaussian background. As summarized in Table 5.6 and D.1, both likelihoods show low statistical uncertainty and consistency of model parameters between two statistical estimations. Cosmic X-ray background (CXB) emission is dominant for the XDB flux above 2 keV, as shown in Figure 3.2. The CXB fluctuation caused by the number variance of point source within XIS/field of view is regarded as almost "0" in the same direction. We estimated that the other CXB fluctuation, according to exposure time, is 2.42×10^{-13}erg s^{-1} cm^{-2} in the lowest time interval ($\sim$ 80 ks). This indicates that the uncertainty in the XDB model is sufficiently small.

In the continuum search, the favorable influence of NXB reproducibility must be considered. The NXB count rate was studied for each location ID to reject the high count rate, as described in Section 5.4. Tawa et al. (2008) reported that the reproducibility of the NXB model count rate estimated by cut-off-rigidity (COR) was 3.4 % or less in the 1–7 keV band for each 50 ks exposure of the NXB data. We examined the fluctuation of the NXB count

[*1] https://heasarc.gsfc.nasa.gov/xanadu/xspec/manual/XSappendixStatistics.html

rate calculated by standard estimation (COR selection) and updated estimation (Location ID selection). In both cases, the uncertainty of the NXB count rate between 2.0 and 5.6 keV is $\sim 20\%$ within 1σ statistical error. In addition, the NXB above 12 keV, where the effective area of XRTs is smaller than 1% of 2–6 keV band, was studied to find that the NXB fluctuation in 12–15 keV is 30%, as shown in Table 5.3. In the search for contribution from ALPs to XDB, the count rate in the 2.0–6.0 keV band implied the negative relation of $(B_\perp L)^2$, as shown in Figures 5.17 in Chapter 5. This is different from the model supposed for ALPs in this thesis. Though there is a possibility that a conversion to ALP from XDB by geomagnetic field is suggested, it is not a significant detection because it is not possible to distinguish with a systematic error such as NXB reproducibility. Thus we applied the interpolation model of NXB to include NXB uncertainty. The upper limit of ALP surface brightness is evaluated by confidence contour calculated from spectral fitting of the XDB + ALP + NXB model.

7.3 Upper limit on ALP-photon coupling constant

In this section, we considered the case of some particles contributing to dark matter (e.g. moduli) decay to ALPs (Cicoli et al., 2014; Higaki et al., 2014). We limited the ALP intensity times its conversion rate to photons in Section 7.1. If we assume the dark matter density and decay rate, we can limit the ALP-photon coupling constant. Given an oscillation length $L \sim 6\mathrm{R_E}$, the sensitivity of ALP masses is in the range of less than 3.3×10^{-6} eV as shown in Equation (3.11). Two candidates of dark matter density decaying to ALPs as the following:

(B) Dark matter exists in the solar system neighborhood.
(C) Dark matter is distributed over the universe uniformly.

Assuming that the decay rate from dark matter to ALPs, $\Gamma_{\Phi\to 2a}$, is the inverse of its lifetime, the X-ray line intensity from dark matter as shown in Equation (2.6) becomes

$$I_{\mathrm{DM}} = P_{\mathrm{a}\to\gamma} I_{\mathrm{a,line}} = P_{\mathrm{a}\to\gamma} \frac{S_\phi \Gamma_{\phi\to 2a}}{2\pi m_\phi}, \tag{7.3}$$

where m_Φ is a dark matter mass. We obtainted the upper limit on ALP-photon coupling constant as follows:

$$g_{\mathrm{a}\gamma\gamma} < \sqrt{\frac{1}{2.45\times 10^{-21}} \frac{I_{\mathrm{DM}}}{I_{\mathrm{a,line}}}} \, (B_\perp L)^{-1}, \tag{7.4}$$

shown in Equation (3.9). In the case of line emission (B), the dark matter density around the Solar system observed in the *Suzaku* archival data set used by Sekiya et al. (2016) was estimated as 50–100 $M_\odot$ pc^{-2} with an assumption of the Galaxy mass and NFW(Navarro-Frenk-White)-like density profile. The decay rate of the dark matter is highly unknown. The dark matter still exists in the Universe, and decays to ALPs, a decay time comparable to

the age of the Universe or longer, t_0 =13.7 Gyr or 4.32×10^{17} s is a very crude assumption. Thus, we assume the normalization values as follows;

- $S_\Phi \simeq 50$ M$_\odot$ pc^{-2}
- $m_\Phi \sim 0.5 - 3.5$ keV in the X-ray band
- $\Gamma_{\Phi\to 2a} = \dfrac{1}{\tau_\phi} < \dfrac{1}{t_0} = \dfrac{1}{4.32 \times 10^{17}\ \mathrm{s}}$.

We obtained the following 3σ upper limit of ALP-photon coupling constant from Chapter 6:

$$g_{\mathrm{a}\gamma\gamma} < 8.4 \times 10^{-8}\ \mathrm{GeV}^{-1} \left(\frac{B_\perp L}{140\ \mathrm{Tm}}\right)^{-1} \left(\frac{\tau_\phi}{4.32 \times 10^{17}\ \mathrm{s}}\right)^{1/2} \left(\frac{S_\phi}{50\ \ \mathrm{M}_\odot \mathrm{pc}^{-2}}\right)^{-1/2}. \quad (7.5)$$

In the case of continuous emission (C), we assume a continuum spectrum created by the superposition of monochromatic lines with different cosmological redshifts:

$$\frac{dN}{dE} = P_{\mathrm{a}\to\gamma}\frac{dN}{dE_a} = P_{\mathrm{a}\to\gamma}\frac{\sqrt{2}c\Gamma_{\phi\to 2a}\rho_{\phi_0}}{\pi H_0} m_\phi^{-\frac{5}{2}}\ E_a^{\frac{1}{2}}\ f\left(\frac{m_\phi}{2E_a}\right). \quad (7.6)$$

Here, we assume the same dark matter decay time comparable to the age of the Universe, and dark matter density to fulfill the critical density ρ_{cr} with $\Omega_m = 0.258$. The assumptions of our calculation are described below using $h = 0.68$:

- $H_0 = 100\ h$ km s^{-1} Mpc^{-1} $= h \times (3.09 \times 10^{17}\ \mathrm{s})^{-1} = 2.20 \times 10^{-18}\ \mathrm{s}^{-1}\left(\dfrac{h}{0.68}\right)$
- $\rho_{\mathrm{cr}} = 1.88 \times 10^{-29}\ h^2$ g cm^{-3} $= 8.63 \times 10^{-30}$ g cm$^{-3}\left(\dfrac{h}{0.68}\right) = 4.84$ keV c^{-2} cm^{-3}
- $\Gamma_{\Phi\to 2a} = \dfrac{1}{\tau_\phi} < \dfrac{1}{t_0} = \dfrac{1}{4.32 \times 10^{17}\ \mathrm{s}}$.

We also obtained the 99% upper limit of ALP-photon coupling constant at $m_\phi < 3.3 \times 10^{-6}$ eV from Chapter 5,

$$g_{\mathrm{a}\gamma\gamma} < 4.4 \times 10^{-7}\ \mathrm{GeV}^{-1}\ \left(\frac{m_\phi}{10\ \ \mathrm{keV}}\right)^{5/4} \left(\frac{\tau_\phi}{4.32 \times 10^{17}\ \mathrm{s}}\right)^{1/2} \left(\frac{B_\perp L}{100\ \mathrm{Tm}}\right)^{-1} \left(\frac{\rho_\phi}{1.25\ \mathrm{keV\ cm}^{-3}}\right)^{-1/2} \left(\frac{H_0}{2.20 \times 10^{-18}\ \mathrm{s}^{-1}}\right)^{1/2} \left(\frac{f}{1.92}\right)^{-1/2}, \quad (7.7)$$

where the $f(x) = [\Omega_{m0} + (1 - \Omega_{m0} - \Omega_{\Lambda 0})/x - \Omega_{\Lambda 0}/x^3]^{-1/2} \simeq 1/\sqrt{\Omega}_m$, as same definition is Asaka et al. (1998). The constraint of the ALPs parameters has shown in Figure 7.1.

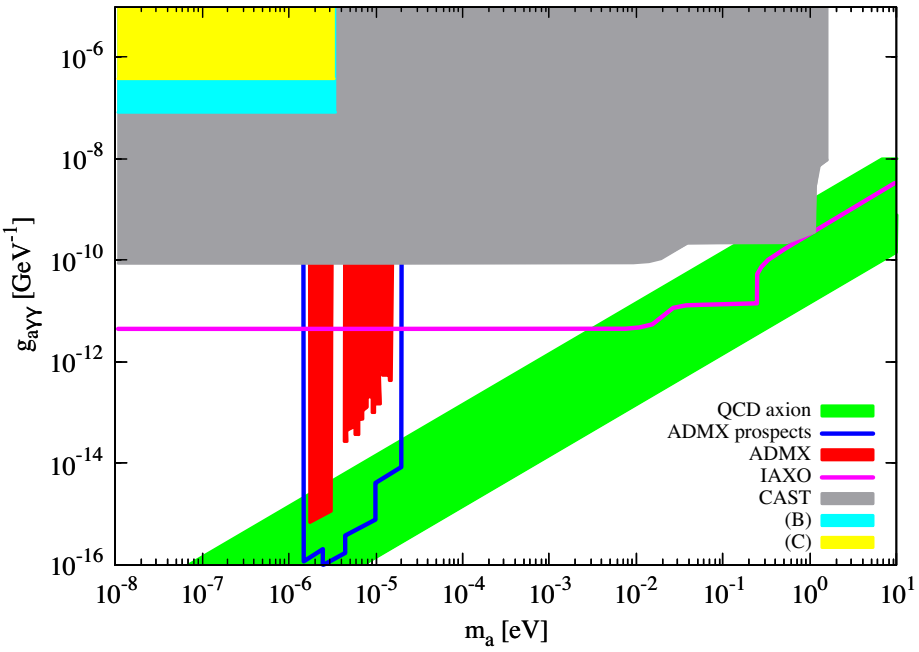

Figure 7.1 ALP parameters constrains in this thesis the same as Figure 2.1 in case (B) (*cyan*) and (C) (*yellow*) see details in text.

8 Conclusions

In this thesis, we searched for X-ray emission from axion-like particles (ALPs) interacting with the Earth's magnetic field in the X-ray diffuse background spectra taken by *Suzaku*/XIS. Energy spectra of ALPs which has been decayed from CMB particles could be continuous or monochromatic. Wavelength of electromagnetic emission from ALPs via inverse Primakoff process depends on the mass of assumed dark matter and ALPs.We noticed that the emission can be detected in X-ray band, and that the efficiency of the inverse Primakoff process by satellite observatories and the Earth magnetosphere is larger than the present ground-based experiments. *Suzaku* is suitable for this observation because of its low Earth orbit and very low intrinsic background.

For the line emission search in X-ray band, previous work by Sekiya et al. (2016) collected the longest exposure of 12 Ms from 10 years of *Suzaku* archival data. The ALP-photon conversion rate, $P_{\mathrm{a}\to\gamma} \propto (B_\perp L)^2$, was computed by using the International Geomagnetic Reference Field of the 12th generation (IGRF-12) model of the Earth's magnetic field and orbital calculation for *Suzaku* data in every 60 seconds. These calculations confirmed that we obtained average ALP-photon conversion rates with satellite observations ($B_\perp L \simeq 140$ Tm) larger than the ground observation ($B_\perp L \simeq 84$ Tm).

Assuming that dark matter has been distributed uniformly after the big-bang, and is decaying with the constant rate, the energy spectrum of ALP becomes a continuous power-law shape with an index of $+1/2$ due to the expansion of the Universe. Our approach was to select long exposure observations for the diffuse X-ray background. The emission from ALPs should be proportional to $(B_\perp L)^2$ along the line-of-sight, which varies by the position of the satellite in orbit relative to the Earth's magnetosphere. We have selected 4 fields of views which have observed several times for calibration and cosmic X-ray background (CXB) study, Lockman hole, MBM 16, North Ecliptic Pole (NEP), and South Ecliptic Pole (SEP). The calculations of $(B_\perp L)^2$ at the orbit also confirmed that the $B_\perp L$ changed about a factor of 5, from 60 Tm to 300 Tm in the same line-of-sight. It enable us to search the ALP mass in the range less than 3.3×10^{-6} eV in simple coherence condition shown in Equation (3.11).

The observed spectrum above 2 keV is dominated by the CXB and non-X-ray background (NXB) which are pseudo events by particle background and fluorescence lines. CXB is considered to be a sum of weak and distant sources which can not be identified, and can not be time-variable at least short time range. A 75–80 % of the CXB are resolved into faint point sources by deep X-ray observations (Brandt & Alexander, 2015). NXB are time-variable due to the flux of Cosmic rays on the satellite. The NXB of *Suzaku* was studied

by Tawa et al. (2008), and an estimation method of the NXB by the Cut-off-Rigidity sorted database was established as the standard analysis method. In our study, the systematic uncertainty of the reproducibility of the NXB was dominant. We found that the standard NXB estimation method used in *Suzaku* analysis is not applicable to the recent change of its orbit and Earth's magnetic field. We quantitatively evaluate the short term fluctuation of the background using the background event (12–15 keV) above the X-ray mirror reflection range and found it was larger than the previous papers, to be 20–40%. We took into account these fluctuations in the spectral fitting to limit the ALP emission for the first time. We also introduced a new parameter, `LOC_ID`. `LOC_ID` is an indicator of latitude and longitude of satellite location, and used for data reduction and secondary NXB estimation method in this thesis.

After these data reduction, we modeled the diffuse background emission of 4 observing field-of-views, which were consistent with previous studies. Then we put an additional component of a power-law model with a photon index of +1/2, ($dN/dE \propto E^{1/2}$), whose intensity is proportional to the $(B_\perp L)^2$ in the field of view. We did not detect any possible continuous emission from ALPs reported by previous similar studies (Fraser et al., 2014). We obtained the upper limit at 99 % *CL* of the X-ray surface brightness and flux from ALPs in the 2.0–6.0 keV energy range as 2.8×10^{-9} erg s^{-1} cm^{-2} sr^{-1}, at $(B_\perp L)^2 = 10^4$ T^{2}m^2 as shown in detail in Chapter 5. It corresponds to the $6 \sim 15$ % of the apparent CXB surface brightness in 2–6 keV band, and it is consistent with that 75–80 % of the CXB are resolved into the point sources. In other words, this 99% *CL* upper limit corresponds to 1/4–3/4 of the unresolved CXB. Upper limit for the line emission by Sekiya et al. (2016) was compiled firstly for the ALP upper limit using an average $(B_\perp L)^2 = 140$ Tm as in Chapter 6.

Assuming that dark matter, such as moduli, decays ALPs, the ALP-photon coupling constant, $g_{a\gamma\gamma}$, was constrained in the ALP mass range of $m_a < \sqrt{2\pi E/L} \sim 3.3 \times 10^{-6}$ eV to be

$$g_{a\gamma\gamma} < 4.4 \times 10^{-7}\ \mathrm{GeV}^{-1} \left(\frac{m_\phi}{10\ \mathrm{keV}}\right)^{5/4} \left(\frac{\tau_\phi}{4.32 \times 10^{17}\ \mathrm{s}}\right)^{1/2} \left(\frac{B_\perp L}{100\ \mathrm{Tm}}\right)^{-1} \left(\frac{\rho_\phi}{1.25\ \mathrm{keV\ cm^{-3}}}\right)^{-1/2} \left(\frac{H_0}{2.20 \times 10^{-18}\ \mathrm{s^{-1}}}\right)^{-1/2} \left(\frac{f}{1.92}\right)^{-1/2}. \quad (8.1)$$

as shown in Figure 7.1. Likewise, a $g_{a\gamma\gamma}$ estimated from the upper limit on the intensities of X-ray line emission shown by Sekiya et al. (2016) is

$$g_{a\gamma\gamma} < 8.4 \times 10^{-8}\ \mathrm{GeV}^{-1} \left(\frac{B_\perp L}{140\ \mathrm{Tm}}\right)^{-1} \left(\frac{\tau_\phi}{4.32 \times 10^{17}\ \mathrm{s}}\right)^{1/2} \left(\frac{S_\phi}{50\ \mathrm{M_\odot pc^{-2}}}\right)^{-1/2}, \quad (8.2)$$

when the ALP density is connected with dark matter density around our galaxy. This restriction of a physical parameter of ALPs is not more strict than other experiments (e.g. CAST, ADMX), which assume a different axion and ALP model than this research. Never-

theless, it is important to note that we found these restrictions by using a new independent method from X-ray observations.

A Details of observational data with *Suzaku*/XIS

Table A.1: Observational logs of the XDB in long term with *Suzaku*/XIS

ID	ObsID	Equatorial (2000) (RA, Dec)	Galactic (l, b)	Start Date	Exposure*
		Lockman hole			
1	101002010	(162.937, 57.256)	(149.703, 53.201)	2006/05/17	80.4
2	102018010	(162.926, 57.258)	(149.707, 53.195)	2007/05/03	96.1
3	103009010	(162.937, 57.255)	(149.705, 53.202)	2008/05/18	83.4
4	104002010	(162.938, 57.255)	(149.704, 53.202)	2009/06/12	92.8
5	105003010	(162.938, 57.251)	(149.709, 53.205)	2010/06/11	78.0
6	106001010	(162.927, 57.253)	(149.713, 53.199)	2011/05/04	42.3
7	107001010	(162.920, 57.255)	(149.715, 53.195)	2012/05/05	35.9
8	108001010	(162.944, 57.275)	(149.674, 53.191)	2013/11/06	38.8
9	109014010	(162.940, 57.278)	(149.674, 53.187)	2014/11/30	37.1
		MBM16			
11	507076010	(49.752, 11.602)	(170.572, -37.268)	2012/07/31	24.9
12	507076020	(49.769, 11.580)	(170.606, -37.272)	2013/02/08	81.0
13	508078010	(49.765, 11.582)	(170.600, -37.274)	2013/08/07	82.3
14	508078020	(49.771, 11.580)	(170.607, -37.271)	2014/02/03	87.9
15	509073010	(49.764, 11.584)	(170.598, -37.273)	2014/07/29	78.8
16	509073020	(49.770, 11.580)	(170.607, -37.272)	2015/02/04	92.0
		SEP			
17	504069010	(89.966, -66.577)	(276.403, -29.825)	2009/11/14	51.9
18	504071010	(89.966, -66.571)	(276.396, -29.825)	2009/12/05	58.0
19	504073010	(89.958, -66.568)	(276.393, -29.828)	2009/12/14	44.4
20	504075010	(89.980, -66.568)	(276.393, -29.819)	2009/12/27	50.0
		NEP			
21	504070010	(270.049, 66.560)	(96.383, 29.792)	2009/11/15	56.3
22	504072010	(270.052, 66.566)	(96.389, 29.791)	2009/12/07	48.7

Table continued on next page.

Continued from previous page.

ID	ObsID	Equatorial (RA, Dec)	Galactic (l, b)	Start Date	Exposure
23	504074010	(270.048, 66.570)	(96.394, 29.792)	2009/12/15	50.2
24	504076010	(270.045, 66.579)	(96.405, 29.794)	2009/12/29	49.8

$*$ in unit of ks

B Background count rate dependence on the Location ID in *Suzaku*/XISdata

B.1 Rejection of each ObsID in this thesis

We estimated the count rate between 2.0 and 5.6 keV as a function of location ID for each observation.

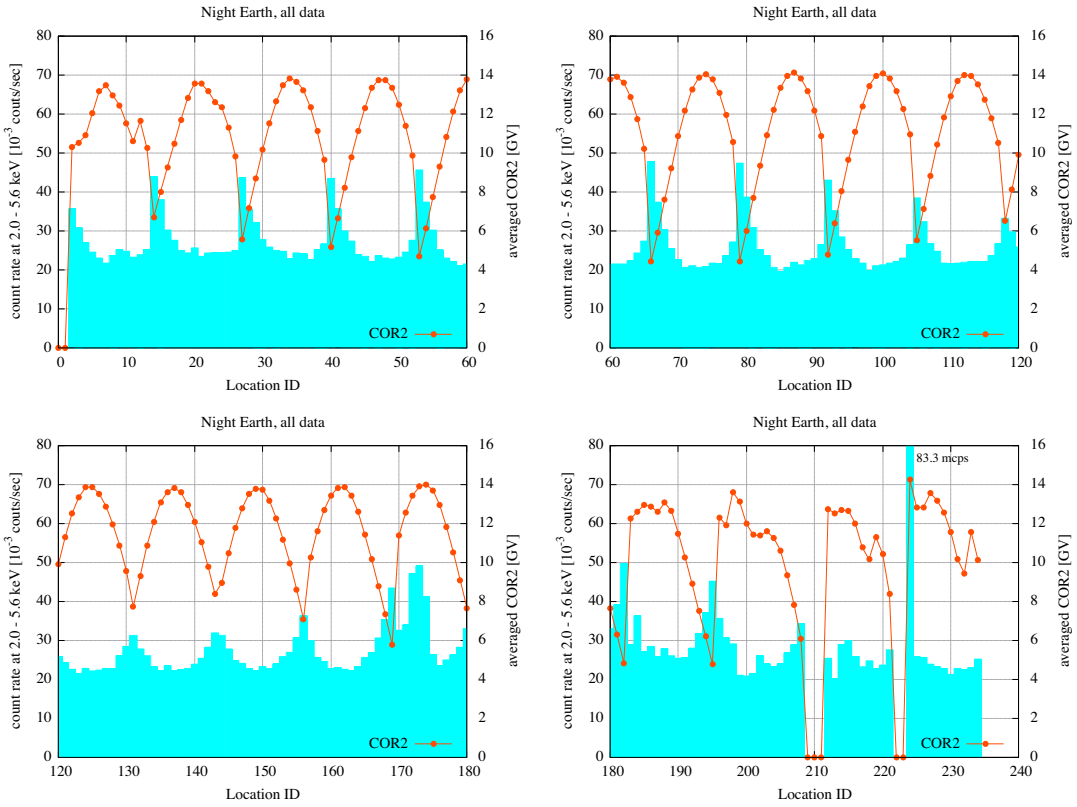

Figure B.1 The count rate of Non X-ray background between 2 and 5.6 keV (left axis) during the XIS FoV was osculated by the night Earth as a function of COR. The time-averaged COR at each location ID is also plotted (right axis).

The result of the rejection shown in Figure B.2-B.13 indicates that the method can eliminate the `LOC_ID` of high count rates in each COR division. This rejection method is described in Section 5.4.

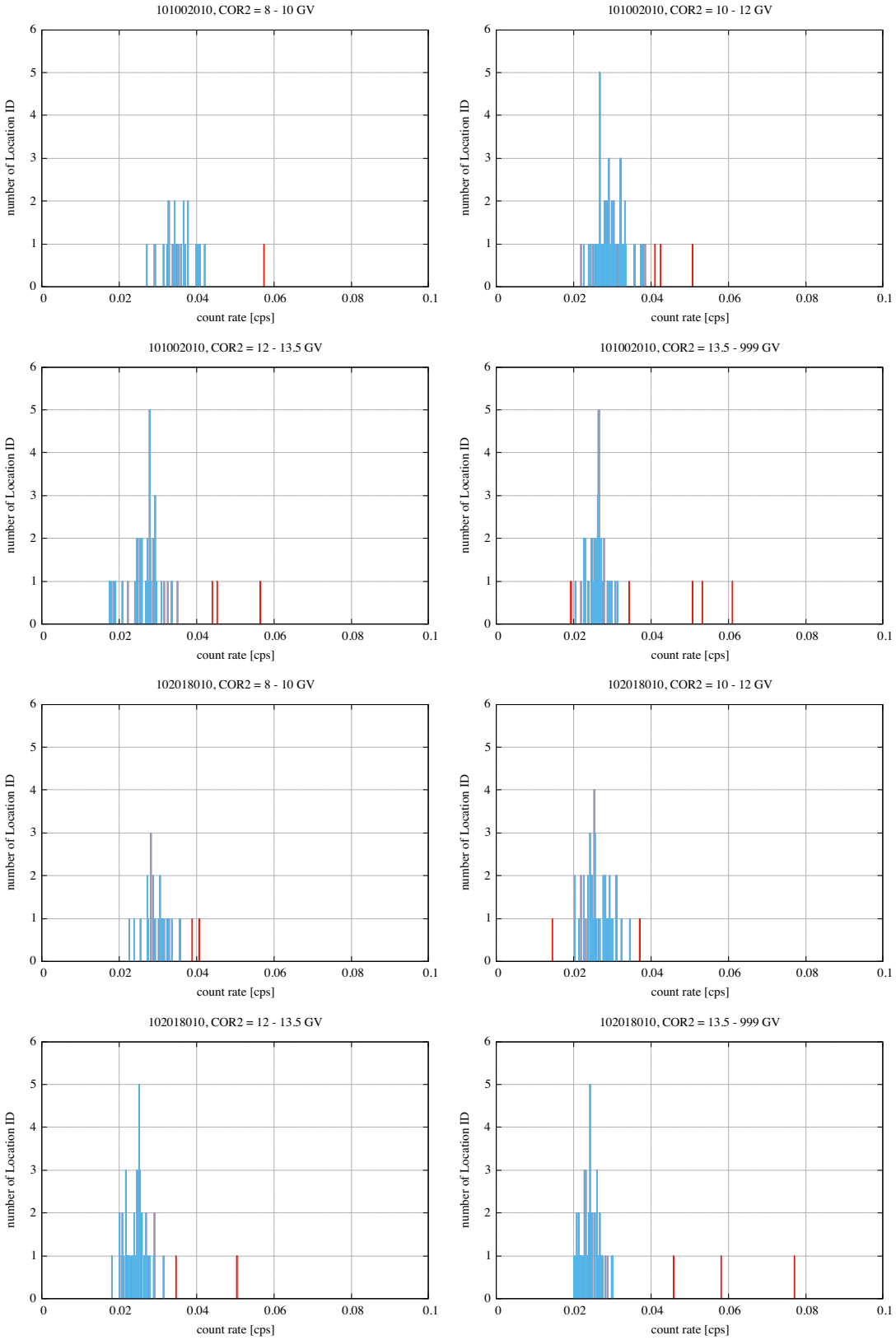

Figure B.2 The histogram of count rate in the 4 `COR2` range, 8-10, 10-12, 12-13.5, 13.5-20 GV/c

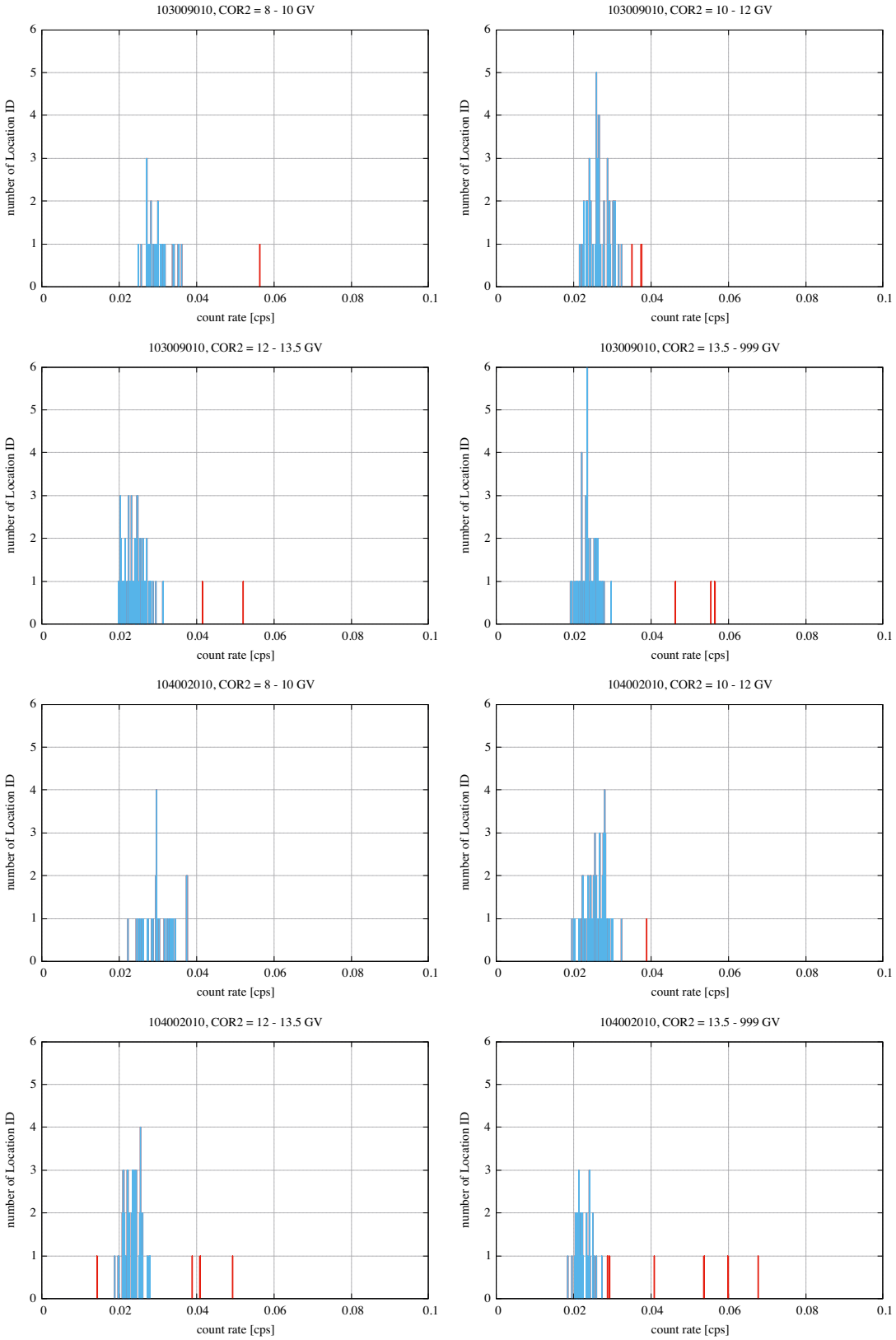

Figure B.3 Same as Figure B.2 but for the ObsID of 103009010 and 104002010

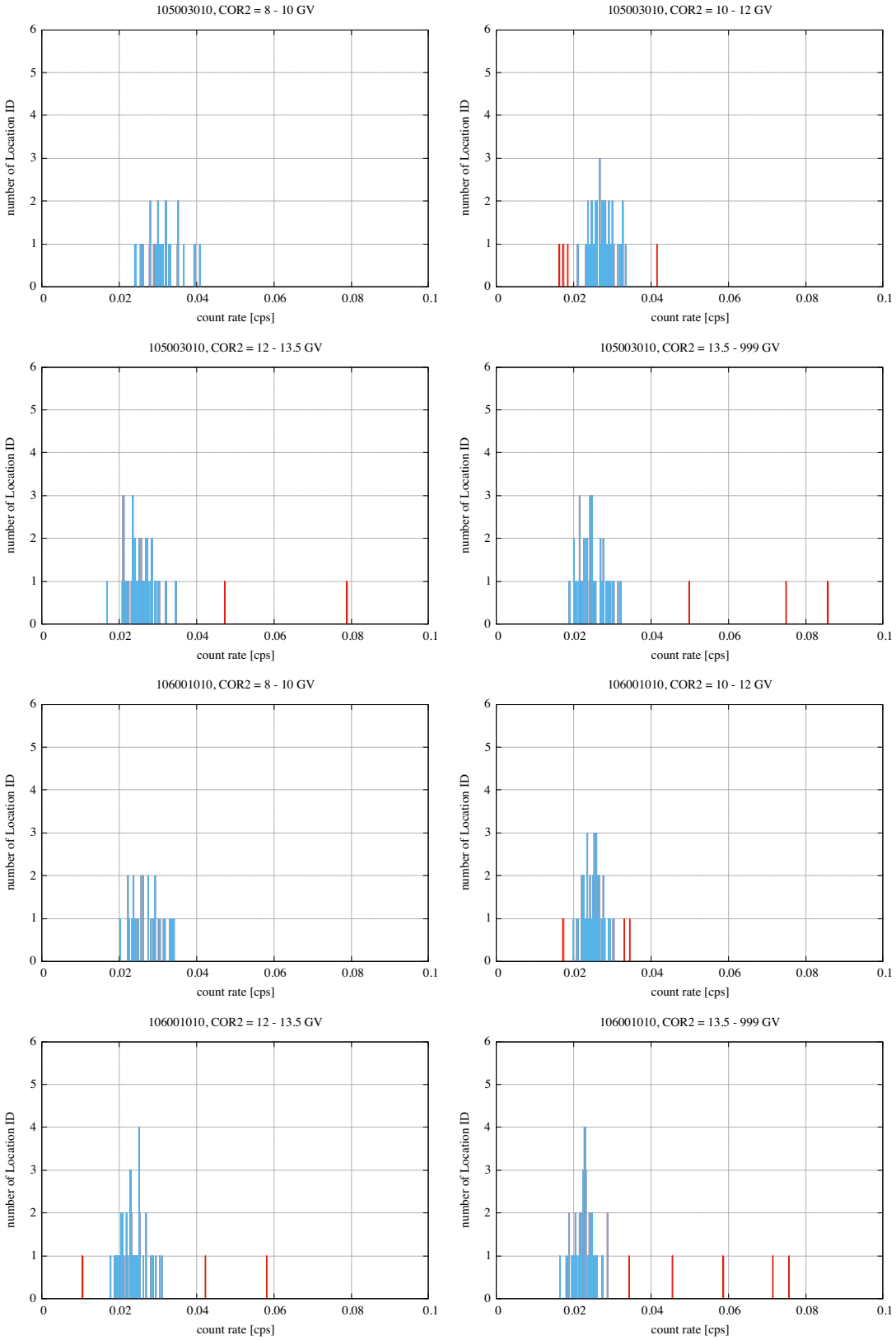

Figure B.4 Same as Figure B.2 but for the ObsID of 105003010 and 106001010

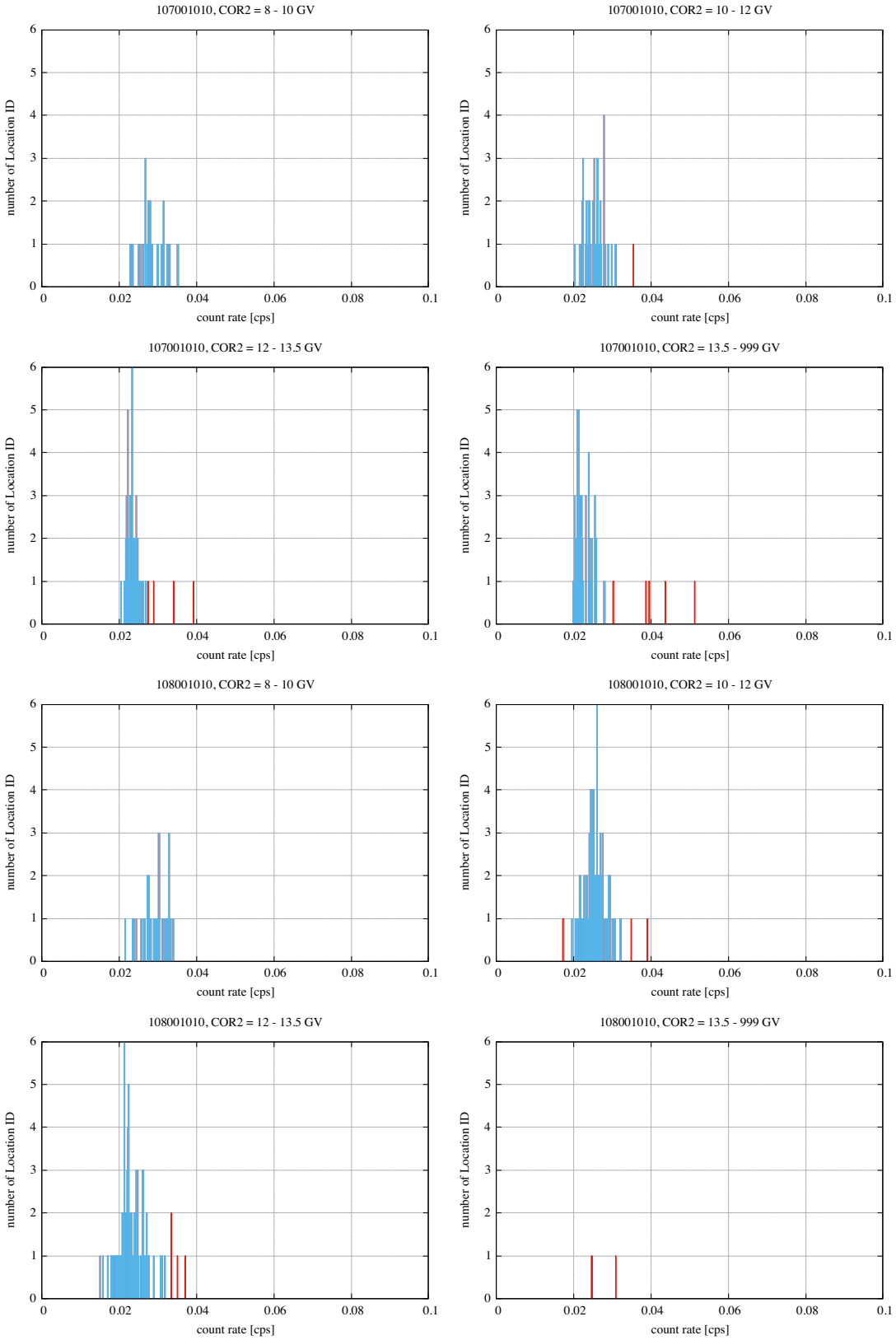

Figure B.5 Same as Figure B.2 but for the ObsID of 107001010 and 108001010

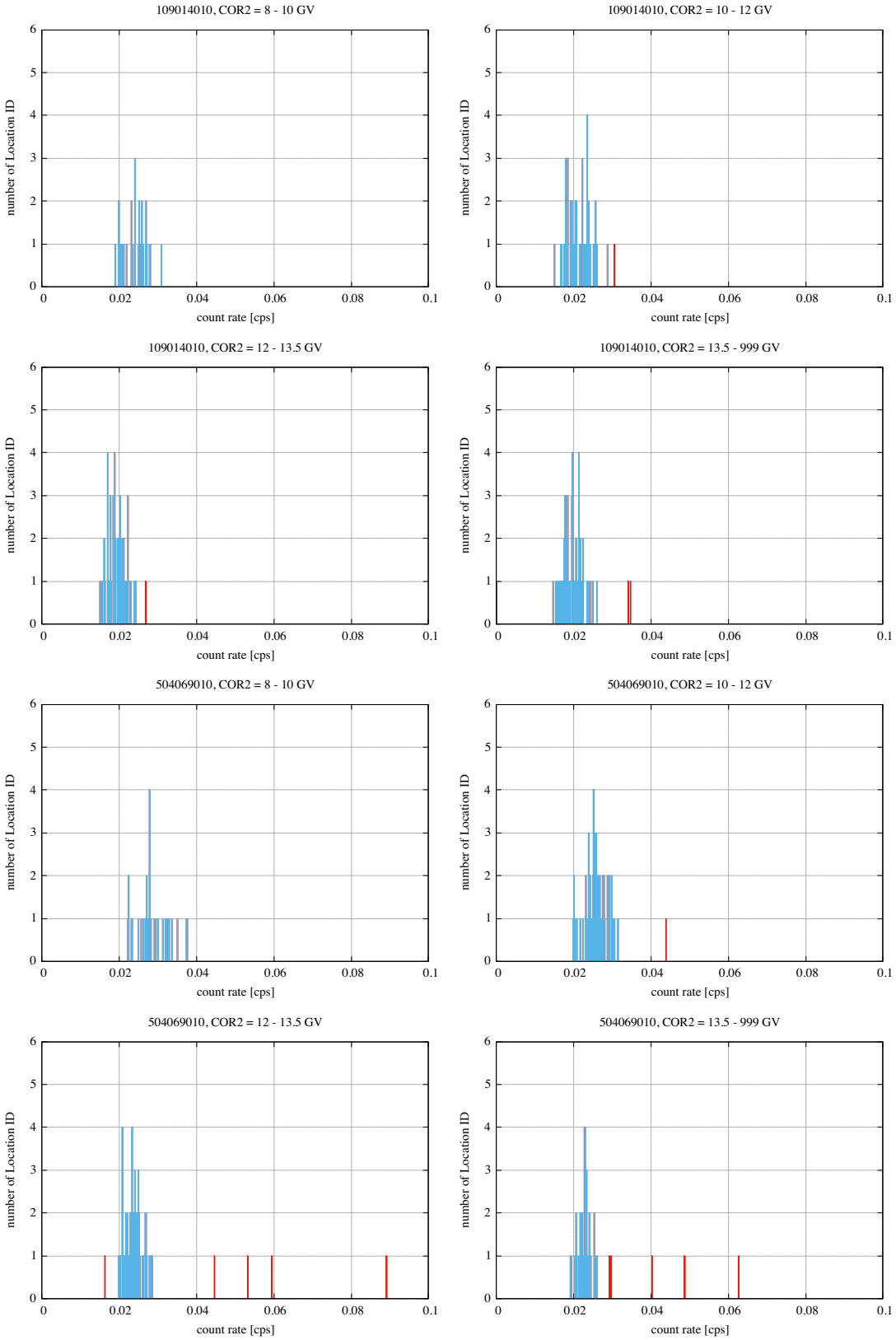

Figure B.6 Same as Figure B.2 but for the ObsID of 109014010 and 504069010

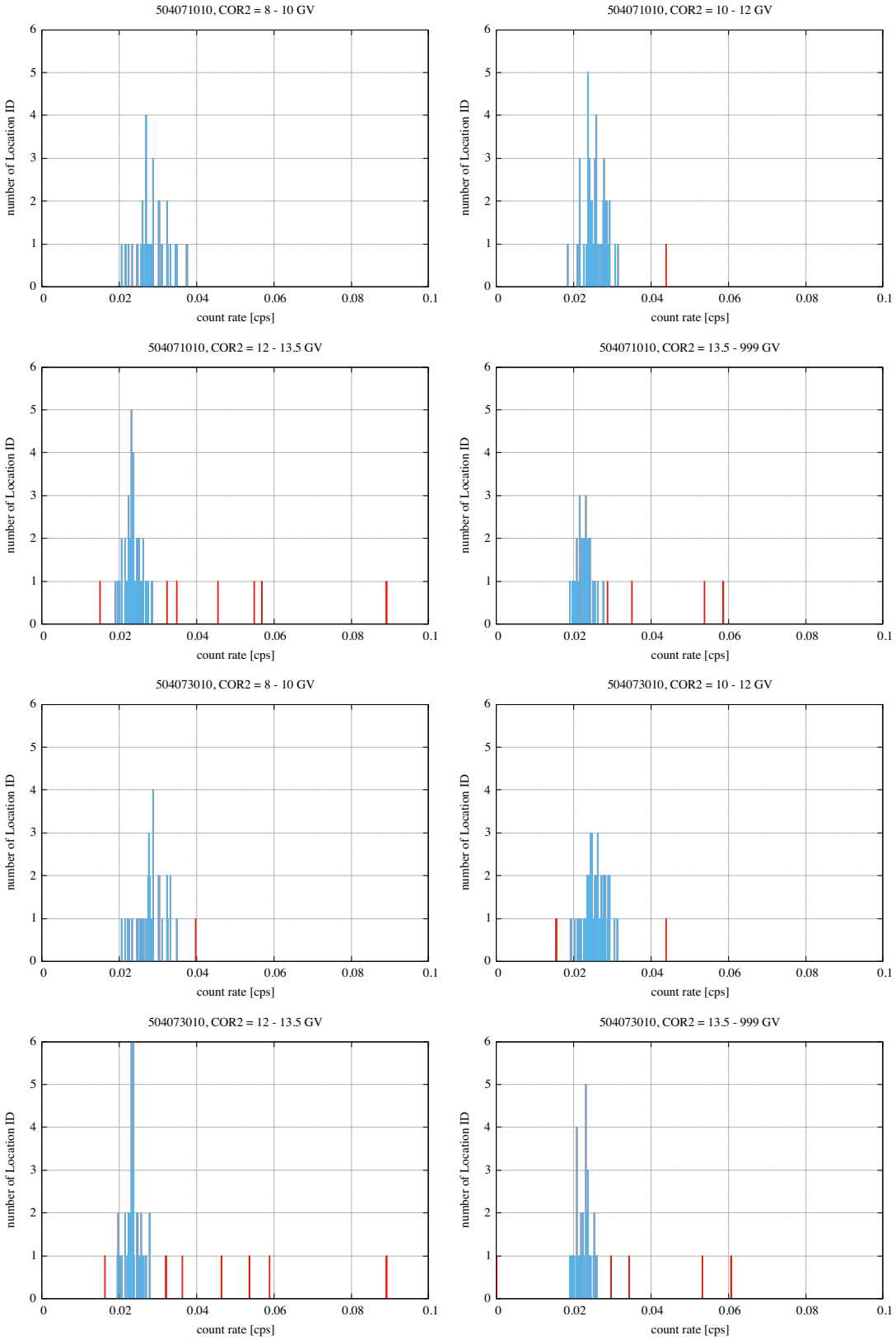

Figure B.7 Same as Figure B.2 but for the ObsID of 504071010 and 504073010

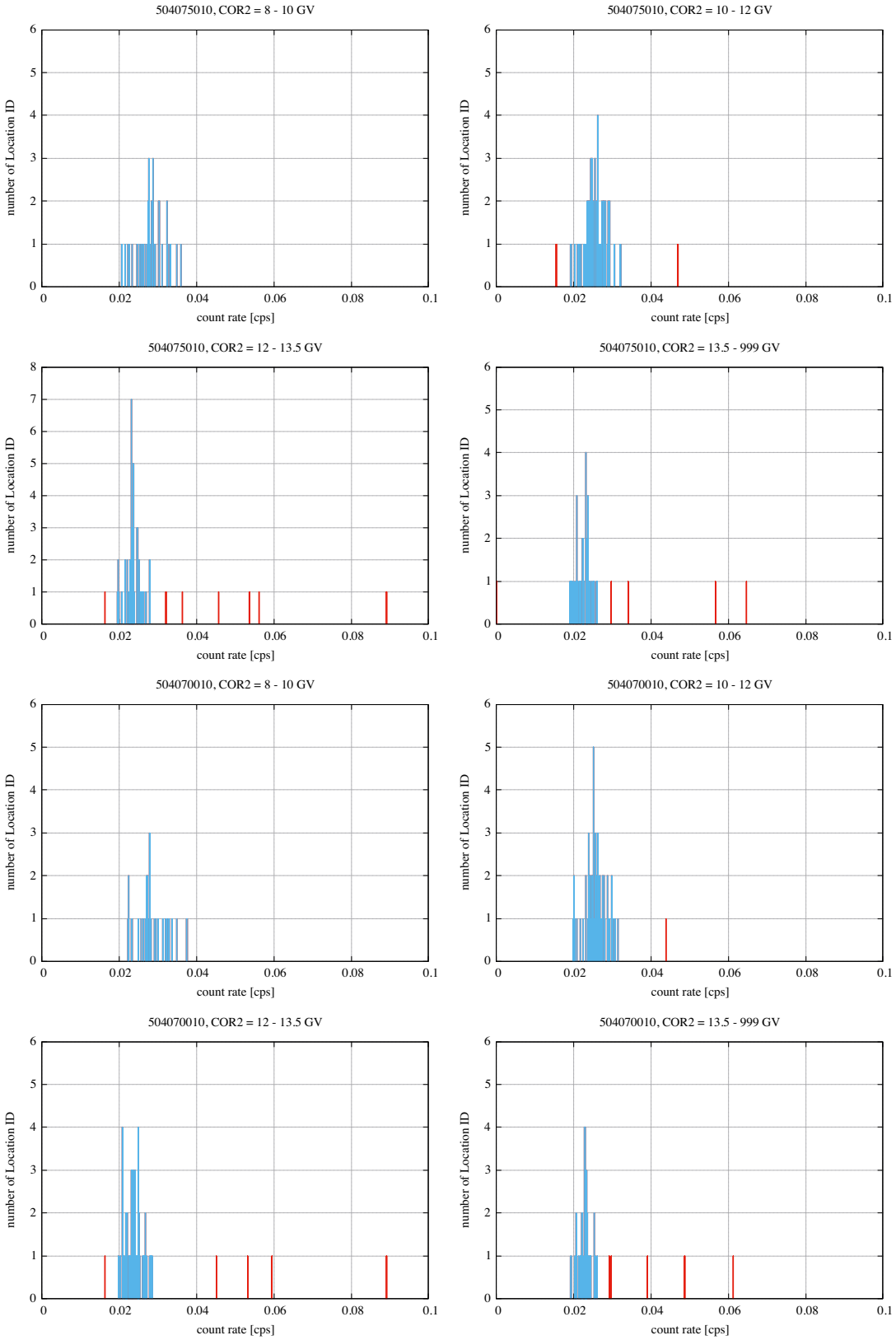

Figure B.8 Same as Figure B.2 but for the ObsID of 504075010 and 504070010

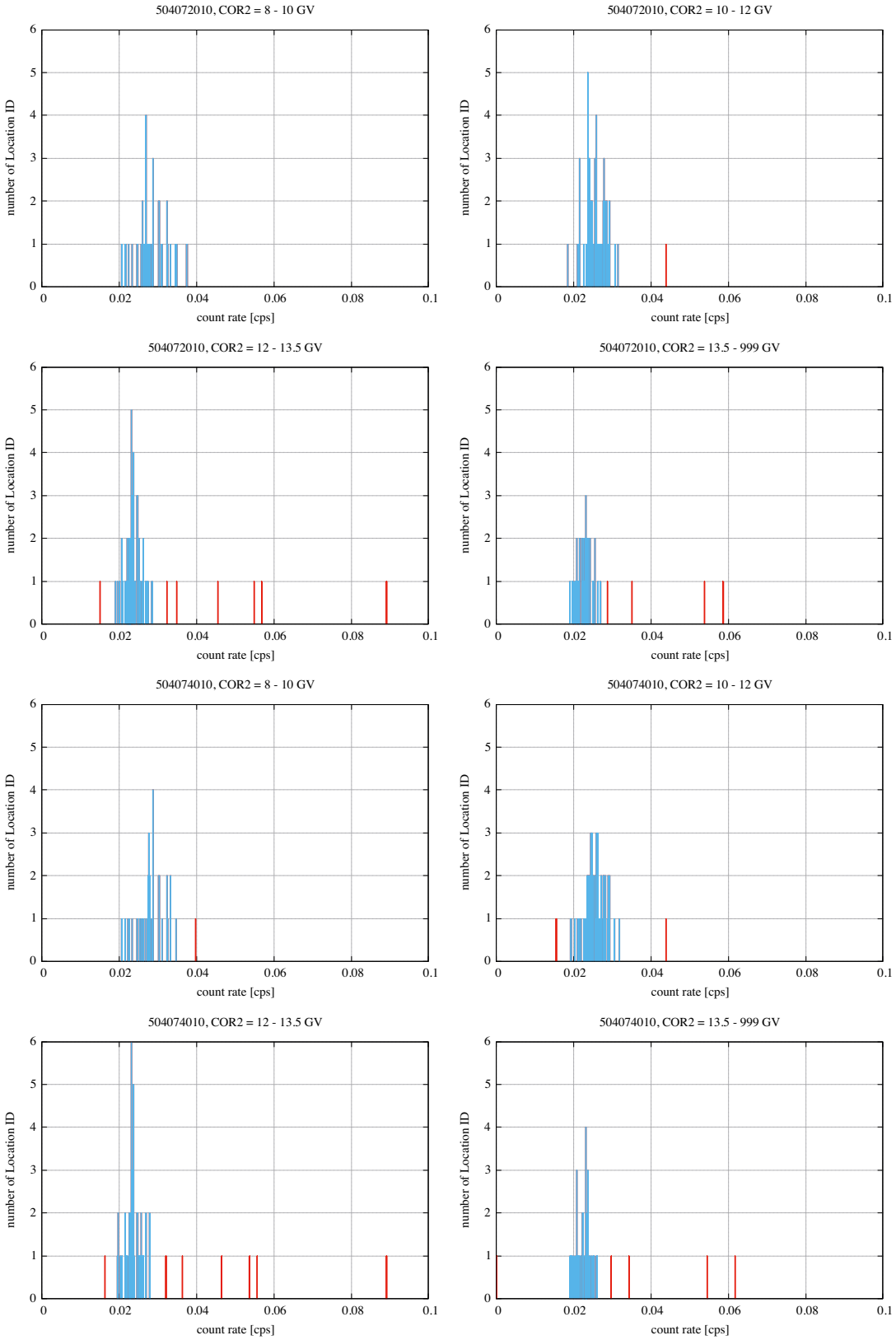

Figure B.9 Same as Figure B.2 but for the ObsID of 504072010 and 504074010

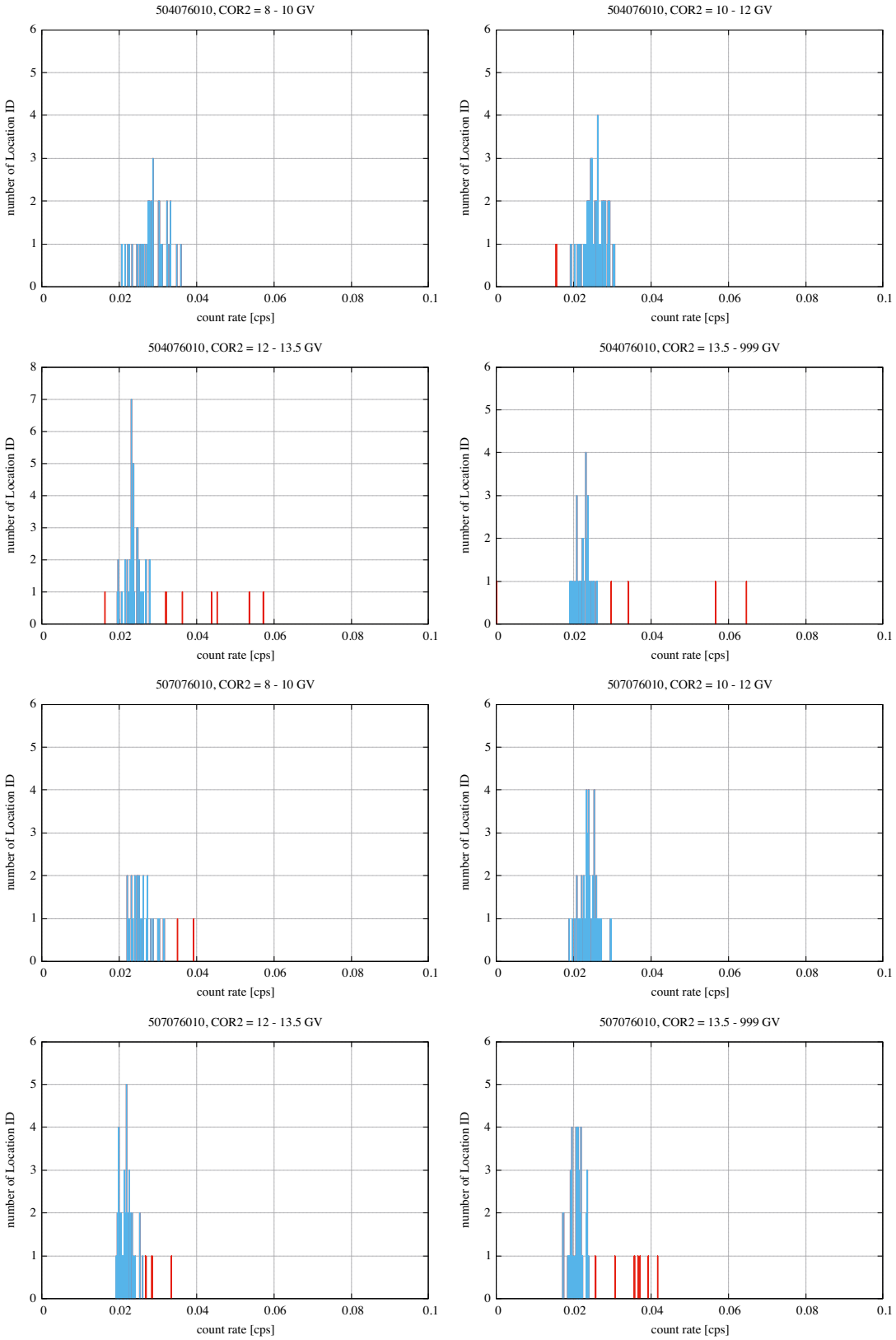

Figure B.10 Same as Figure B.2 but for the ObsID of 504076010 and 507076010

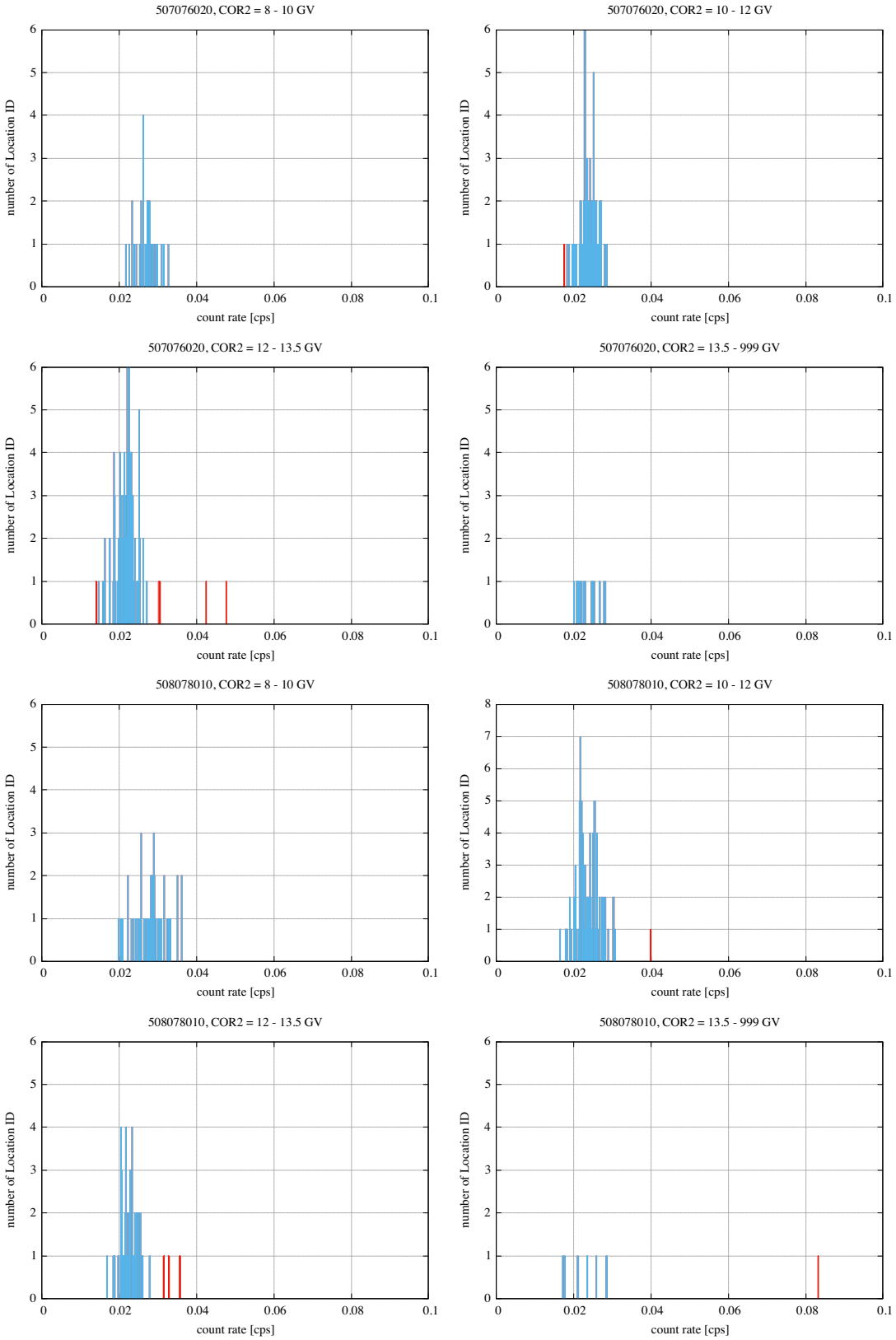

Figure B.11 Same as Figure B.2 but for the ObsID of 507076020 and 508078010

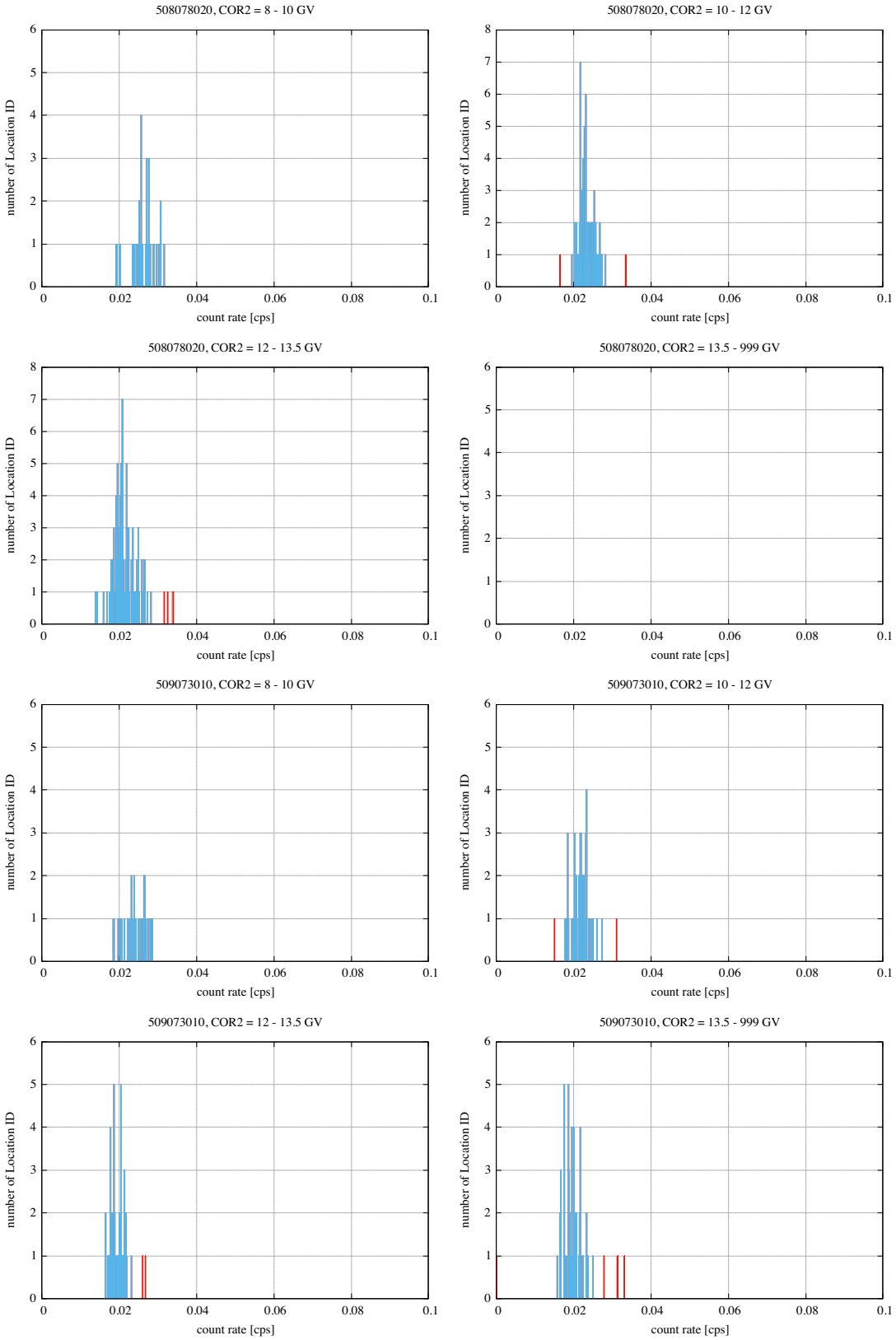

Figure B.12 Same as Figure B.2 but for the ObsID of 508078020 and 509073010

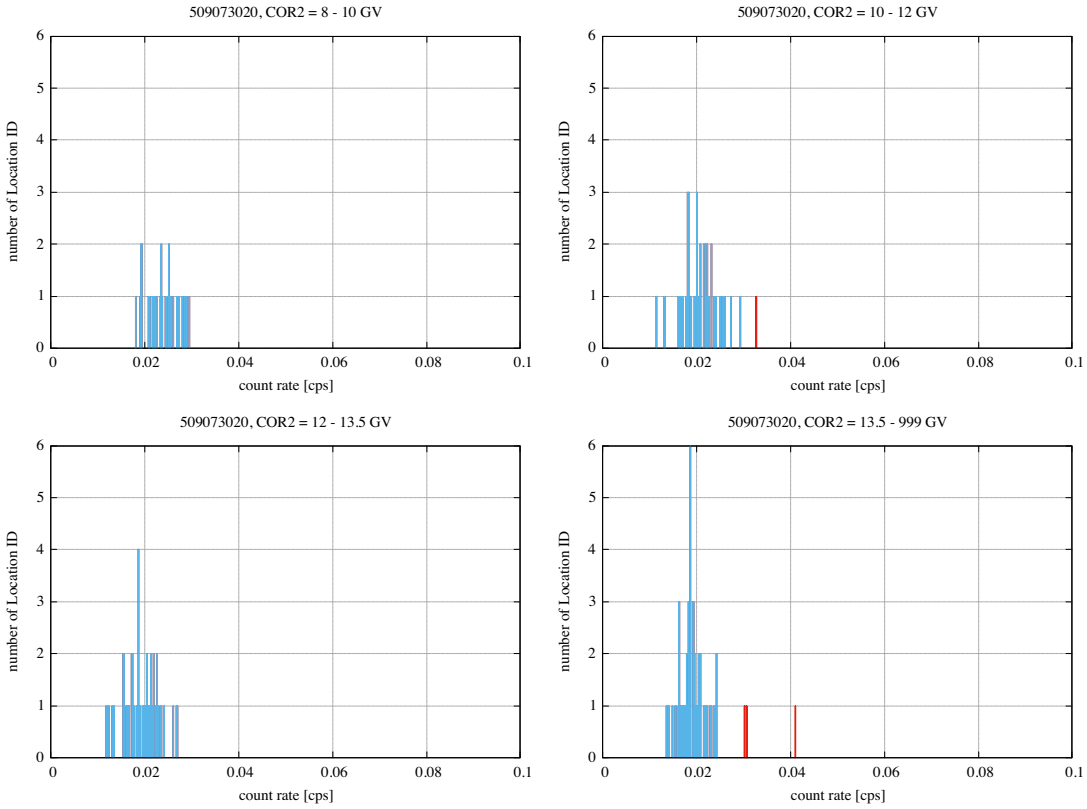

Figure B.13 Same as Figure B.2 but for the ObsID of 509073020

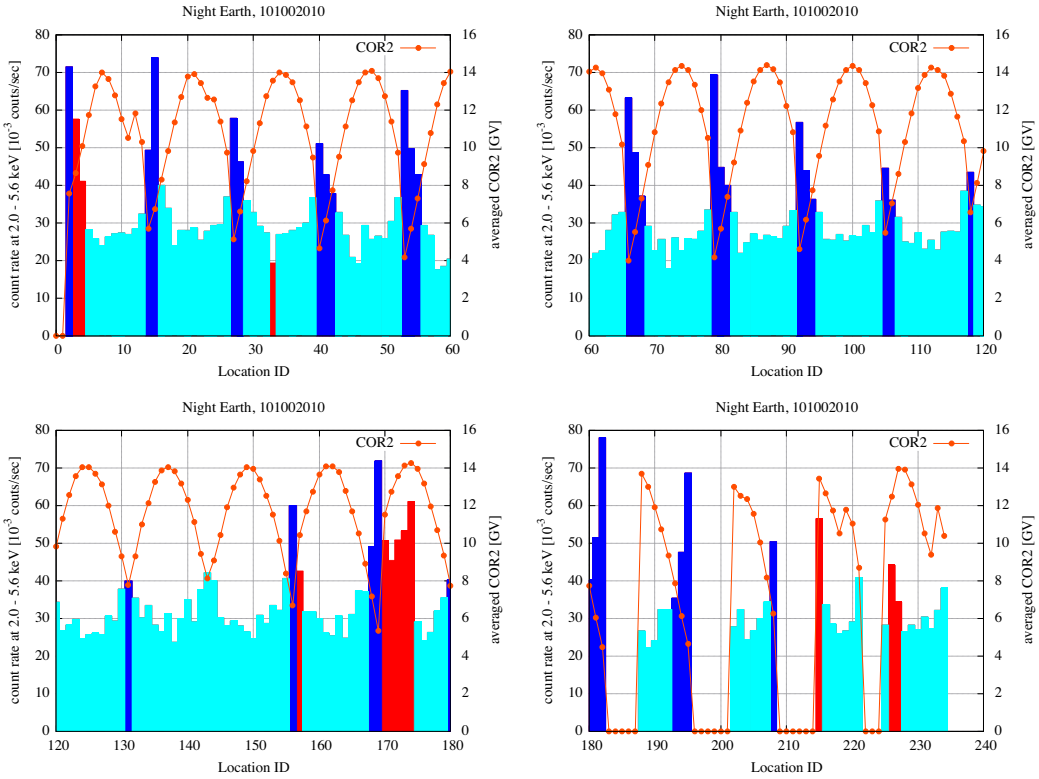

Figure B.14 Count rate of Non X-ray background between 2 and 5.6 keV (left axis) during the XIS FoV was osculated by the night Earth as a function of COR. The time-averaged COR at each location ID is also plotted (right axis). *BLUE*: the region of standard data screening. *RED*: the region of updating data rejection by location ID.

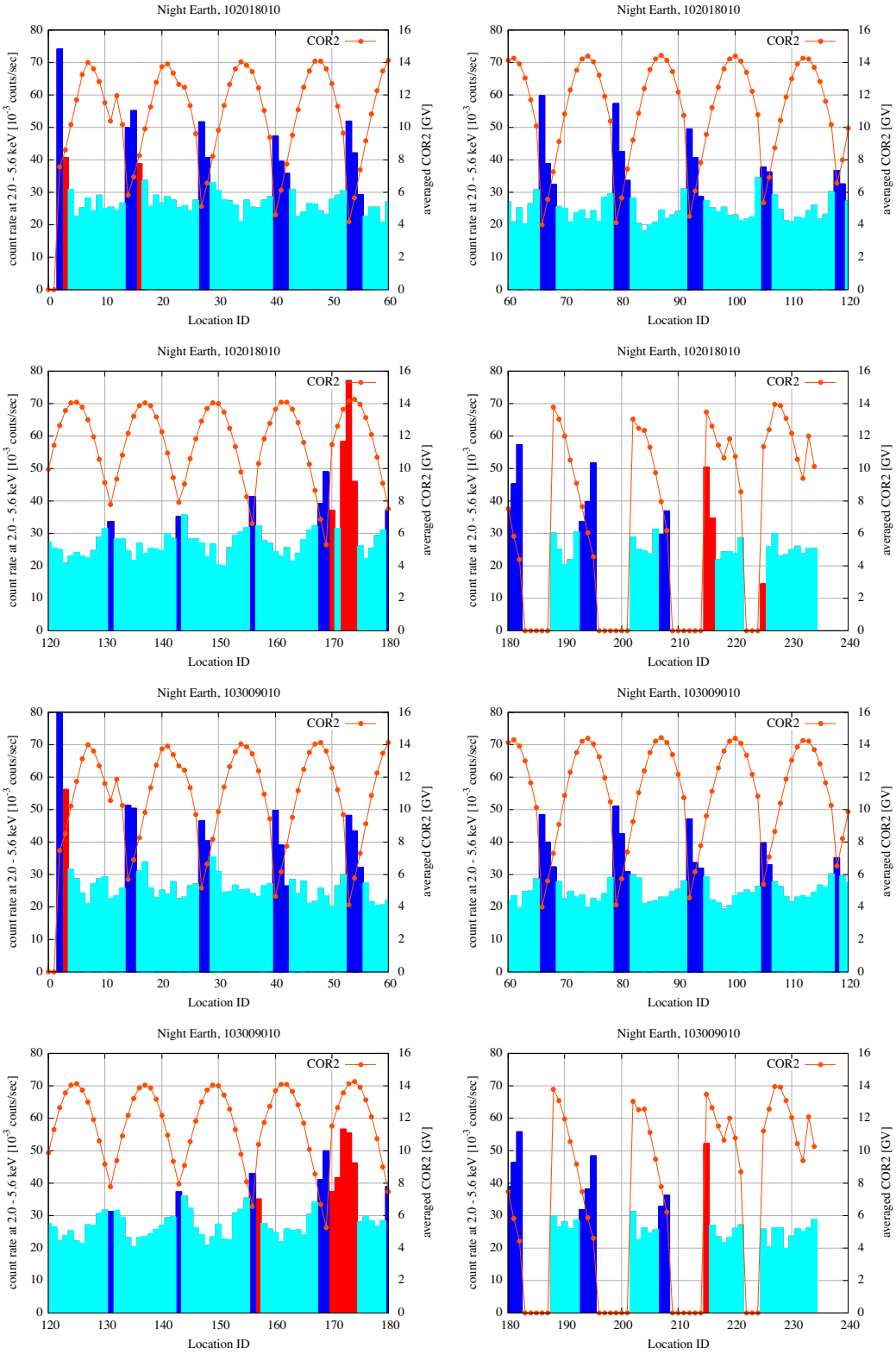

Figure B.15 Same as Figure B.14 but for the ObsID of 102018010 and 103009010

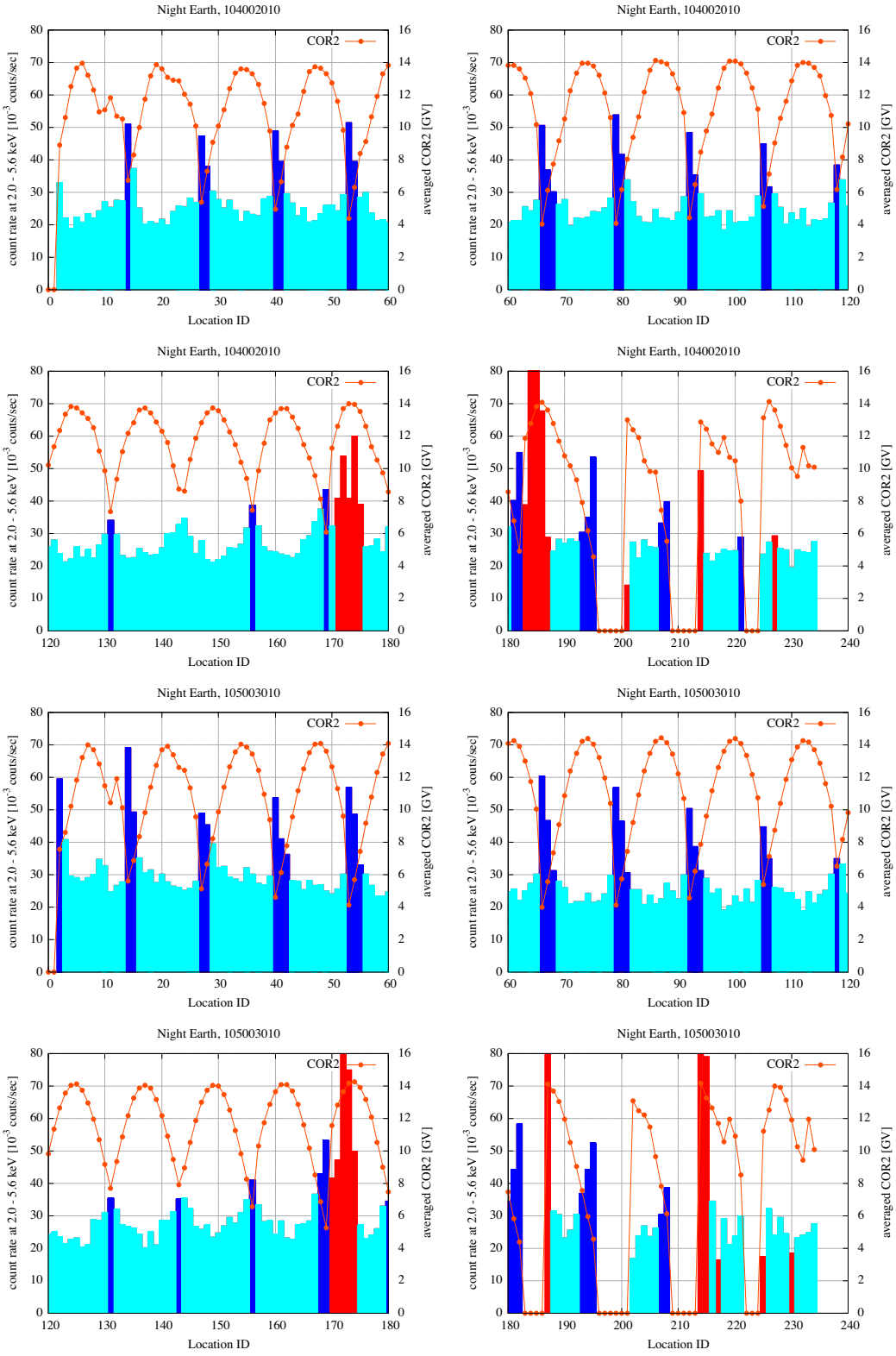

Figure B.16 Same as Figure B.14 but for the ObsID of 104002010 and 105003010

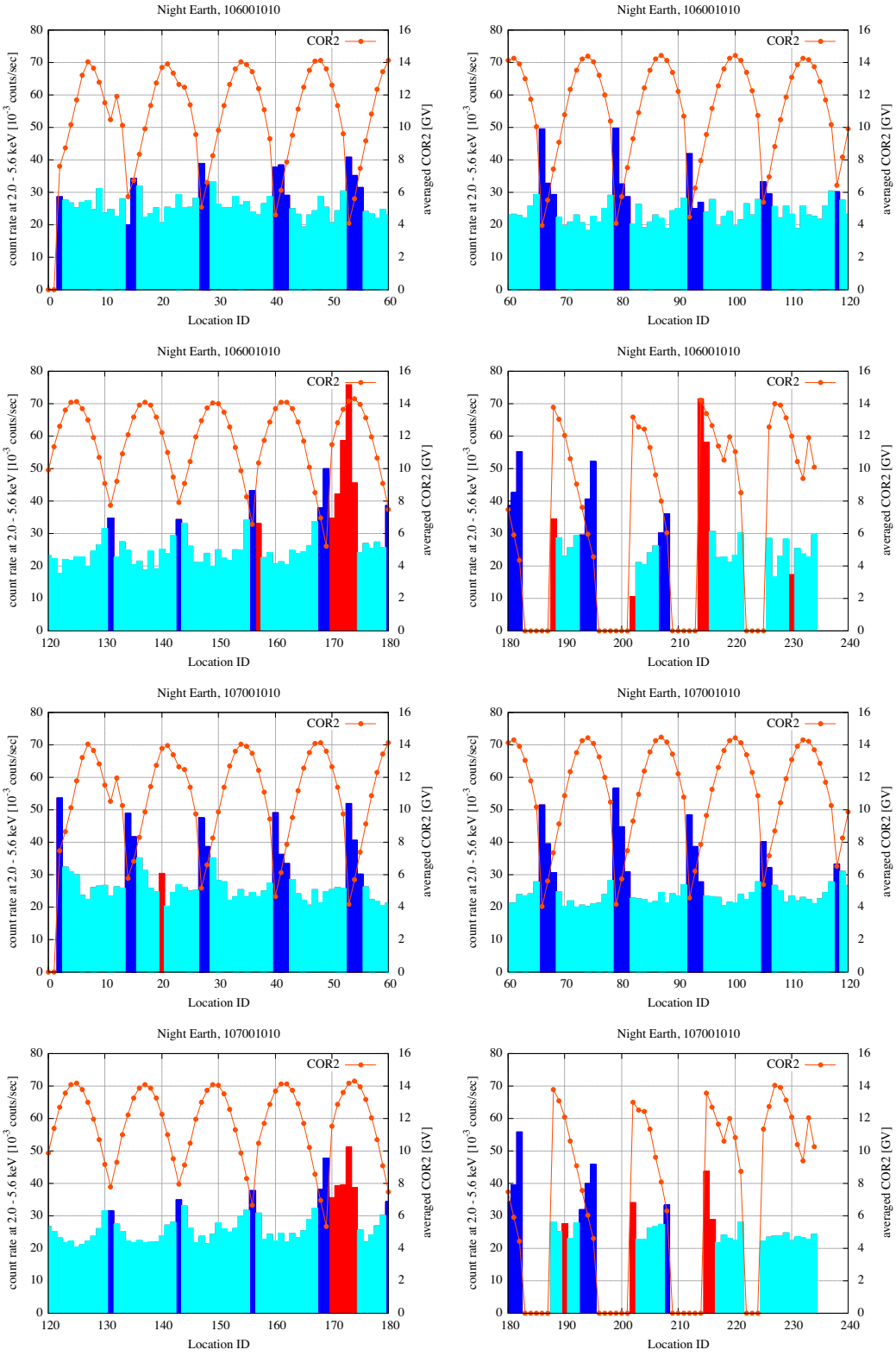

Figure B.17 Same as Figure B.14 but for the ObsID of 106001010 and 107001010

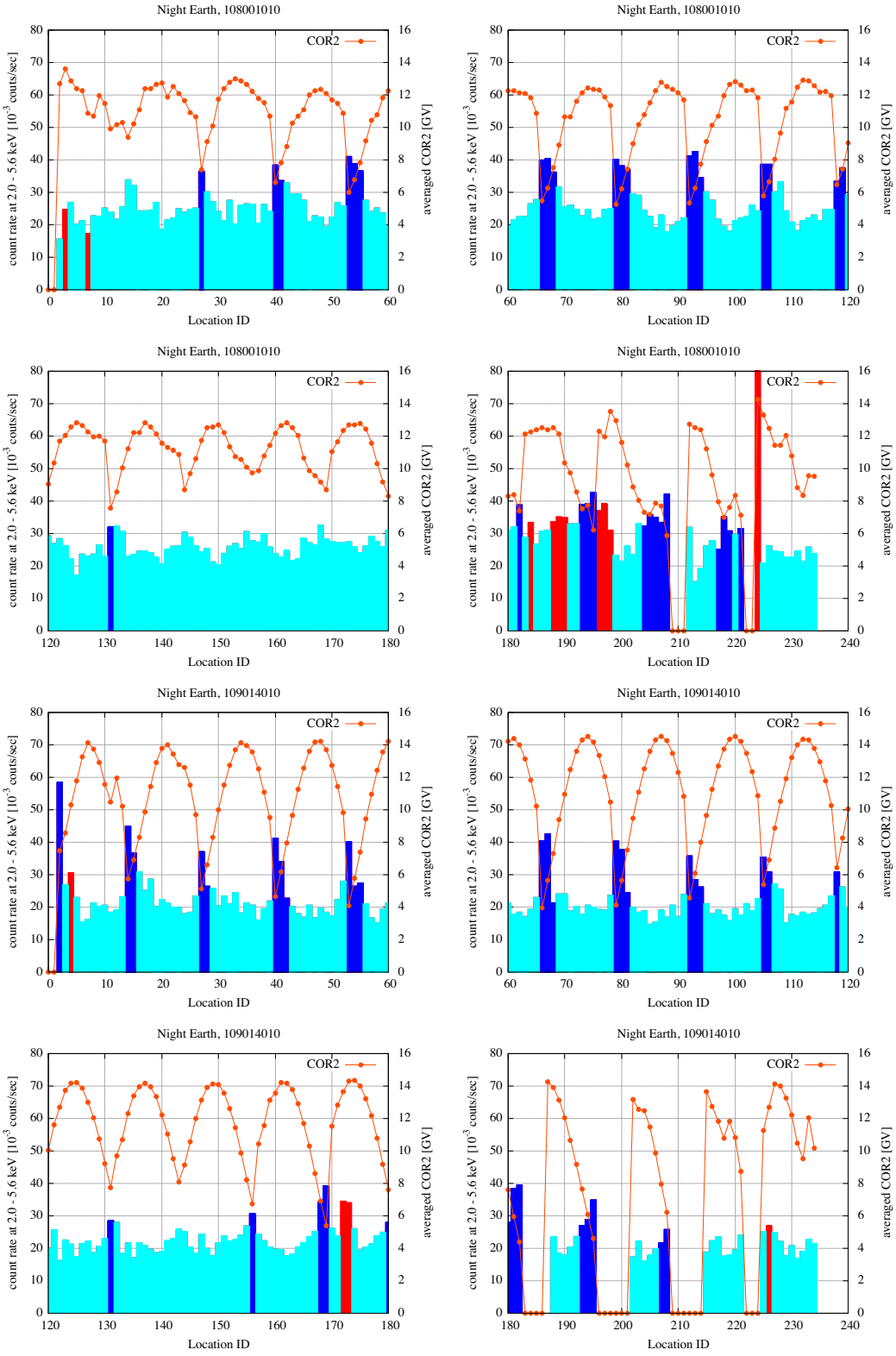

Figure B.18 Same as Figure B.14 but for the ObsID of 108001010 and 109014010

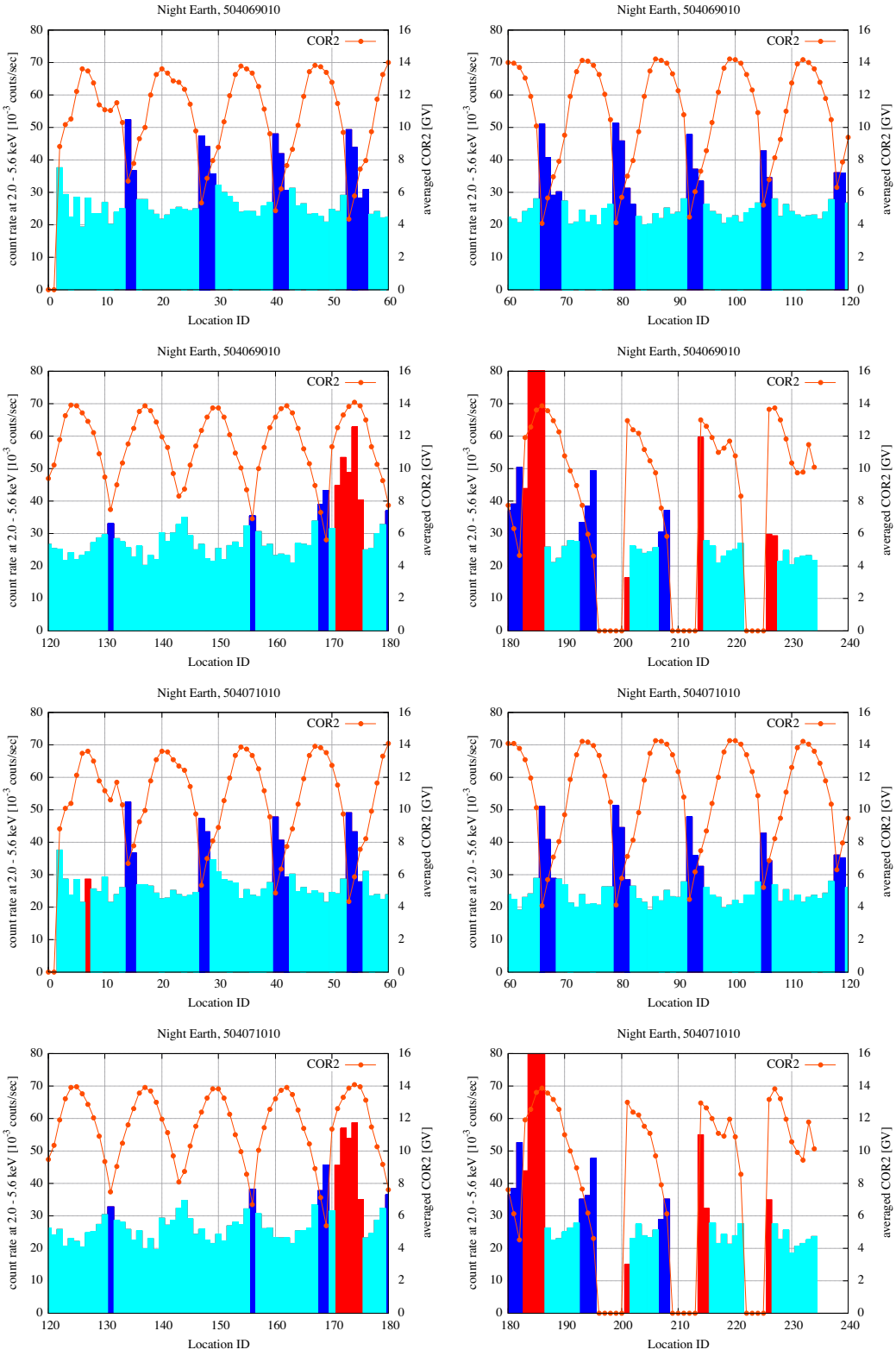

Figure B.19 Same as Figure B.14 but for the ObsID of 504069010 abd 504071010

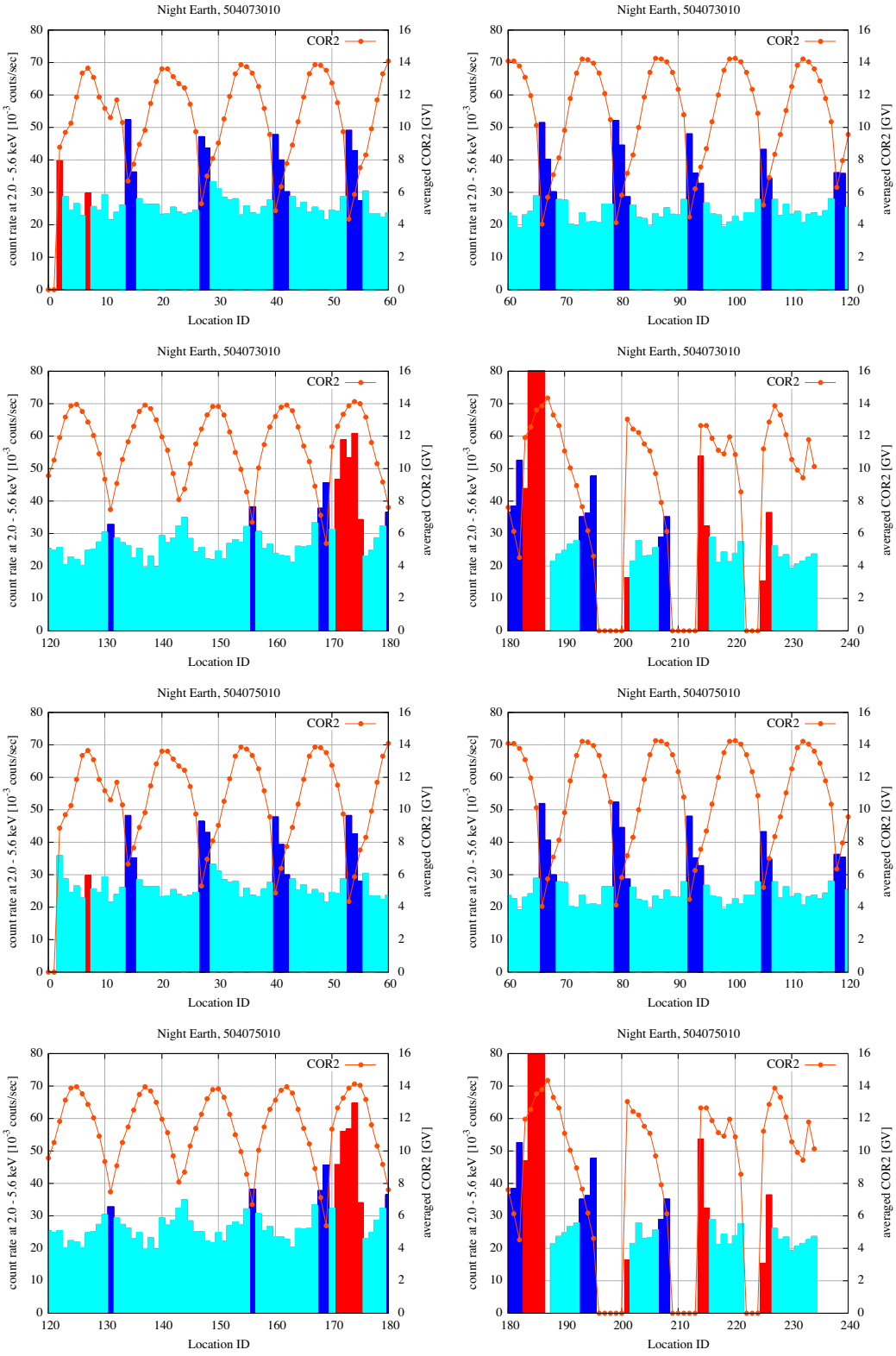

Figure B.20 Same as Figure B.14 but for the ObsID of 504073010 and 504075010

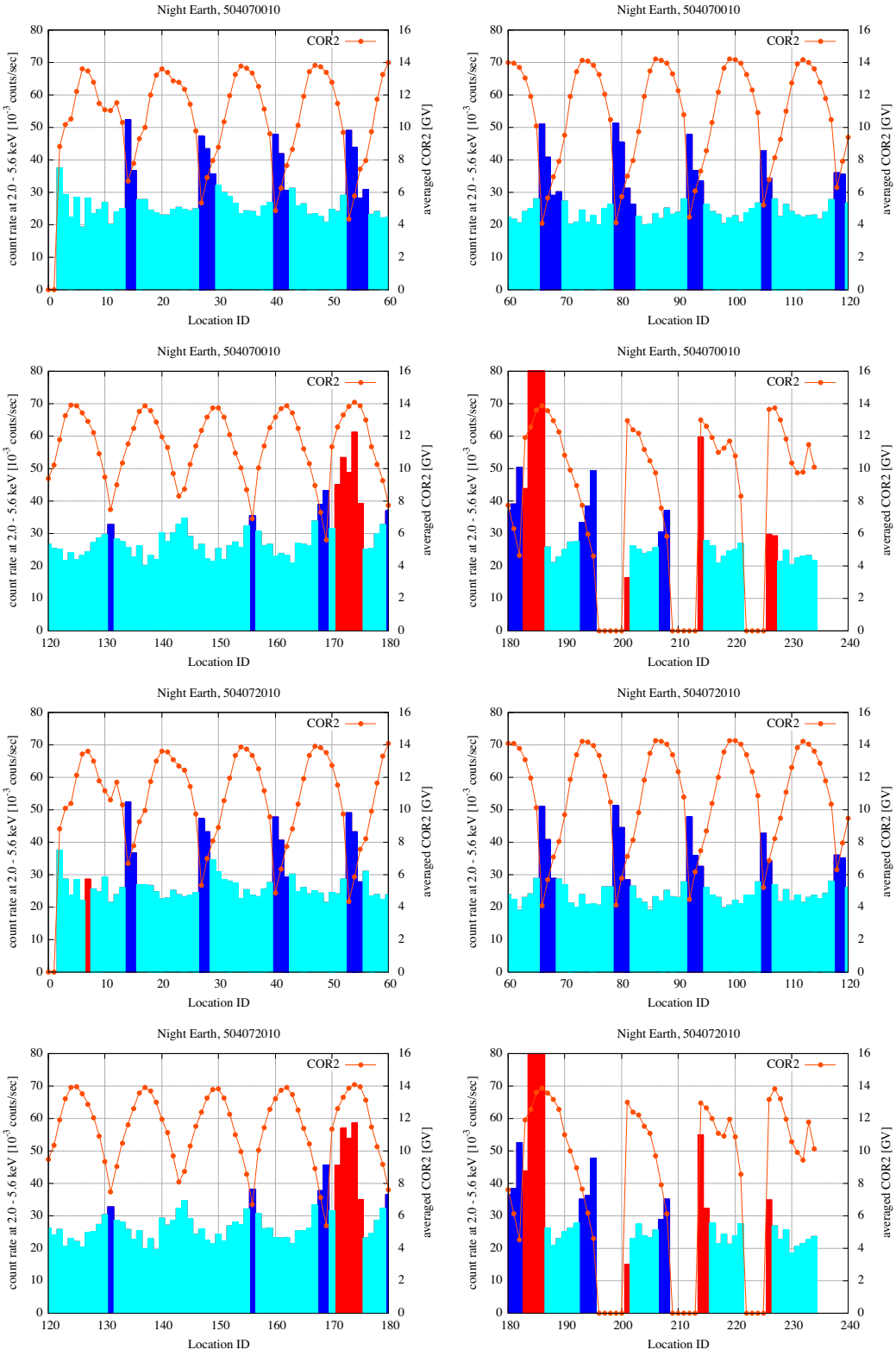

Figure B.21 Same as Figure B.14 but for the ObsID of 504070010 and 504072010

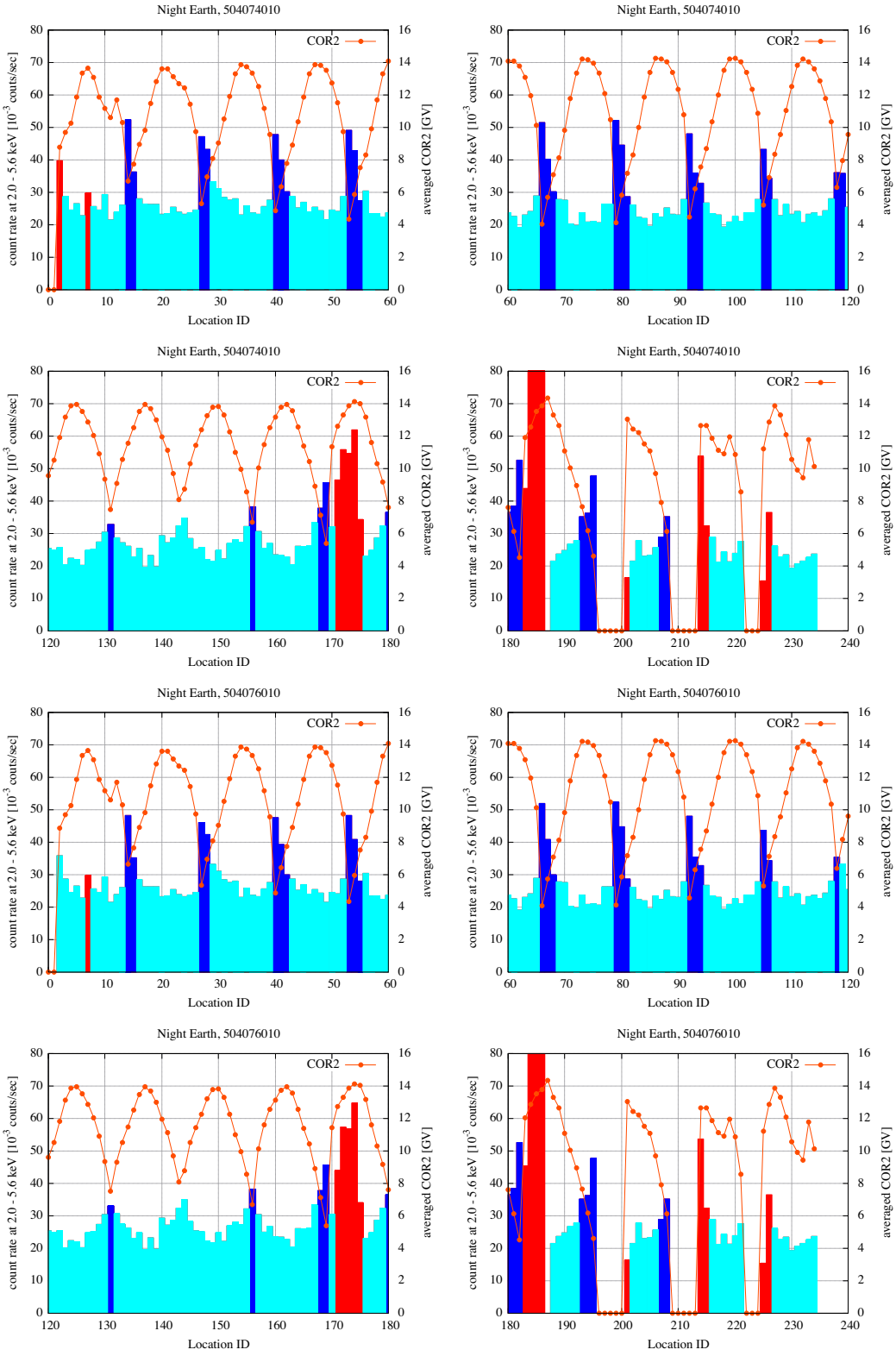

Figure B.22 Same as Figure B.14 but for the ObsID of 504074010 and 504076010

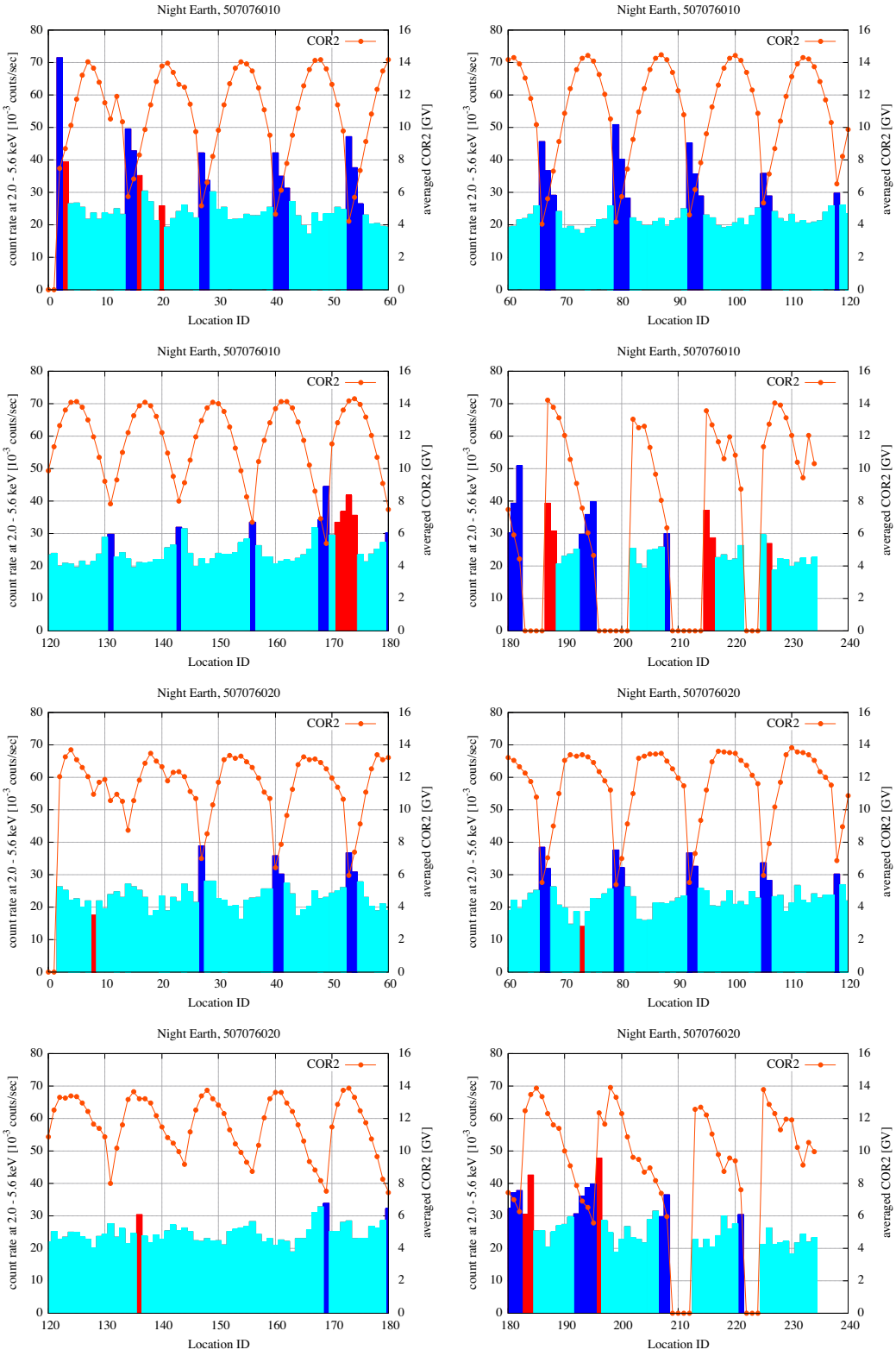

Figure B.23 Same as Figure B.14 but for the ObsID of 507076010 and 507076020

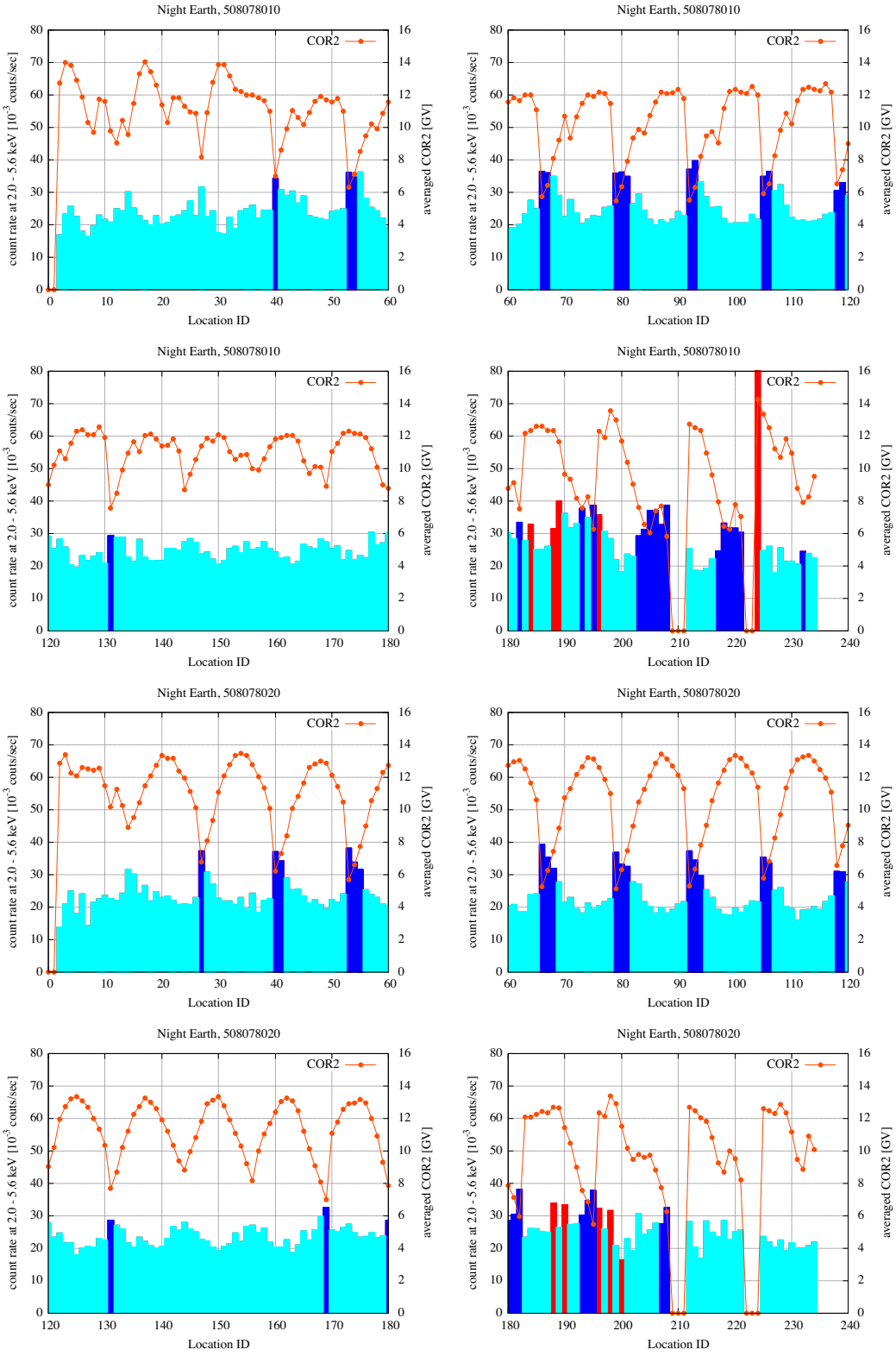

Figure B.24 Same as Figure B.14 but for the ObsID of 508078010 and 508078020

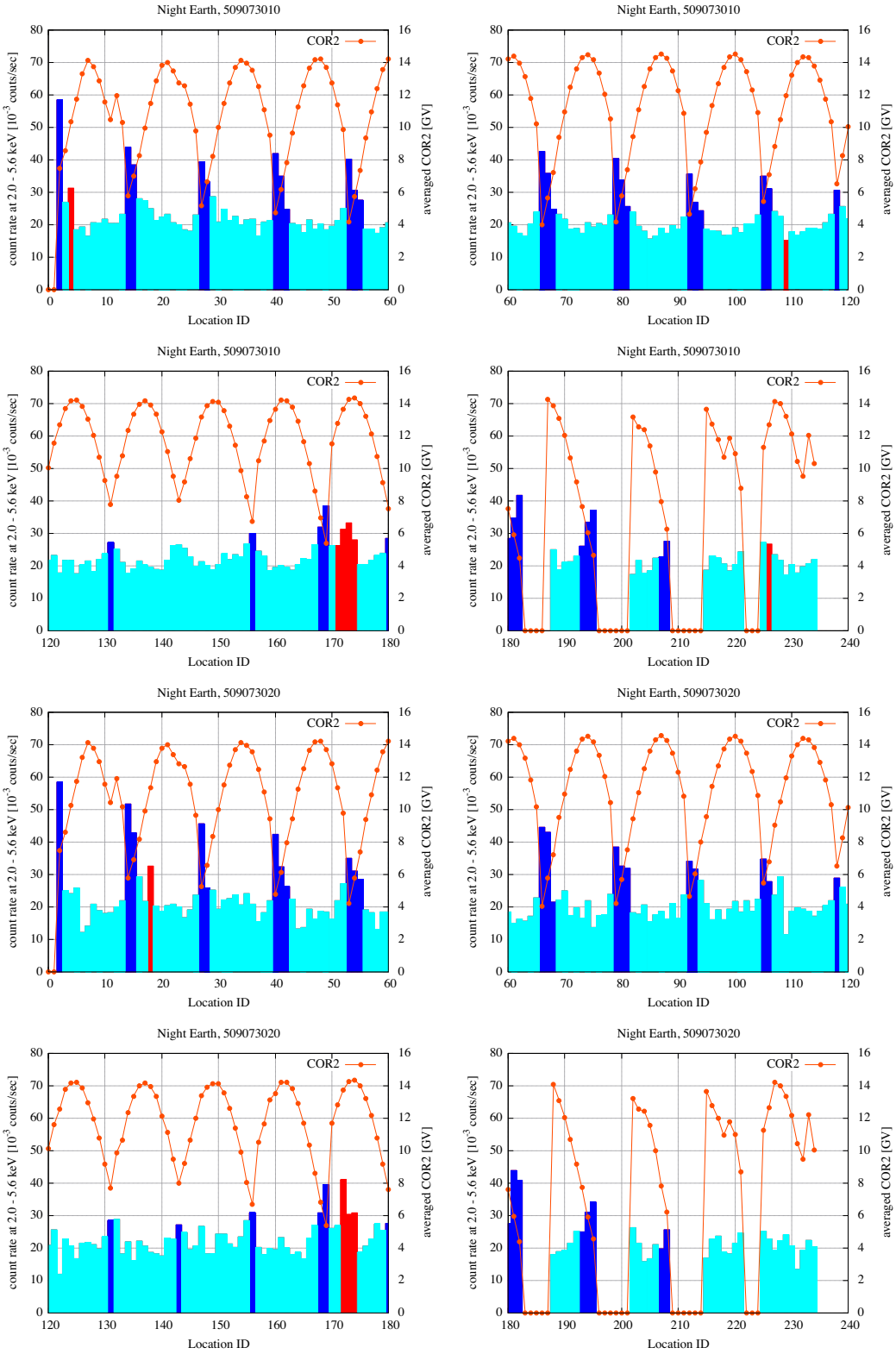

Figure B.25 Same as Figure B.14 but for the ObsID of 509073010 and 509073020

B.2 NXB distribution of each ObsID in this thesis

The results of the distribution are shown in Figure B.26-B.34. This calculation method is described in Section 5.4.2.

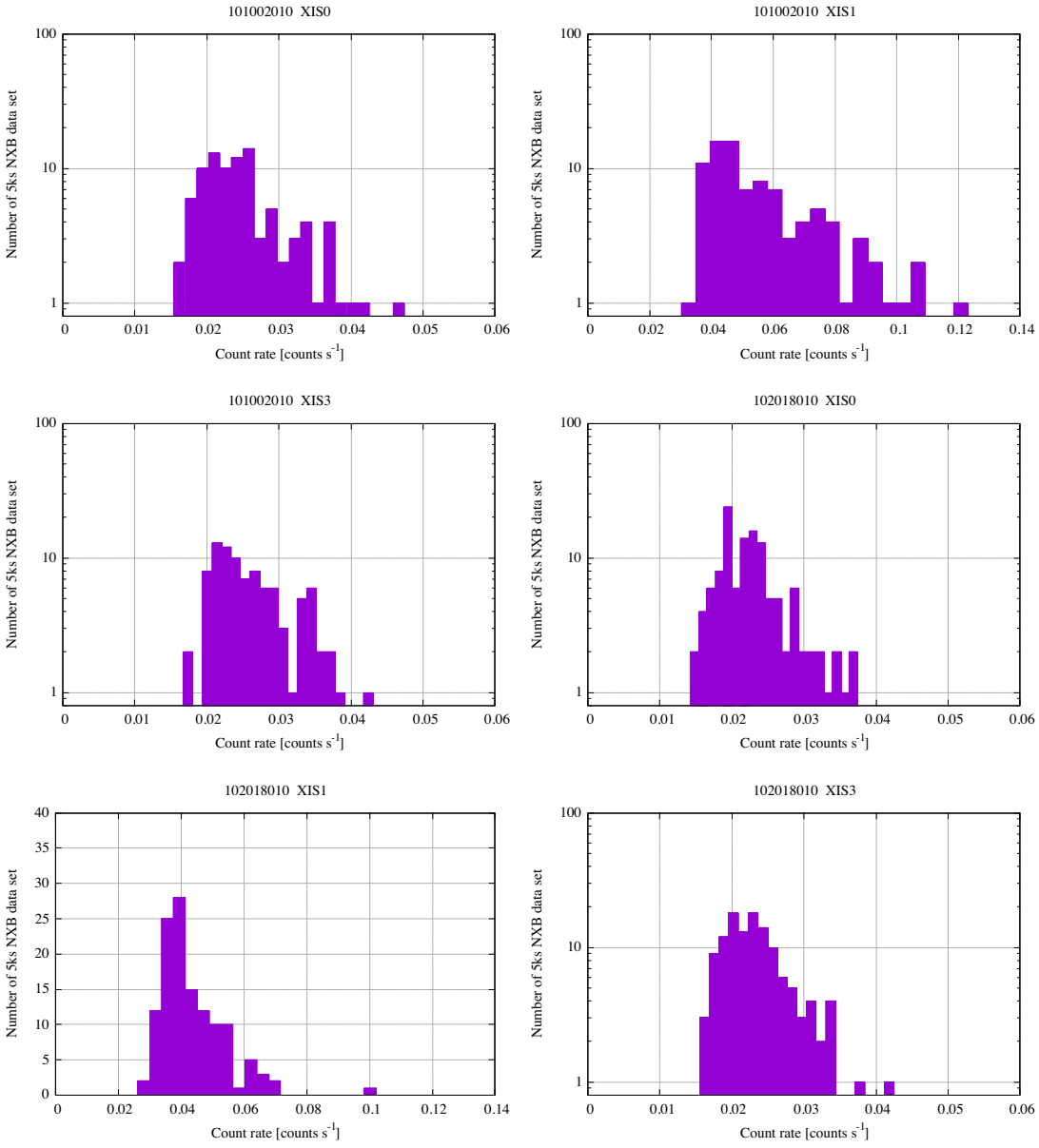

Figure B.26 The histogram of NXB count rate for 5 ks exposure time in the 2.0-5.6 keV

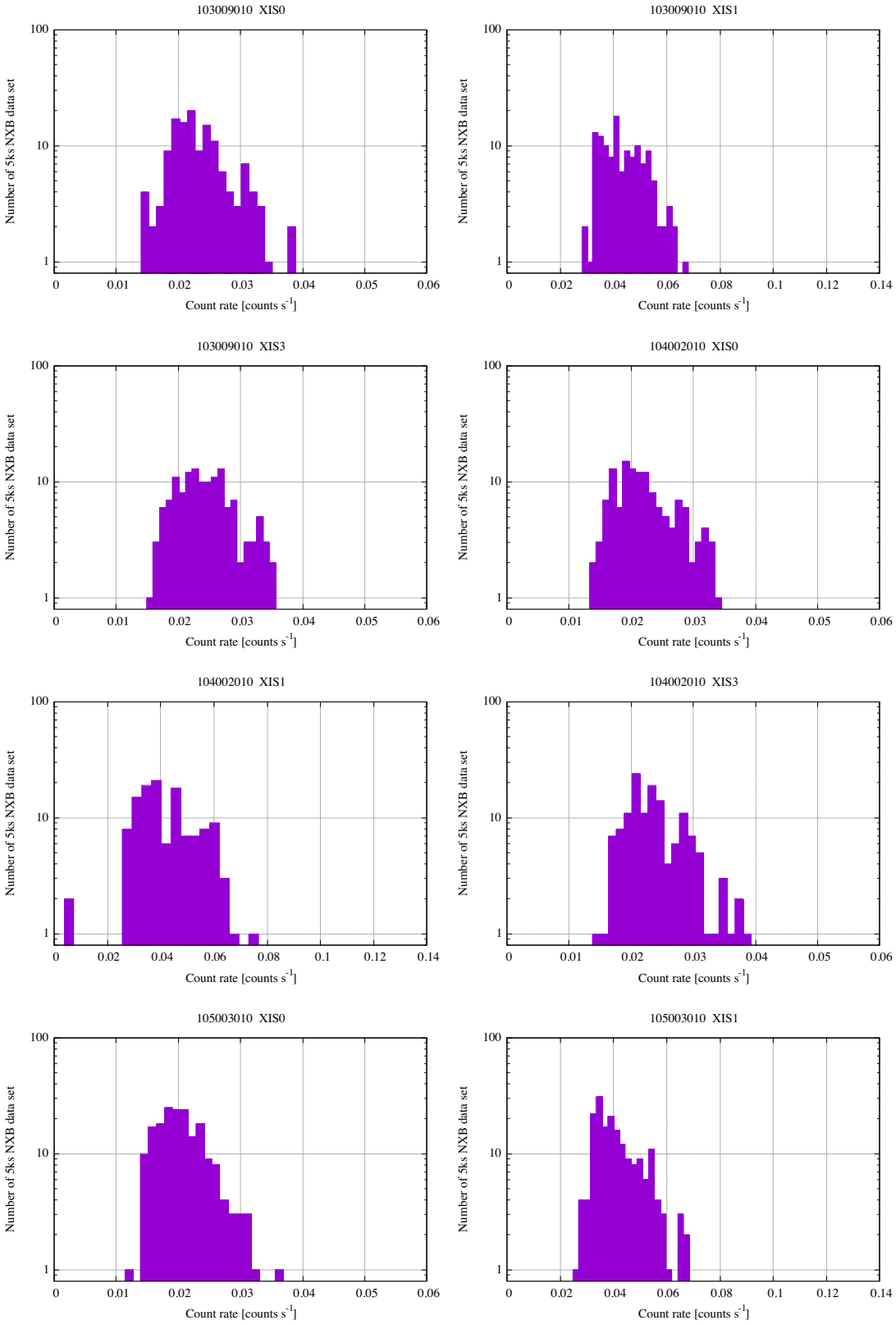

Figure B.27 Same as Figure B.26 but for the ObsID of 103009010, 104002010 and 105003010

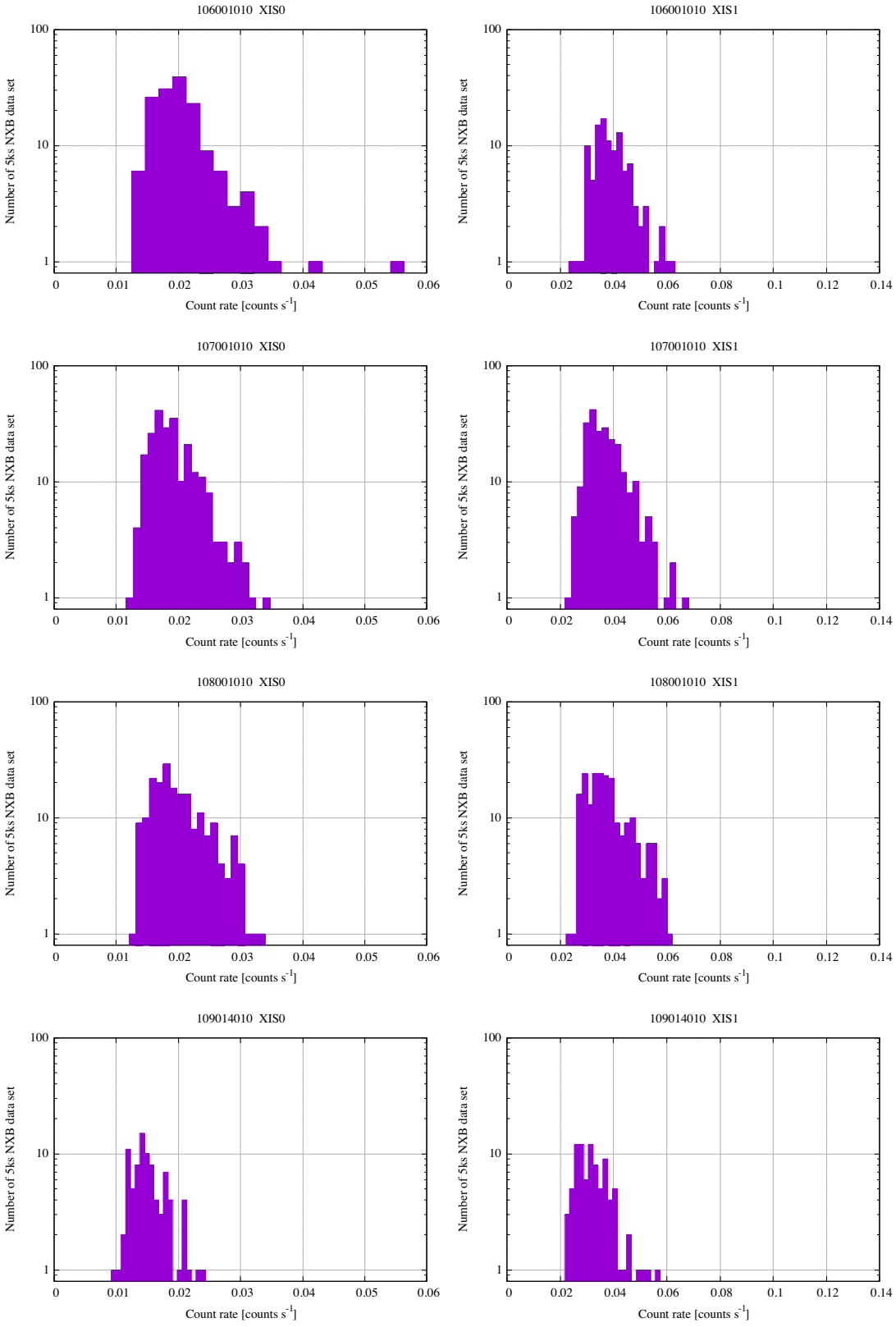

Figure B.28 Same as Figure B.26 but for the ObsID of 105003010, 106001010, 107001010, 108001010 and 109014010

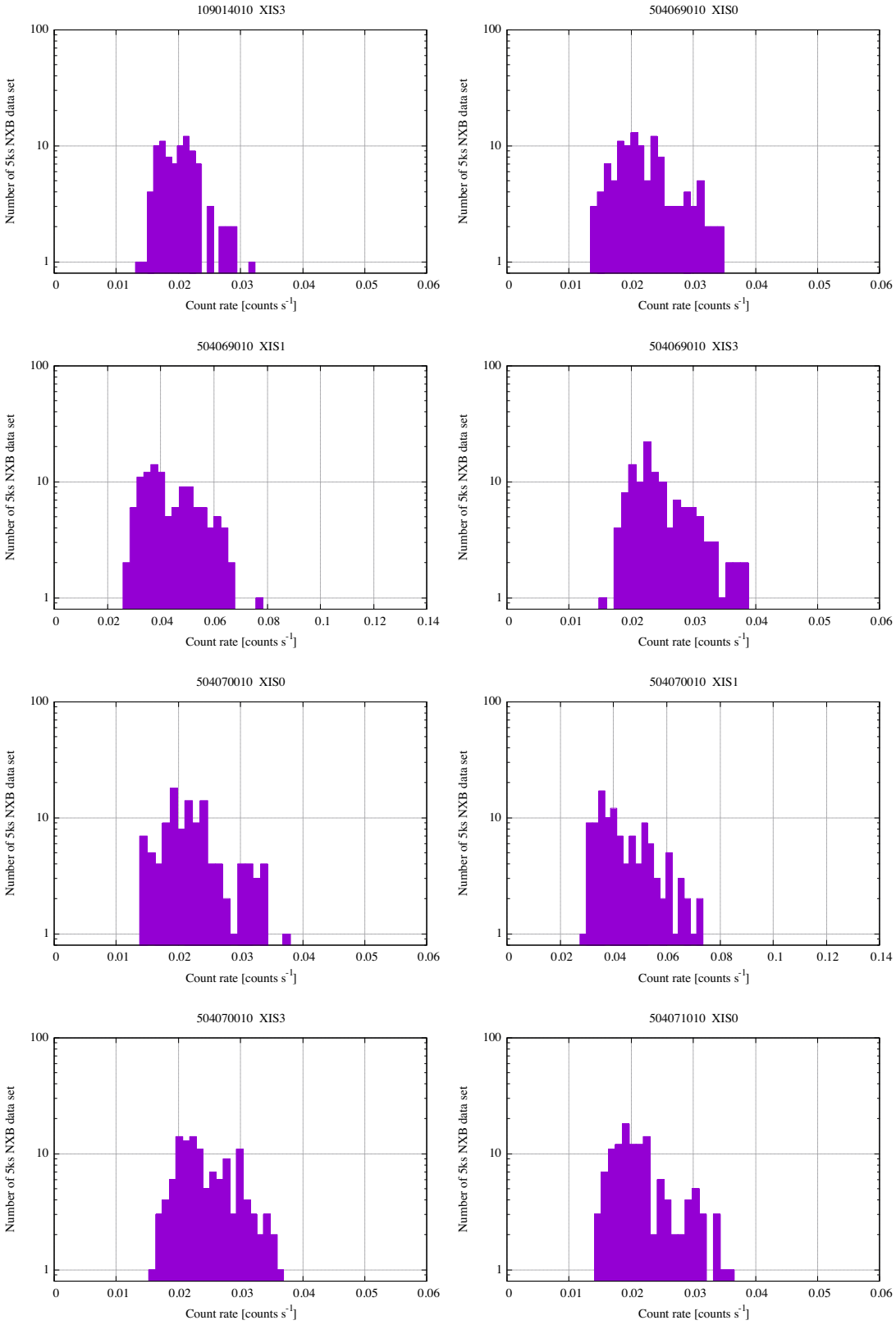

Figure B.29 Same as Figure B.26 but for the ObsID of 109014010, 504069010 and 504071010

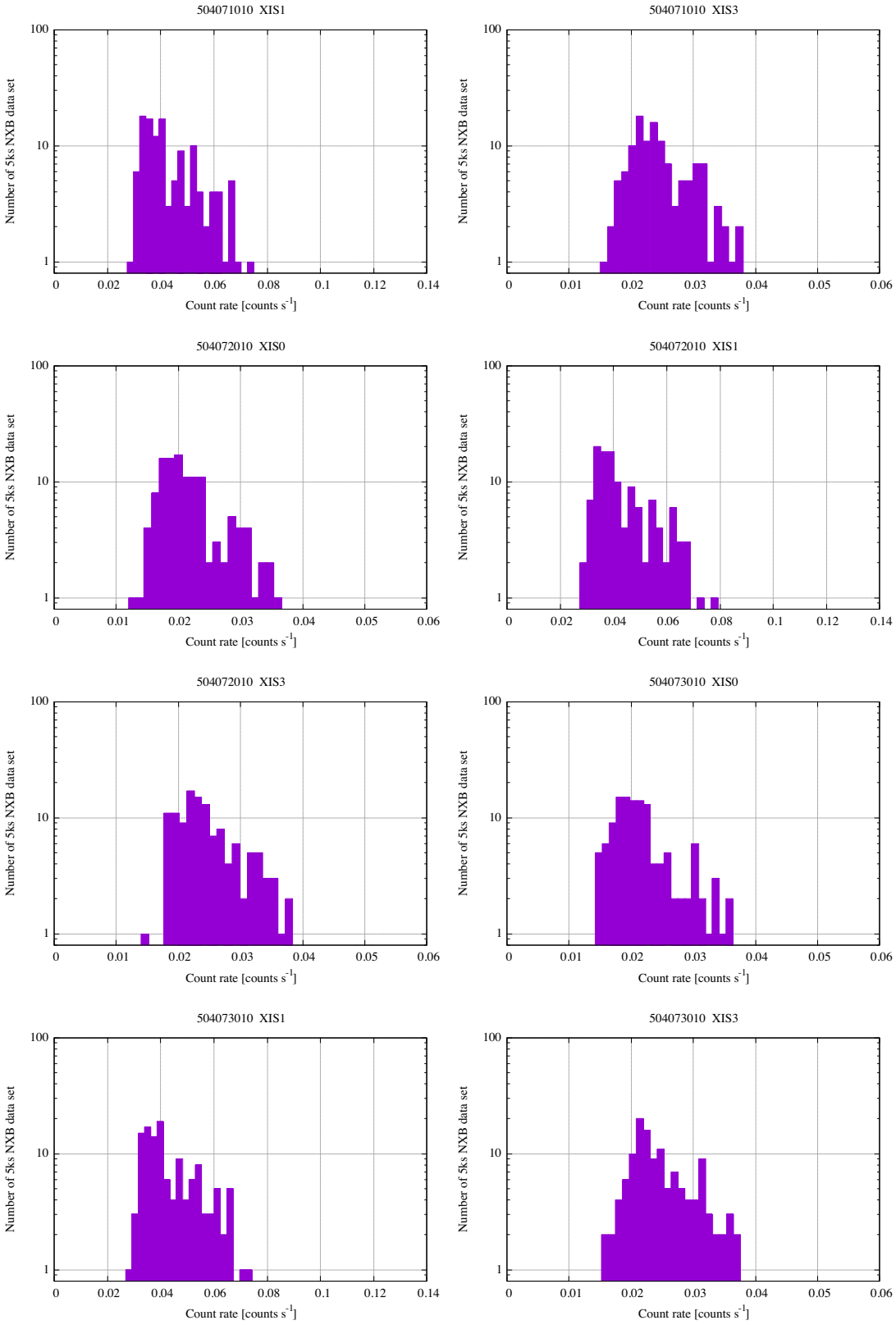

Figure B.30 Same as Figure B.26 but for the ObsID of 504071010, 504072010 and 504073010

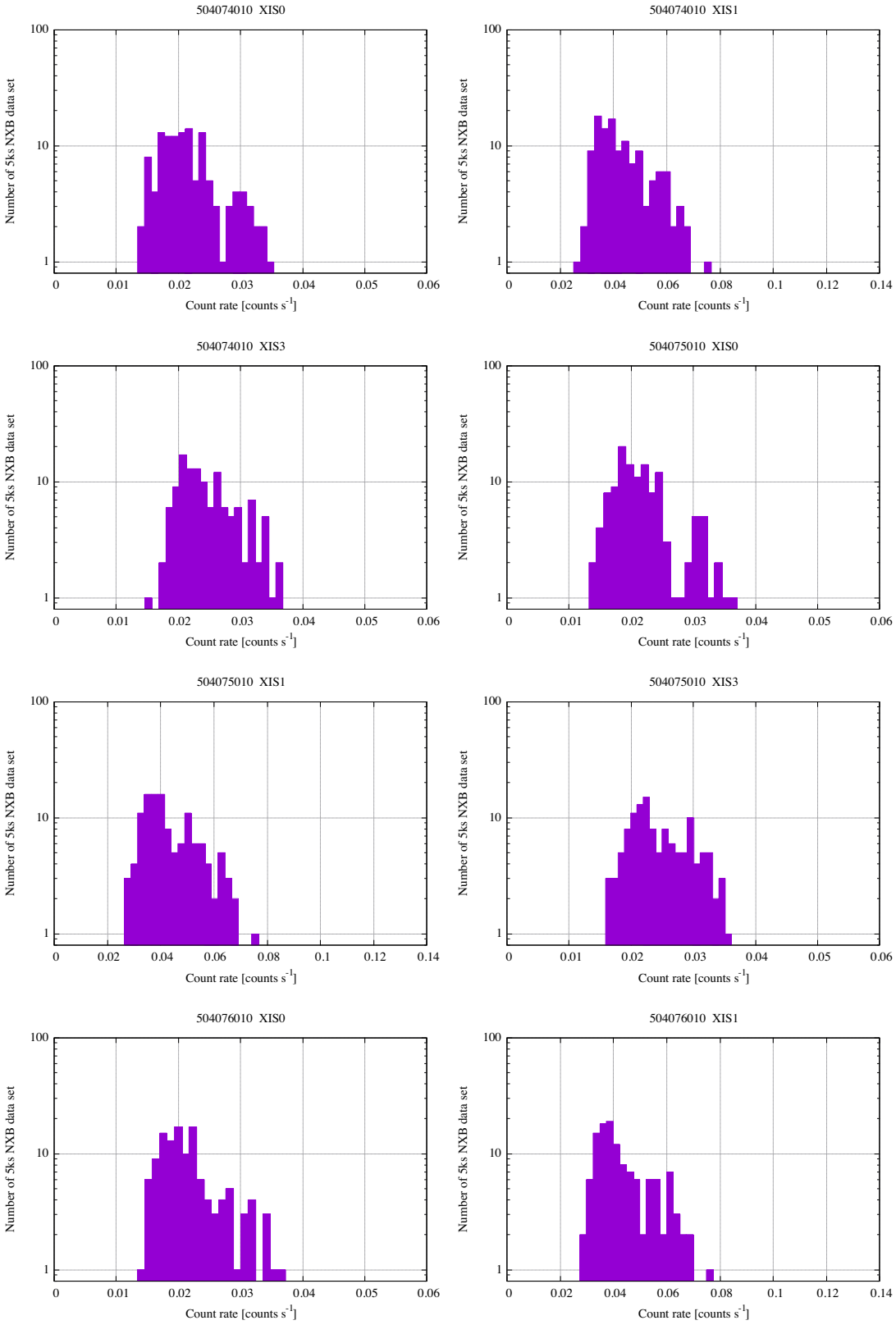

Figure B.31 Same as Figure B.26 but for the ObsID of 504074010, 504075010 and 504076010

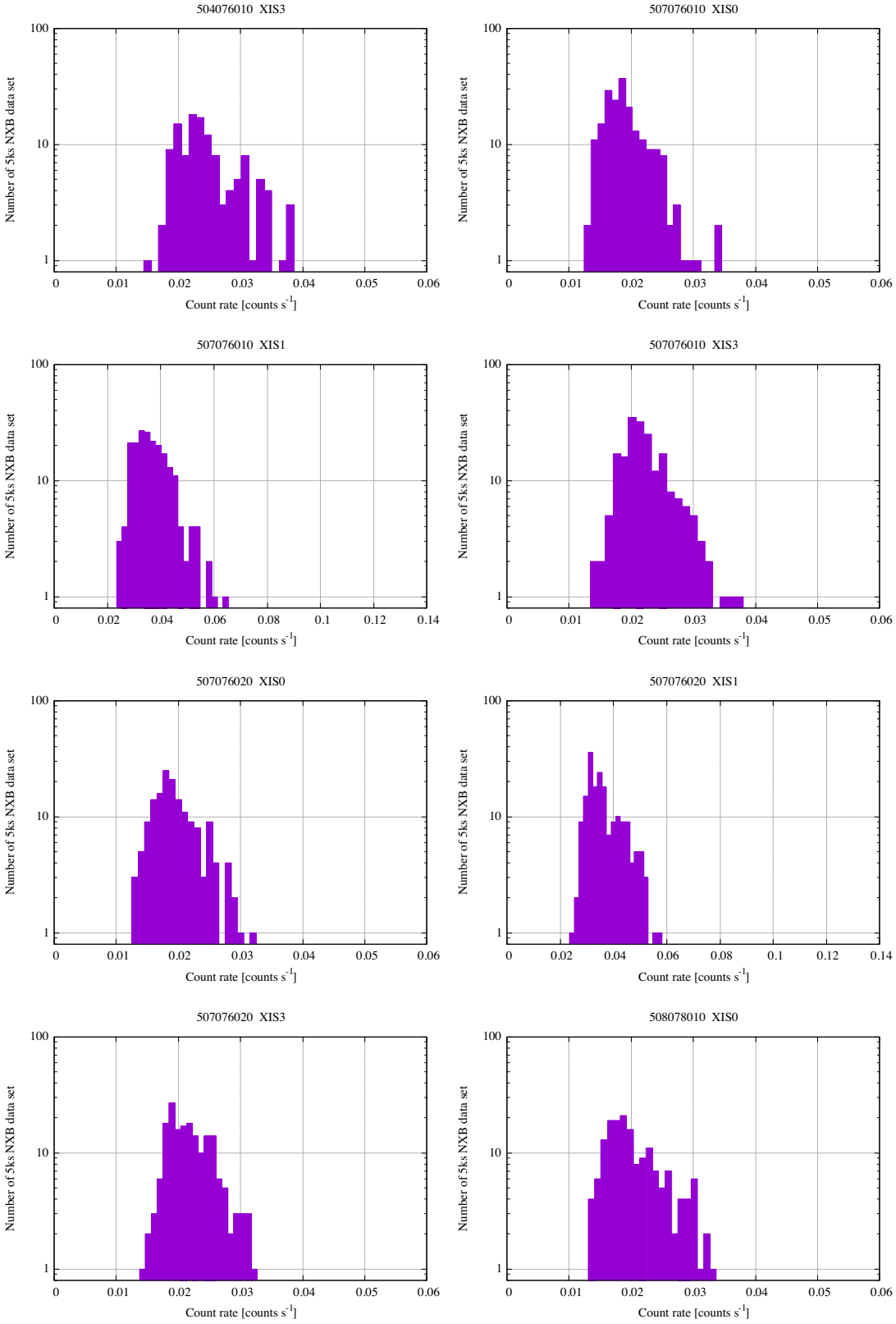

Figure B.32 Same as Figure B.26 but for the ObsID of 504076010, 507076010, 507076020 and 508078010

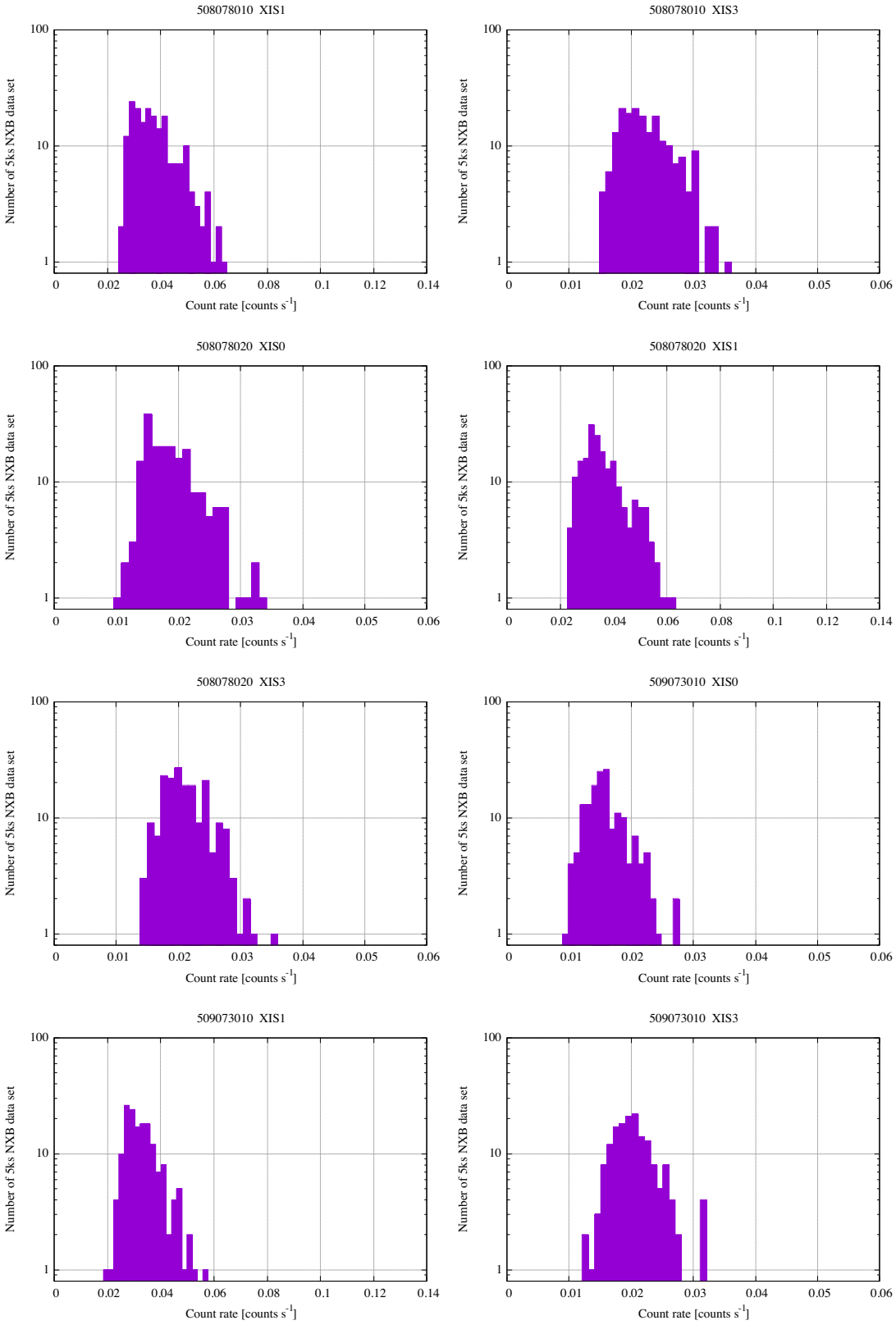

Figure B.33 Same as Figure B.26 but for the ObsID of 508078010, 508078020, 509073010

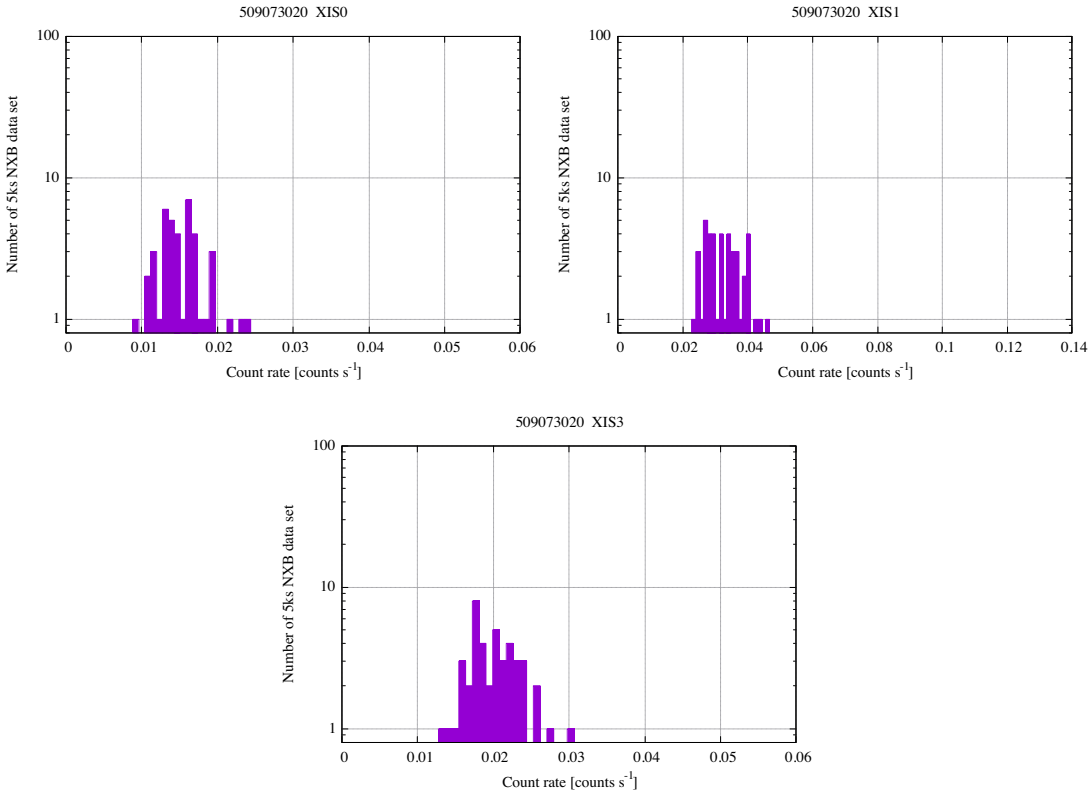

Figure B.34 Same as Figure B.26 but for the ObsID of 509073020

B.3 The position of *Suzaku* for each $B_{\perp}L$ class

The Earth's locations of *Suzaku*satellite for each $B_{\perp}L$ class summarized in Table 5.1 are shown in Figure B.35-B.37.

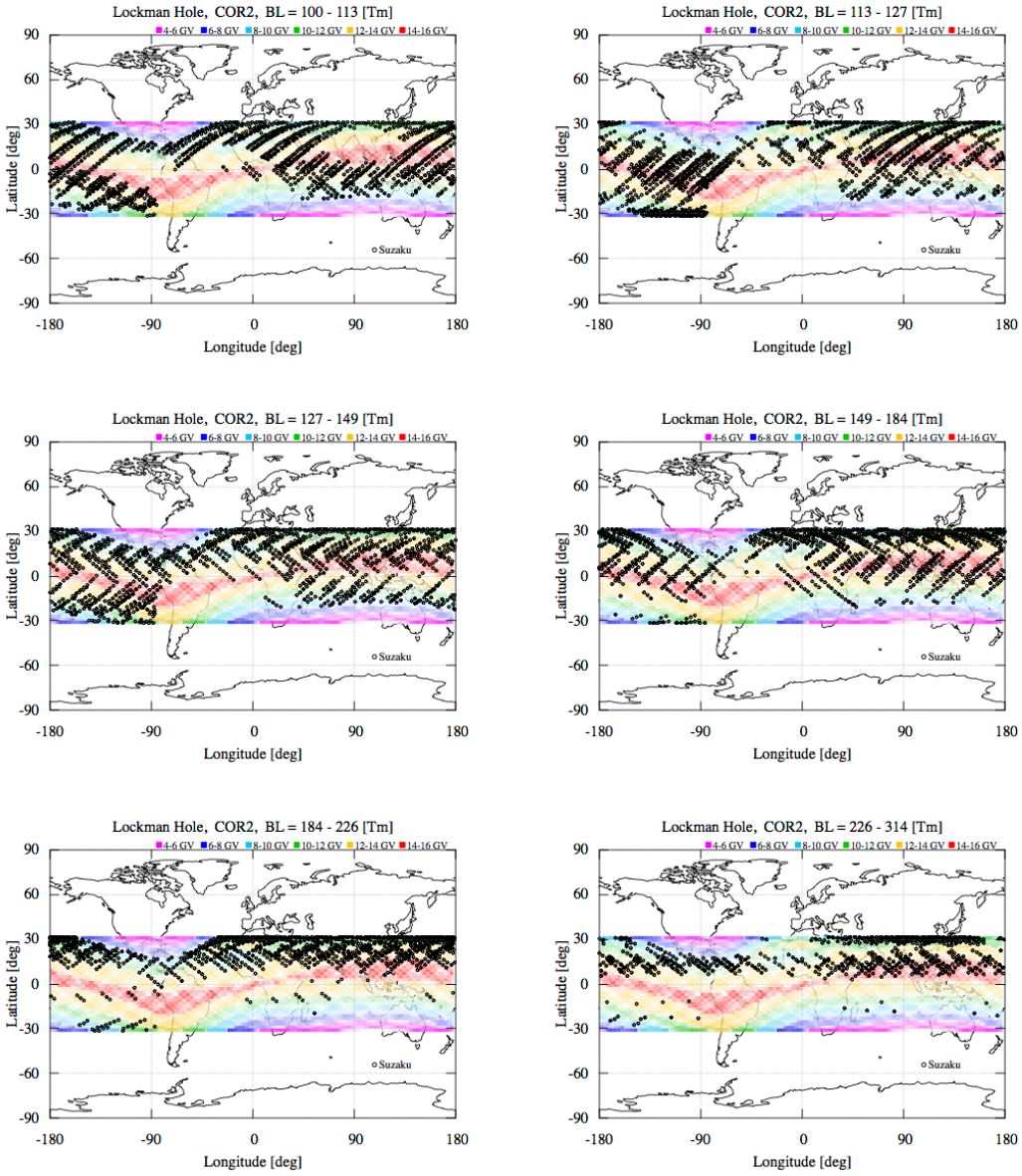

Figure B.35 The *Suzaku* location and COR value for each $B_{\perp}L$ class in Lockman hole observation.

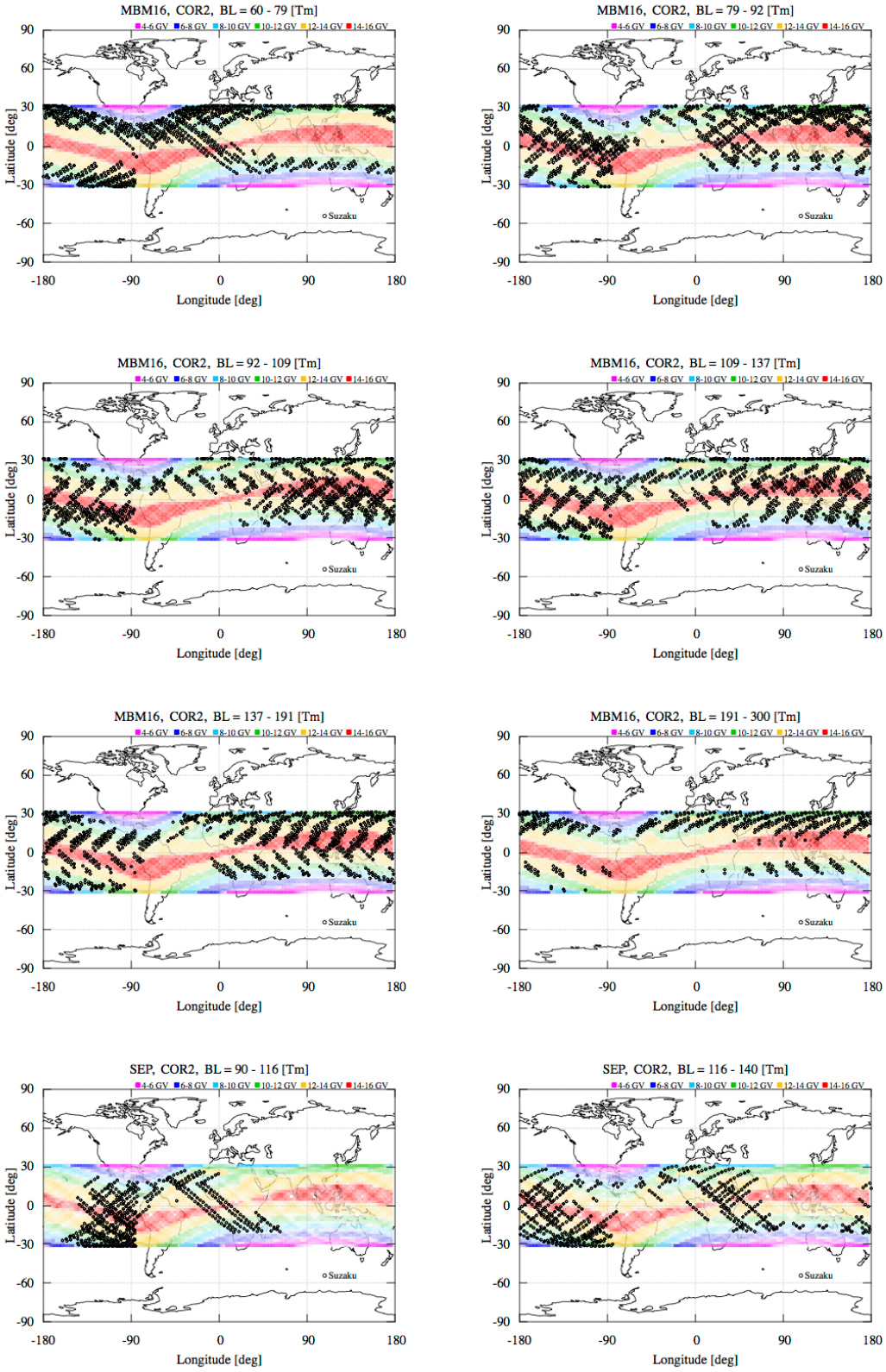

Figure B.36 Same as Figure B.35 but for MBM16 and SEP observations

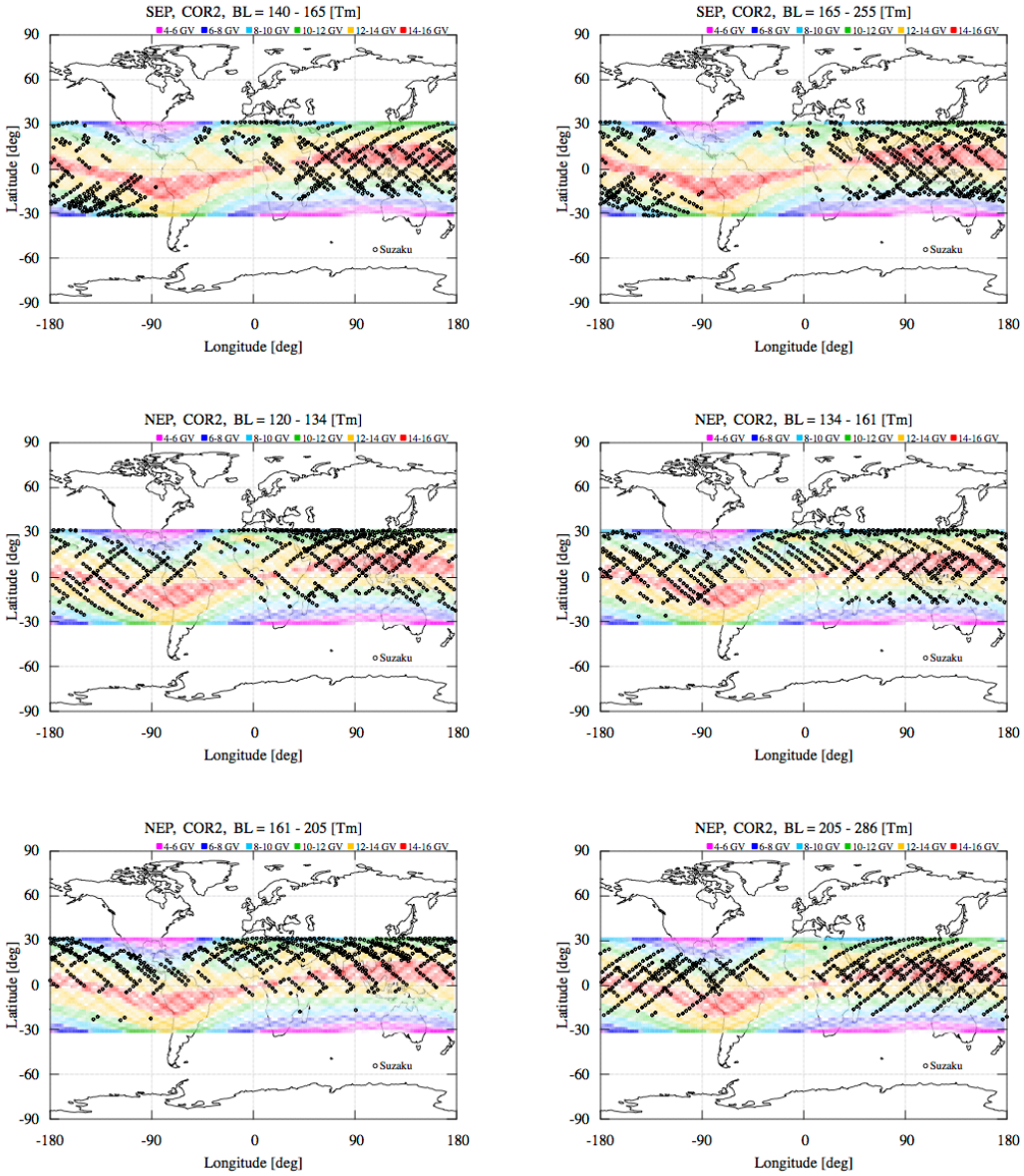

Figure B.37 Same as Figure B.35 but for SEP and NEP observations

C Details of analysis tools

C.1 Ftools in HEAsoft

The observational data of the *Suzaku* satellite were provided in the astronomical standard format known as the Flexible Image Transport System (FITS). *Suzaku* data manipulation were performed using the HEAsoft package called Ftool (http://heasarc.gsfc.nasa.gov/docs/software/lheasoft/).

`cleansis`

The `cleansis` removes hot and flickering pixels based on a Poissonian analysis. This was originally written for the CCD of *ASCA* data and can also work on *Suzaku* data.

`xisrmfgen`

The `xisrmfgen` generates that redistribution matrix files (RMFs) of an X-ray imaging spectrometer (XIS) energy fit for a PHA file affecting the instrumental response with calibration database. This calculates a line profile of monochromatic X-rays at each energy bin.

`xissimarfgen`

The `xissimarfgen` calculates the ancillary response files (ARFs) of *Suzaku*/XIS by Monte-Carlo simulations (Ishisaki et al., 2007). The ARF files include an effective area related XRT mirror geometry and reflectively, transmission through the thermal shield and transmission of optical blocking filter contaminant. In this thesis, we assumed that the source emission is uniformly extended inside 20 arcmin from the optical axis.

`xisnxbgen`

The `xisnxbgen` estimates the non-X-ray background (NXB) spectrum and image of XIS, from the weighted summation of the night Earth observation detailed in Section 5.3. In this thesis, we selected 2 sorting parameters, which is the cut-off-rigidity (`COR2`) and location ID (`LOC_ID`).

C.2 Models in XSPEC

We used XSPEC, which is one of the Ftools used to fit emission models multiplied by the RMFs and ARFs to NXB-subtracted spectra with *Suzaku*/XIS. XSPEC contains about 100 spectral models (https://heasarc.gsfc.nasa.gov/xanadu/xspec). Here, we simply explain the spectral models used in this thesis.

apec

The Astrophysical Plasma Emission Code (*apec*) describes both lines and continuum emissivity for a hot, optically thin plasma that is in collisional ionization equilibrium (CIE, Smith et al., 2001). In this thesis, we set the metal abundance to the Solar-neighbor value (Anders & Grevesse, 1989). The normalization of *apec*, which is the of the emission measure along the line-of-sight is,

$$\mathrm{Norm}_{apec} = \frac{10^{-14}}{4\pi D_A^2 \left(1+z\right)^2} \int n_e n_H dV \quad [\mathrm{cm}^{-5}], \tag{C.1}$$

where D_A is the angular diameter distance to the source and n_e, n_H are the electron and hydrogen densities.

power-law

The *power-law* is a simple photon power law, $f\left(E\right) = SE^{-\Gamma}$, where Γ is photon index and S is normalization in unit of photons keV^{-1} cm^{-2} s^{-1} at 1 keV.

phabs

The *phabs* model is the photoelectric absorption by interstellar medium, $M\left(E\right) = \exp\left(-n_H \sigma\left(E\right)\right)$, where n_H is equivalent hydrogen column in units of 10^{22} atoms cm^{-2} and $\sigma\left(E\right)$ is the photo-electric cross-section.

D Details of spectral fitting results

In this thesis, we analyzed the four observational directions of *Suzaku*/XIS. The spectral fitting results as shown in Figure D.1 and D.2 of the four data sets were summarized in Table 5.6, D.1 and D.2. The fitting process is described in Section 5.6.1. We also evaluated the XDB + ALP model, including NXB fluctuation as summarized in Table 5.7, 5.8 and D.3. In conclusions, we obtained the upper limit of ALP surface brightness in Table 5.9 estimated from confidence contours as shown in Figure 5.25 and 5.26.

Table D.1 Summary of parameters of the XDB model by spectral fitting in MBM16 observation.

Parameter	Summed(χ^2)[¶]	Summed(C)[‖]	$(B_\perp L)^2$ sort(C)[‖††]
$n_{\rm H}$[*] (10^{20} cm^{-2})	16.90(fix)	16.90(fix)	16.90(fix)
Norm$_1$[†]	0(fix)	0(fix)	0(fix)
kT_2 (keV)	$0.30^{+0.11}_{-0.06}$	$0.33^{+0.01}_{-0.01}$	$0.32^{+0.01}_{-0.01}$
Norm$_2$[†]	$2.1^{+1.7}_{-0.8}$	$2.0^{+0.1}_{-0.1}$	$2.0^{+0.2}_{-0.1}$
$\Gamma_{\rm CXB}$[‡]	$1.25^{+0.02}_{-0.02}$	$1.24^{+0.01}_{-0.01}$	$1.24^{+0.01}_{-0.01}$
$S_{\rm CXB}$[§]	$6.2^{+0.1}_{-0.2}$	$6.3^{+0.1}_{-0.1}$	$6.3^{+0.1}_{-0.1}$
kT_3 (keV)	-	-	-
Norm$_3$[†]	0(fix)	0(fix)	0(fix)
χ^2 or C/dof(dof)	1.32(768)	1.35(768)	1.07(4638)

All errors indicate 90% confidence level.

[*] The column densities of galactic absorption for the MWH, CXB and HTC component were fixed to the weighted average value estimated from Kalberla et al. (2005)

[†] The emission measure of CIE plasma integrated over the line-of-sight for SWCX+LHB, MWH and HTC (the normalization of *apec* model): $(1/4\pi)\int n_{\rm e} n_{\rm H} ds$ in unit of 10^{14} cm^{-5} sr^{-1}.

[‡] The photon index of the *power-law* model for the CXB.

[§] The surface brightness of the CXB (the normalization of *power-law* model): in unit of photons s^{-1} cm^{-2} sr^{-1} at 1 keV.

[¶] The goodness of the fit is χ^2/dof.

[‖] The goodness of the fit is C/dof.

[††] Simultaneous fit with $(B_\perp L)^2$ sorted spectra.

Table D.2 Same as Table D.1 but for in SEP and NEP observation.

SEP			
Parameter	Summed(χ^2)[¶]	Summed(C)[‖]	$(B_\perp L)^2$ sort(C)[‖††]
$n_{\rm H}$[*] (10^{20} cm^{-2})	4.72(fix)	4.72(fix)	4.72(fix)
Norm$_1$[†]	$123.6^{+33.1}_{-33.1}$	$127.9^{+19.4}_{-19.1}$	$104.8^{+19.9}_{-20.9}$
kT_2 (keV)	-	-	-
Norm$_2$[†]	0(fix)	0(fix)	0(fix)
$\Gamma_{\rm CXB}$[‡]	$1.50^{+0.05}_{-0.05}$	$1.50^{+0.02}_{-0.02}$	$1.52^{+0.02}_{-0.02}$
$S_{\rm CXB}$[§]	$5.7^{+0.2}_{-0.3}$	$6.0^{+0.1}_{-0.1}$	$6.0^{+0.1}_{-0.1}$
kT_3 (keV)	$0.72^{+0.03}_{-0.03}$	$0.72^{+0.03}_{-0.02}$	$0.71^{+0.03}_{-0.03}$
Norm$_3$[†]	$1.8^{+0.2}_{-0.2}$	$1.8^{+0.1}_{-0.2}$	$1.8^{+0.1}_{-0.1}$
χ^2 or C/dof(dof)	1.06(509)	1.06(509)	1.01(2057)
NEP			
Parameter	Summed(χ^2)[¶]	Summed(C)[‖]	$(B_\perp L)^2$ sort(C)[‖††]
$n_{\rm H}$[*] (10^{20} cm^{-2})	3.92(fix)	3.92(fix)	3.92(fix)
Norm$_1$[†]	0(fix)	0(fix)	0(fix)
kT_2 (keV)	$0.24^{+0.07}_{-0.04}$	$0.24^{+0.02}_{-0.01}$	$0.23^{+0.01}_{-0.01}$
Norm$_2$[†]	$3.2^{+3.6}_{-1.8}$	$3.5^{+0.3}_{-0.3}$	$3.8^{+0.4}_{-0.4}$
$\Gamma_{\rm CXB}$[‡]	$1.34^{+0.04}_{-0.04}$	$1.33^{+0.02}_{-0.02}$	$1.33^{+0.02}_{-0.02}$
$S_{\rm CXB}$[§]	$6.1^{+0.3}_{-0.2}$	$6.2^{+0.1}_{-0.1}$	$6.1^{+0.0}_{-0.1}$
kT_3 (keV)	$0.92^{+0.30}_{-0.21}$	$0.93^{+0.09}_{-0.10}$	$0.83^{+0.11}_{-0.10}$
Norm$_3$[†]	$0.4^{+0.1}_{-0.2}$	$0.4^{+0.1}_{-0.1}$	$0.4^{+0.1}_{-0.1}$
χ^2 or C/dof(dof)	1.12(508)	1.15(508)	1.09(2056)

All errors indicate 90% confidence level.

[*] The column densities of galactic absorption for the MWH, CXB and HTC component were fixed to the weighted average value estimated from Kalberla et al. (2005)

[†] The emission measure of CIE plasma integrated over the line-of-sight for SWCX+LHB, MWH and HTC (the normalization of *apec* model): $(1/4\pi)\int n_{\rm e} n_{\rm H} ds$ in unit of 10^{14} cm^{-5} sr^{-1}.

[‡] The photon index of the *power-law* model for the CXB.

[§] The surface brightness of the CXB (the normalization of *power-law* model): in unit of photons s^{-1} cm^{-2} sr^{-1} at 1 keV.

[¶] The goodness of the fit is χ^2/dof.

[‖] The goodness of the fit is C/dof.

[††] Simultaneous fit with $(B_\perp L)^2$ sorted spectra.

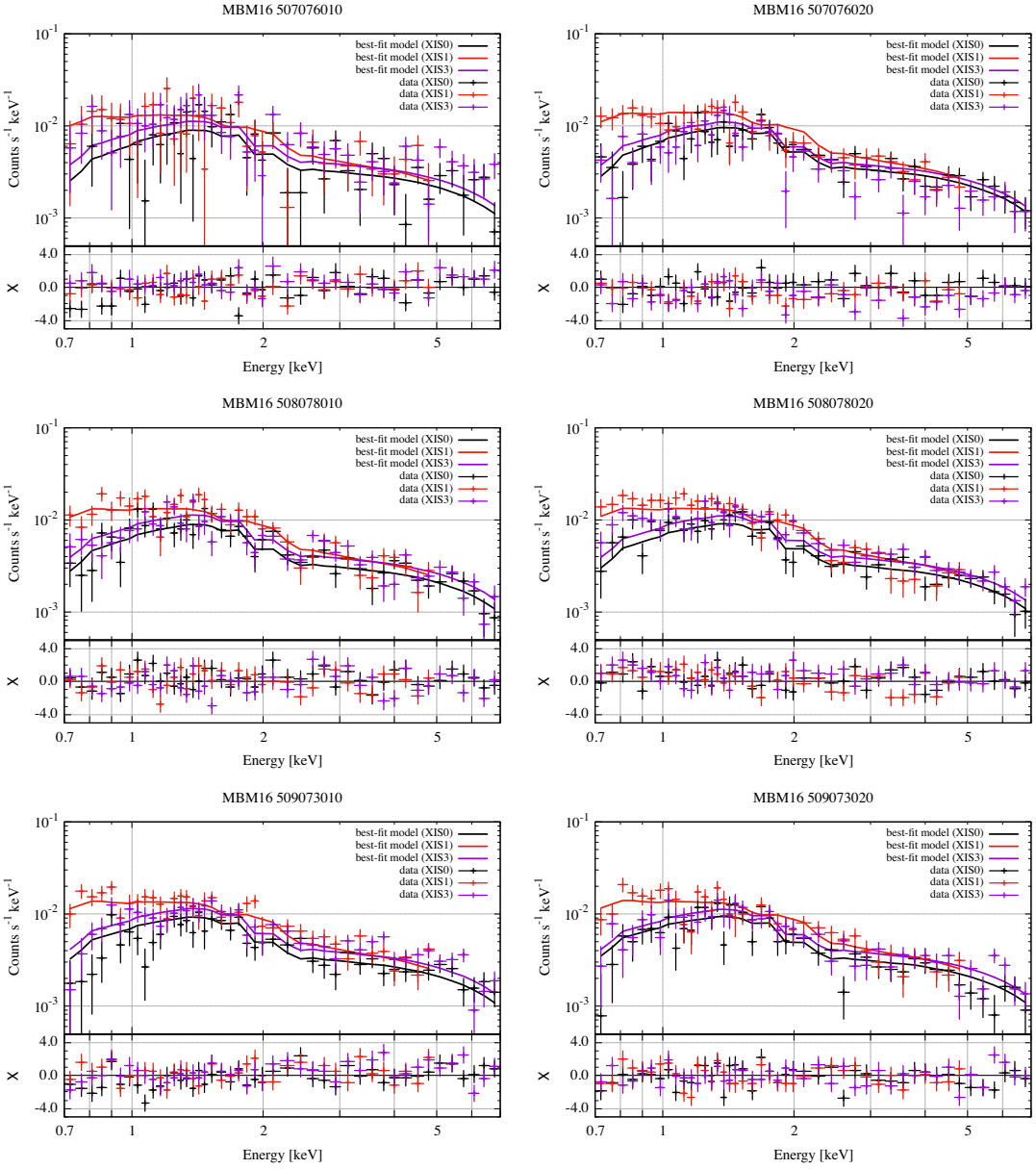

Figure D.1 Spectral fit results for MBM16 direction of each ObsID

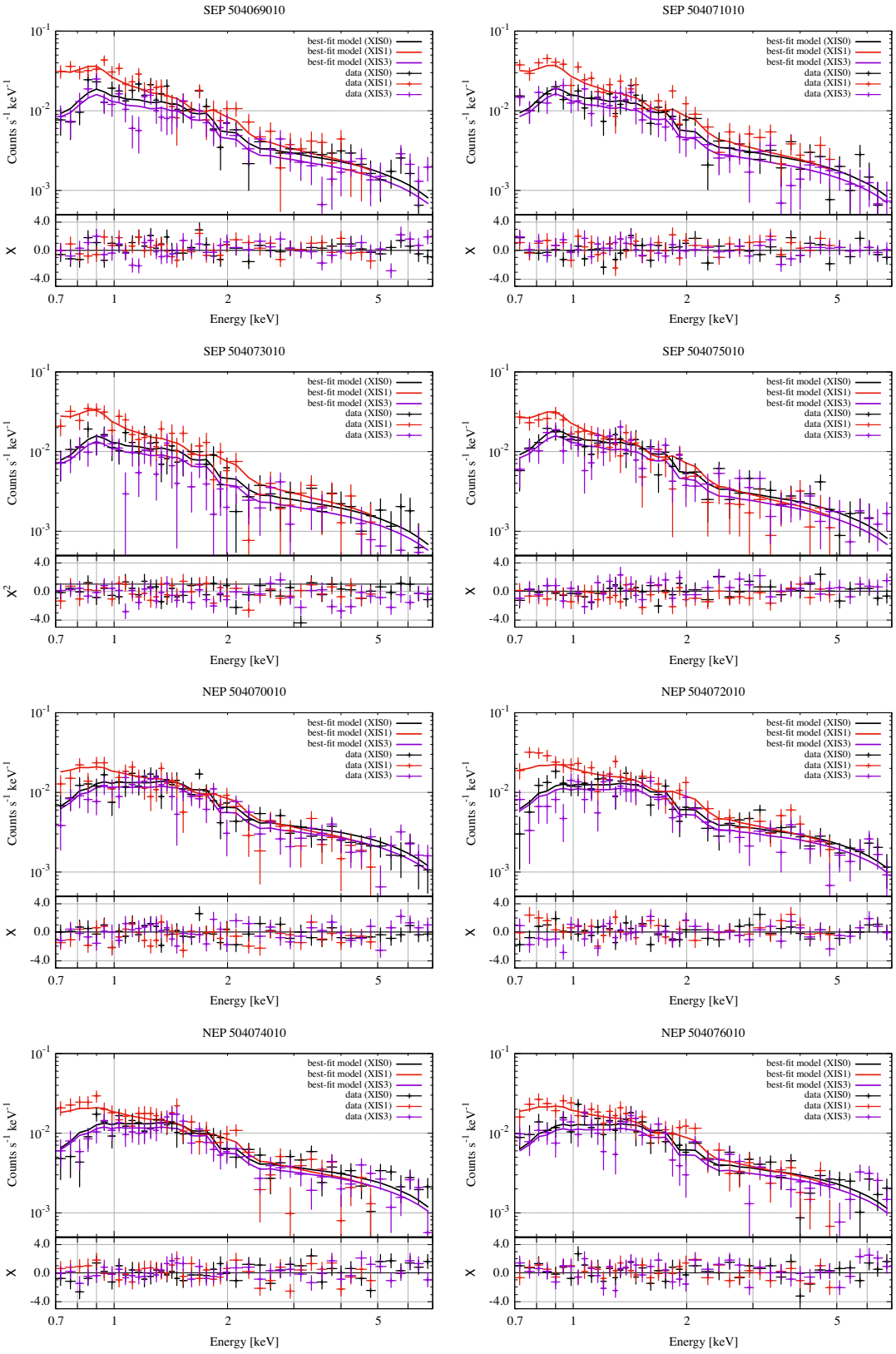

Figure D.2 Same as Figure D.1 but for SEP and NEP direction

Table D.3: Summary of NXB normalization parameters, a, by spectral fitting with XDB + ALP + NXB model.

Obs. ID	$B_\perp L$ interbal*	XIS0	XIS1	XIS3
Lockman hole				
101002010	149 - 184	$0.81^{+0.14}_{-0.13}$	$0.72^{+0.10}_{-0.10}$	$0.97^{+0.17}_{-0.17}$
	184 - 226	$0.95^{+0.16}_{-0.15}$	$0.71^{+0.10}_{-0.10}$	$1.06^{+0.19}_{-0.18}$
	226 - 314	$0.56^{+0.31}_{-0.27}$	$0.40^{0.22}_{-0.19}$	$0.92^{+0.41}_{-0.37}$
102018010	149 - 184	$1.03^{+0.19}_{-0.18}$	$0.79^{+0.14}_{-0.14}$	$0.87^{+0.19}_{-0.18}$
	184 - 226	$0.86^{+0.18}_{-0.17}$	$0.87^{+0.15}_{-0.14}$	$0.74^{+0.19}_{-0.19}$
	226 - 314	$0.81^{+0.20}_{-0.19}$	$0.73^{+0.16}_{-0.15}$	$0.99^{+0.24}_{-0.23}$
103009010	149 - 184	$0.91^{+0.15}_{-0.15}$	$0.68^{+0.11}_{-0.11}$	$0.97^{+0.17}_{-0.17}$
	184 - 226	$0.83^{+0.12}_{-0.12}$	$0.81^{+0.10}_{-0.10}$	$0.95^{+0.15}_{-0.15}$
	226 - 314	$1.04^{+0.18}_{-0.17}$	$0.92^{+0.13}_{-0.13}$	$0.93^{+0.20}_{-0.19}$
104002010	149 - 184	$1.01^{+0.16}_{-0.15}$	$0.77^{+0.11}_{-0.11}$	$1.07^{+0.16}_{-0.16}$
	184 - 226	$0.88^{+0.17}_{-0.16}$	$0.77^{+0.12}_{-0.12}$	$0.86^{+0.17}_{-0.17}$
	226 - 314	$0.93^{+0.19}_{-0.18}$	$0.89^{+0.13}_{-0.13}$	$0.95^{+0.20}_{-0.19}$
105003010	149 - 184	$0.99^{+0.23}_{-0.22}$	$0.91^{+0.16}_{-0.15}$	-
	184 - 226	$0.72^{+0.23}_{-0.21}$	$1.01^{+0.17}_{-0.17}$	-
	226 - 314	$0.76^{+0.22}_{-0.22}$	$0.67^{+0.15}_{-0.14}$	-
106001010	149 - 184	$0.79^{+0.21}_{-0.20}$	$0.87^{+0.16}_{-0.15}$	-
	184 - 226	$0.71^{+0.18}_{-0.18}$	$0.82^{+0.13}_{-0.13}$	-
	226 - 314	$0.55^{+0.29}_{-0.26}$	$0.91^{+0.21}_{-0.19}$	-
107001010	149 - 184	$1.03^{+0.28}_{-0.26}$	$0.63^{+0.18}_{-0.18}$	-
	184 - 226	$0.79^{+0.53}_{-0.44}$	$0.96^{+0.40}_{-0.35}$	-
	226 - 314	$1.37^{+1.94}_{-1.30}$	$1.27^{+1.29}_{-0.92}$	-
108001010	149 - 184	$0.84^{+0.29}_{-0.26}$	$1.02^{+0.23}_{-0.21}$	-
	184 - 226	$1.07^{+0.35}_{-0.32}$	$0.76^{+0.24}_{-0.22}$	-
	226 - 314	$2.38^{+1.70}_{-1.30}$	$3.27^{+1.39}_{-1.16}$	-
109014010	149 - 184	$0.68^{+0.31}_{-0.28}$	$0.92^{+0.21}_{-0.20}$	$1.02^{+0.28}_{-0.26}$
	184 - 226	$0.57^{+0.33}_{-0.30}$	$0.74^{+0.21}_{-0.20}$	$1.04^{+0.30}_{-0.28}$
	226 - 314	$0.78^{+0.36}_{-0.33}$	$1.09^{+0.25}_{-0.23}$	$1.32^{+0.35}_{-0.33}$
MBM16				
507076010	137 - 191	$1.16^{+0.57}_{-0.49}$	$0.87^{+0.37}_{-0.33}$	$0.79^{+0.45}_{-0.38}$
	191 - 300	$0.88^{+0.43}_{-0.39}$	$0.75^{+0.28}_{-0.26}$	$1.32^{+0.41}_{-0.38}$
507076020	137 - 191	$0.96^{+0.26}_{-0.25}$	$0.64^{+0.18}_{-0.19}$	$0.83^{+0.23}_{-0.23}$

Table continued on next page.

Continued from previous page.

Obs. ID	$B_\perp L$ interbal*	XIS0	XIS1	XIS3
	191 - 300	$0.79^{+0.28}_{-0.27}$	$0.77^{+0.19}_{-0.19}$	$0.65^{+0.25}_{-0.25}$
508078010	137 - 191	$0.96^{+0.24}_{-0.24}$	$0.83^{+0.18}_{-0.19}$	$1.04^{+0.23}_{-0.23}$
	191 - 300	$0.57^{+0.59}_{-0.50}$	$0.64^{+0.40}_{-0.35}$	$0.92^{+0.56}_{-0.49}$
508078020	137 - 191	$0.91^{+0.23}_{-0.23}$	$0.84^{+0.18}_{-0.19}$	$1.38^{+0.23}_{-0.24}$
	191 - 300	$0.95^{+0.36}_{-0.35}$	$0.94^{+0.24}_{-0.24}$	$0.76^{+0.31}_{-0.31}$
509073010	137 - 191	$0.96^{+0.27}_{-0.26}$	$0.81^{+0.20}_{-0.20}$	$1.05^{+0.25}_{-0.24}$
	191 - 300	$0.83^{+0.32}_{-0.32}$	$0.69^{+0.21}_{-0.21}$	$1.06^{+0.29}_{-0.29}$
509073020	137 - 191	$0.87^{+0.23}_{-0.23}$	$0.73^{+0.17}_{-0.18}$	$0.98^{+0.22}_{-0.22}$
	191 - 300	$0.70^{+0.29}_{-0.29}$	$0.71^{+0.19}_{-0.20}$	$0.94^{+0.27}_{-0.27}$
		SEP		
504069010	140 - 165	$0.85^{+0.19}_{-0.19}$	$0.86^{+0.13}_{-0.13}$	$0.83^{+0.17}_{-0.17}$
	165 - 255	$0.87^{+0.23}_{-0.22}$	$0.80^{+0.13}_{-0.13}$	$0.80^{+0.19}_{-0.19}$
504071010	140 - 165	$0.79^{+0.23}_{-0.22}$	$0.71^{+0.15}_{-0.14}$	$0.73^{+0.20}_{-0.20}$
	165 - 255	$0.77^{+0.24}_{-0.23}$	$0.93^{+0.15}_{-0.14}$	$0.88^{+0.21}_{-0.21}$
504073010	140 - 165	$0.83^{+0.23}_{-0.22}$	$0.77^{+0.15}_{-0.14}$	$0.52^{+0.19}_{-0.18}$
	165 - 255	$0.61^{+0.23}_{-0.22}$	$0.68^{+0.14}_{-0.14}$	$0.62^{+0.21}_{-0.21}$
504075010	140 - 165	$0.84^{+0.23}_{-0.22}$	$0.62^{+0.15}_{-0.15}$	$0.90^{+0.22}_{-0.21}$
	165 - 255	$0.68^{+0.24}_{-0.23}$	$0.65^{+0.14}_{-0.14}$	$0.94^{+0.21}_{-0.21}$
		NEP		
504070010	134 - 161	$0.62^{+0.17}_{-0.16}$	$0.71^{+0.13}_{-0.13}$	$0.99^{+0.17}_{-0.16}$
	161 - 205	$0.92^{+0.16}_{-0.15}$	$0.73^{+0.11}_{-0.11}$	$1.04^{+0.15}_{-0.15}$
	205 - 286	$0.96^{+0.19}_{-0.19}$	$0.63^{+0.11}_{-0.12}$	$0.94^{+0.16}_{-0.16}$
504072010	134 - 161	$0.82^{+0.22}_{-0.20}$	$0.83^{+0.16}_{-0.15}$	$1.18^{+0.22}_{-0.21}$
	161 - 205	$0.82^{+0.21}_{-0.20}$	$0.91^{+0.15}_{-0.14}$	$1.01^{+0.20}_{-0.19}$
	205 - 286	$1.00^{+0.25}_{-0.23}$	$0.72^{+0.15}_{-0.15}$	$0.95^{+0.22}_{-0.21}$
504074010	134 - 161	$0.84^{+0.17}_{-0.16}$	$0.70^{+0.12}_{-0.12}$	$1.07^{+0.16}_{-0.15}$
	161 - 205	$1.22^{+0.23}_{-0.22}$	$0.89^{+0.16}_{-0.15}$	$0.95^{+0.21}_{-0.20}$
	205 - 286	$1.14^{+0.40}_{-0.36}$	$0.70^{+0.25}_{-0.23}$	$1.19^{+0.37}_{-0.33}$
504076010	134 - 161	$0.89^{+0.21}_{-0.19}$	$0.75^{+0.15}_{-0.14}$	$1.15^{+0.21}_{-0.19}$
	161 - 205	$0.77^{+0.22}_{-0.20}$	$0.87^{+0.16}_{-0.15}$	$1.16^{+0.22}_{-0.21}$
	205 - 286	$1.04^{+0.26}_{-0.24}$	$0.70^{+0.16}_{-0.15}$	$0.98^{+0.23}_{-0.22}$

All errors indicate 90% confidence level.

∗ In the unit of Tm.

References

Acharya, B., & Pongkitivanichkul, C. 2016, Journal of High Energy Physics, 2016, 1

Anders, E., & Grevesse, N. 1989, Geochimica et Cosmochimica Acta, 53, 197

Andriamonje, S., et al. 2007, Journal of Cosmology and Astroparticle Physics, 2007, 010

Arik, M., et al. 2014, Physical Review Letters, 112, 091302

Asaka, T., Hashiba, J., Kawasaki, M., & Yanagida, T. 1998, Physical Review D, 58, 023507

Baker, C. A., et al. 2006, Physical Review Letters, 97, 131801

Boyarsky, A., Ruchayskiy, O., Iakubovskyi, D., & Franse, J. 2014, Physical Review Letters, 113, 251301

Brandt, W. N., & Alexander, D. M. 2015, The Astronomy and Astrophysics Review, 23, 1

Brunner, H., Cappelluti, N., Hasinger, G., Barcons, X., Fabian, A. C., Mainieri, V., & Szokoly, G. 2008, Astronomy & Astrophysics, 479, 283

Bulbul, E., Markevitch, M., Foster, A., Smith, R. K., Loewenstein, M., & Randall, S. W. 2014, The Astrophysical Journal, 789, 13

Carosi, G., Friedland, A., Giannotti, M., Pivovaroff, M. J., Ruz, J., & Vogel, J. K. 2013, Arxiv preprint astro-ph/, 8

Cash, W. 1979, The Astrophysical Journal, 228, 939

Cicoli, M., Conlon, J. P., Marsh, M. C. D., & Rummel, M. 2014, Physical Review D, 90, 023540

Conlon, J. P., & Day, F. V. 2014, Journal of Cosmology and Astroparticle Physics, 2014, 033

Conlon, J. P., & Powell, A. J. 2015, Journal of Cosmology and Astroparticle Physics, 2015, 019

Davoudiasl, H., & Huber, P. 2006, Physical Review Letters, 97, 141302

—. 2008, Journal of Cosmology and Astroparticle Physics, 2008, 026

Fraser, G., Read, A., Sembay, S., Carter, J., & Schyns, E. 2014, Monthly Notices of the Royal Astronomical Society, 445, 2146

Grupe, D., Komossa, S., Gallo, L. C., Longinotti, A. L., Fabian, A. C., Pradhan, A. K., Gruberbauer, M., & Xu, D. 2012, The Astrophysical Journal Supplement Series, 199, 28

Hayashida, K., & Inoue, H. 1989, Publications of the Astronomical Society of Japan, 41, 373

Higaki, T., Jeong, K. S., & Takahashi, F. 2014, Physics Letters B, 733, 25

Hoshino, a., et al. 2010, Publications of the Astronomical Society of Japan, 62, 371

Inoue, Y., Akimoto, Y., Ohta, R., Mizumoto, T., Yamamoto, A., & Minowa, M. 2008, Physics Letters B, 668, 93

Irastorza, I. G., et al. 2013, Journal of Physics: Conference Series, 460, 012002

Ishisaki, Y., et al. 2007, Publications of the Astronomical Society of Japan, 59, S113

Kalberla, P. M. W., Burton, W. B., Hartmann, D., Arnal, E. M., Bajaja, E., Morras, R., & Pöppel, W. G. L. 2005, Astronomy & Astrophysics, 440, 775

Kawaharada, M., et al. 2010, The Astrophysical Journal, 714, 423

Kawasaki, M., & Yanagida, T. 1997, Physics Letters B, 399, 45

Kim, J. E. 1987, Physics Reports, 150, 1

Kim, J. E., & Carosi, G. 2010, Reviews of Modern Physics, 82, 557

Kokubun, M., et al. 2007, Publications of the Astronomical Society of Japan, 59, S53

Koyama, K., et al. 2007, Publications of the Astronomical Society of Japan, 59, S23

Kushino, A., Ishisaki, Y., Morita, U., Yamasaki, N. Y., Ishida, M., Ohashi, T., & Ueda, Y. 2002, Publications of the Astronomical Society of Japan, 2, 27

Lampton, M., Margon, B., & Bowyer, S. 1976, The Astrophysical Journal, 208, 177

Masui, K., Mitsuda, K., Yamasaki, N. Y., Takei, Y., Kimura, S., Yoshino, T., & McCammon, D. 2009, Publications of the Astronomical Society of Japan, 61, S115

Mitsuda, K., et al. 2007, Publications of the Astronomical Society of Japan, 59, S1

Moretti, A., Campana, S., Lazzati, D., & Tagliaferri, G. 2003, The Astrophysical Journal, 588, 696

Murakami, H., Kitsunezuka, M., Ozaki, M., Dotani, T., & Anada, T. 2006, in Proceedings of SPIE, ed. M. J. L. Turner & G. Hasinger, Vol. 6266, 62662Y

Mushotzky, R. F., Cowie, L. L., Barger, A. J., & Arnaud, K. A. 2000, Nature, 404, 459

Pearson, K. 1900, The London, Edinburgh, and Dublin Philosophical Magazine and Journal of Science, 50, 157

Peccei, R. D., & Quinn, H. R. 1977, Physical Review Letters, 38, 1440

Raffelt, G., & Stodolsky, L. 1988, Physical Review D, 37, 1237

Roncadelli, M., & Tavecchio, F. 2015, Monthly Notices of the Royal Astronomical Society: Letters, 450, L26

Rosenberg, L. J. 2015, Proceedings of the National Academy of Sciences, 112, 12278

Saez, C., & Chartas, G. 2011, The Astrophysical Journal, 737, 91

Sakai, K., Yao, Y., Mitsuda, K., Yamasaki, N. Y., Wang, Q. D., Takei, Y., & McCammon, D. 2014, Publications of the Astronomical Society of Japan, 66, 83

Sekiya, N., Yamasaki, N. Y., & Mitsuda, K. 2016, Publications of the Astronomical Society of Japan, 68, S31

Sekiya, N., Yamasaki, N. Y., Mitsuda, K., & Takei, Y. 2014, Publications of the Astronomical Society of Japan, 66, 10

Serlemitsos, P. J., et al. 2007, Publications of the Astronomical Society of Japan, 59, S9

Sikivie, P. 1983, Physical Review Letters, 51, 1415

Smith, R. K., Brickhouse, N. S., Liedahl, D. A., & Raymond, J. C. 2001, The Astrophysical Journal, 556, L91

Smith, R. K., et al. 2007, Publications of the Astronomical Society of Japan, 59, S141

Snowden, S. L., Cox, D. P., McCammon, D., & Sanders, W. T. 1990, The Astrophysical Journal, 354, 211

Takahashi, T., et al. 2007, Publications of the Astronomical Society of Japan, 59, S35

Takahashi, T., et al. 2016, in Proceedings of SPIE, ed. J.-W. A. den Herder, T. Takahashi, & M. Bautz, 99050U

Tamura, T., Iizuka, R., Maeda, Y., Mitsuda, K., & Yamasaki, N. Y. 2015, Publications of the Astronomical Society of Japan, 67, 231

Tawa, N., et al. 2008, Publications of the Astronomical Society of Japan, 60, S11

Tawara, Y., Matsumoto, C., Tozuka, M., Fukazawa, Y., Matsushita, K., & Anabuki, N. 2008, Publications of the Astronomical Society of Japan, 60, S307

Thébault, E., et al. 2015, Earth, Planets and Space, 67, 79

Urban, O., Werner, N., Allen, S. W., Simionescu, A., Kaastra, J. S., & Strigari, L. E. 2015, Monthly Notices of the Royal Astronomical Society, 451, 2447

van Bibber, K., McIntyre, P. M., Morris, D. E., & Raffelt, G. G. 1989, Physical Review D, 39, 2089

Weinberg, S. 1978, Physical Review Letters, 40, 223

Whittaker, I. C., Gamble, R. J., Rodger, C. J., Clilverd, M. A., & Sauvaud, J.-A. 2013, Journal of Geophysical Research: Space Physics, 118, 7611

Wilczek, F. 1978, Physical Review Letters, 40, 279

Yamaguchi, H., et al. 2006, in Proceedings of SPIE, ed. M. J. L. Turner & G. Hasinger, Vol. 6266, 626642

Yao, Y., Wang, Q. D., Hagihara, T., Mitsuda, K., McCammon, D., & Yamasaki, N. Y. 2009, The Astrophysical Journal, 690, 143

Yoshino, T., et al. 2009, Publications of the Astronomical Society of Japan, 61, 805

Yoshitake, H., Sakai, K., Mitsuda, K., Yamasaki, N. Y., Takei, Y., & Yamamoto, R. 2013, Publications of the Astronomical Society of Japan, 65, 32